universität wien

MASTERARBEIT/MASTER'S THESIS

Titel der Masterarbeit / Title of the Master's Thesis

Analysis and improvement of forecasts of cyclogenesis in the northern Mediterranean Sea with WRF

verfasst von / submitted by

Fabian Lehner, B.Sc.

angestrebter akademischer Grad / in partial fulfilment of the requirements for the degree of

Master of science (M.Sc.)

Wien, 2016 / Vienna, 2016

Studienkennzahl lt. Studienblatt / degree programme code as it appears on the student record sheet:	A 066 614
Studienrichtung lt. Studienblatt / degree programme as it appears on the student record sheet:	Meteorologie
Betreut von / Supervisor:	Ao. Univ.-Prof. Dr. Leopold Haimberger

Abstract

An accurate forecast of Mediterranean cyclones is exceptionally important for a satisfying weather forecast in Central Europe. In particular, Vb lows are often responsible for heavy precipitation. Therefore, a better forecast is of public interest.

In this thesis, 14 cases of cyclogenesis in the Northern Mediterranean Sea between the years 2013 and 2015 are investigated, some of them feature a Vb low. Four different configurations with the numerical model WRF were run, where the topography (ECMWF, 4 km and 1.33 km topography), the horizontal resolution (4 km and 1.33 km) and the initialization on the vertical levels of the global model of ECMWF (on either 25 pressure or 137 hybrid levels) were changed. The results are discussed regarding bias, RMSE and the SAL-method, an object-based verification method for precipitation. The verification sources include radio soundings, in-situ weather stations on the ground and weather radar.

A closer look on two cases is taken. One case between 2015-02-04 and 2015-02-07 shows that the pressure and precipitation fields are shifted to the north. However, a more realistic topography and higher model resolution can reduce this error. This makes a huge difference at the northern edges of the precipitation fields, e.g. in Vienna. The accumulated precipitation differs up to a factor of 5 or 6. Another case between 2014-08-31 and 2014-09-03 shows a similar northward shift of pressure isolines and partly also of precipitation fields.

Overall, it can be stated, that there is not much difference between the initialization on ECMWF hybrid or pressure levels. Major improvement can be achieved when running the model with a 4 km topography instead of using the much smoother ECMWF topography. If one uses the nested domain over the Alps with a resolution of 1.33 km, some errors can be reduced even more. However, this last model configuration comes with three times the computational costs.

It is rather unsatisfying that even the best WRF run with the nested topography in the Alps is - at best - as accurate as the ECMWF forecast. Some repeatedly occuring errors, such as a negative MSLP bias in general and a warm temperature bias in the higher resolutions, need further investigation.

Zusammenfassung

Eine genaue Vorhersage von Zyklonen im Mittelmeer ist von außerordentlich wichtiger Bedeutung für eine zufriedenstellende Wetterprognose in Mitteleuropa. Insbesondere sind Vb Tiefs oft mitverantwortlich für heftige Niederschläge. Daher ist eine bessere Vorhersage nicht nur von wissenschaftlichem, sondern auch von öffentlichem Interesse.

In dieser Arbeit werden 14 Fälle von Zyklogenesen im nördlichen Mittelmeerraum zwischen 2013 und 2015 untersucht, einige davon sind Vb Tiefs. Vier verschiedene Konfigurationen des frei verfügbaren numerischen Prognosemodells WRF wurden gerechnet, wobei die Topografie (EZMWF, 4 km und 1.33 km Topografie), die horizontale Auflösung (4 km und 1.33 km) und die Initialisierung auf den vertikalen Levels des Globalmodells von EZMWF (entweder auf 25 Drucklevels oder auf 137 Hybridlevels) geändert wurden. Die Ergebnisse werden in Bezug auf den Bias, den RMSE und auf die SAL-Methode, eine objekt-basierte Verifikationsmethode für Niederschlag, untersucht. Die Quellen für die Verifikation stammen aus Radiosonden, Wetterstationen am Boden oder von Regenradaren.

Zwei der 14 Fälle werden genauer untersucht. Der Erste der beiden Fälle zwischen dem 04.02.2015 und dem 07.02.2015 weist eine Verschiebung der Druck- und Niederschlagsmuster nach Norden auf. Dieser Fehler wird aber durch eine realistischere Topografie oder durch eine höhere Auflösung reduziert. Besonders markant ist dieser Fehler am Nordrand der Niederschlagsfelder, wie z.B. in diesem Fall in Wien. Zwischen den Niederschlagsmengen der verschiedenen WRF Konfigurationen liegt ein Faktor von 5 oder 6. Im zweiten Fall zwischen dem 31.08.2014 und dem 03.09.2014 sind die Druckmuster ebenfalls nach Norden verschoben, zum Teil gilt das auch wieder für den Niederschlag.

Insgesamt kann man feststellen, dass der Unterschied zwischen der Initialisierung auf den EZMWF Drucklevels und den Hybridlevels sehr gering ausfällt. Wesentlich größer hingegen ist der Unterschied von der Modellkonfiguration mit der 4 km Topografie zur glatteren EZWMF Topografie. Mit der genesteten Domain in den Alpen können viele Fehlermaße noch etwas weiter verringert werden, auch wenn das mit der dreifachen Rechenkapazität teuer erkauft wird.

Es ist leider ziemlich unbefriedigend, dass sogar die WRF Konfiguration, die am besten abschneidet, noch immer nicht besser ist als das EZMWF Modell. Bezüglich einiger wiederholt auftretender Fehler, wie einem negativen MSLP-Bias oder einem warmen Temperatur-Bias in der höchsten Auflösung, besteht noch Bedarf an genauerer Untersuchung in zukünftigen Arbeiten.

Contents

1 Motivation and Aim of this Thesis

Exceptional and large scale precipitation events over Central Europe are often related to low pressure systems propagating over the Mediterranean Sea. For flooding events such as in August 2002 in Austria and Eastern Germany, a major contribution to the local precipitation originated from moisture sources over the Adriatic or the Mediterranean Sea. Therefore, these specific cyclone paths over the northern Mediterranean Sea are an important contributing factor to large scale heavy precipitation over Central Europe and are subject of research mainly for European scientists. Already in the 19$^{\text{th}}$ century, Van Bebber (1882) analyzed and classified cyclone tracks over Europe into five main categories denominated by Roman numerals from I to V. Type V is still in use today - especially Vb-tracks over the northern Mediterranean, the Eastern Alps and the Baltic region or Vc-tracks with a path over Eastern and Southeastern Europe (Hofstätter and Chimani, 2012).

The typical spatial and temporal scales of Mediterranean cyclones is much lower than those of Atlantic lows, which is one reason why many NWP models have considerably larger forecast errors with Mediterranean cyclones. The meteorological experience shows that even slight displacements of Mediterranean lows can cause completely different weather at certain places. Mediterranean lows are commonly known as difficult to forecast with global models. Surprisingly, the local area model WRF (Weather Research and Forecasting Model) sometimes even shows greater deviations from observations compared to global models. The question and hypothesis of this work is therefore:

Which parameters in WRF have to be changed to gain a better and more accurate short-range forecast of cyclogenesis in the northern Mediterranean Sea?

2 Climatology of Cyclones in the Mediterranean Region

As the Mediterranean Region mostly lies between 35°N and 45°N which is a transition area between the subtropical high pressure belt and the midlatitude westerlies. It represents an important source of energy and moisture. Many cyclones are therefore reinforced when traveling over the Mediterranean Sea or originate in this area itself.

One of the first objective climatologies of Mediterranean cyclones was done by Alpert et al. (1990). The spatial resolution was very low compared to current studies (2.5° x 2.5°) and the ECMWF analysis only had a period of 5 years from 1983 to 1987. Maheras et al. (2001) used the same spatial resolution but a much longer period of 40 years from 1958 to 1997. Much higher resolution data was used in Campins et al. (2006) with a 0.5° x 0.5° grid over an 8 year period from 1995 to 2003. Trigo et al. (1999) developed a cyclone tracking algorithm and analyzed ECMWF data from 1979 to 1996 on a 1.125° x 1.125° grid. The tracking algorithm identified local minima in the 1000 hPa geopotential height. Two conditions had to be met: The central sea level pressure is required to be below a value of 1020 hPa and the mean pressure gradient in an area of 9° lat and 11.25° long around the minimum pressure has to be at least 0.55 hPa per 100 km. In general, over 60 % of the detected lows lasted for less than 12 hours (Fig. 2.1 left). If only those cyclones with a lifetime of at least 12 hours are considered, the average lifetime is 28 hours, which is far less than the lifetime of a typical North Atlantic low. Also the average maximum sizes are much smaller than those of synoptic lows with approximately 500 km (Fig. 2.1 right), which usually belongs to the mesoscale size. The size is defined as the distance between the center and the nearest saddle point in the 1000 hPa geopotential field.

Campins et al. (2011) used ERA-40 data with the same resolution of 1.125° x 1.125° but for a longer range from 1957 to 2002. They detected cyclones by finding a local minimum in the smoothed mean sea level pressure (MSLP) field. As a condition, a minimum gradient of 0.5 hPa per 100 km around the center must be present. The radius of cyclones is the distance from the center to the zero vorticity line. The averaged distance in 16 directions defines the mean radius. They stated that the mean radius of cyclones is 518 km, which is comparable to those obtained in Trigo et al. (1999).

To find the cyclone tracks and therefore, the lifetimes of cyclones, a tracking algorithm was implemented (Campins et al., 2011): Cyclone centers tend to move along the 700 hPa wind. An elliptic area around this area is defined. If the cyclone center is found in that area, then it is flagged as the same cyclone. Otherwise the cyclone has vanished. The average lifetime is found to be very short with 49.5 % of the cyclones having a lifetime

below 6 h. If those are not included, the average lifetime is 22.2 h, which is also similar to the lifetime found by Trigo et al. (1999).

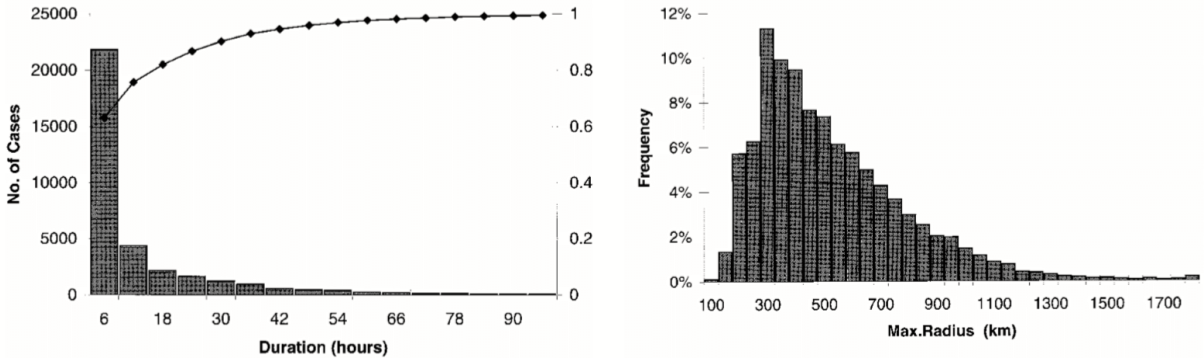

Figure 2.1: Left: Histogram of detected cyclones' lifetime. Right: Maximum radius distribution only for cyclones with a minimum life cycle of 12 h (Trigo et al., 1999)

.

2.1 Areas of Cyclogenesis

Alpert et al. (1990) found out that the Gulf of Genoa and the region around Cyprus were frequently observed as cyclogenetic. This was later confirmed by other studies as e.g. Maheras et al. (2001). They found one more high frequency center of cyclogenesis in southern Italy. Trigo et al. (2002) stated that one of the major cyclogenesis areas is the Gulf of Genoa which is persistent throughout the year. In winter, it even is the most active region of the whole Mediterranean Sea (Trigo et al., 2002), causing the most intense cyclones (Maheras et al., 2001). Genoa lows are mainly of lee cyclogenesis origin. Numerical experiments show no or just very weak cyclogenesis activity over this area when the Alps are absent. The life cycle is about 31 hours, which is above Mediterranean average throughout the whole year. Other cyclogenetic areas are located near the Atlas Mountains in the Sahara as well as in the Iberian peninsula. In the eastern part of the Mediterranean Sea, the Aegean Sea is one major source of cyclones (Trigo et al., 1999). Other areas will not be discussed here due to a lack of influence to the area of interest of this work, which is mainly the Greater Alpine Region. However, Fig. 2.2 shows all cyclogenesis areas in the Mediterranean depending on the month.

Campins et al. (2011) found the Gulf of Genoa but also the region around Cyprus to be one of the most outstanding maxima of the cyclogenetic regions. Other areas are less preferred. The high spatial resolution of Campins et al. (2006) allowed to find smaller cyclogenetic hot spots. Overall, they do not much differ from the ones found in other studies but additional maxima were found e.g. in the Gulf of Venice.

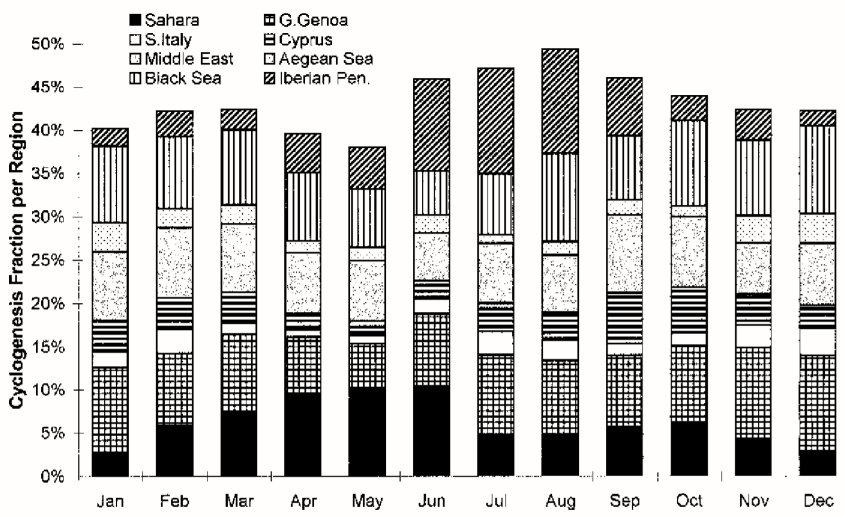

Figure 2.2: Monthly fraction of cyclogenesis events within the main cyclogenesis areas (Trigo et al., 1999)

2.2 Seasonality of Cyclogenesis

Trigo et al. (2002) stated that cyclogenesis tends to cluster around certain regions in spring and summer (Fig. 2.2). However, these areas are more scattered in summer due to higher influence of thermal profiles and diurnal forcings. In winter, a strong link to synoptic troughs and orography can be distinguished. Campins et al. (2011) stated that Cyprus stands out in the summer as a maximum of cyclogenesis. Trigo et al. (1999) detected 3 distinct seasons with respect to cyclogenesis characteristics: winter (lasting from October to March), spring (March to June) and summer (June to October). Therefore, the traditional meteorological Autumn can either be seen as late summer or early winter. The peak of the winter season occurs in January when the polar front jet is most likely to influence the Northern Mediterranean Sea. In combination with the strong land-sea contrast, the baroclinicity is high and supports cyclogenesis. Even though the number of cyclones may be higher in other seasons, the most wet and severe weather conditions are often linked to winter cyclones (Trigo et al., 2002).

One important distinction criterion of winter compared to other seasons is the little influence of local instabilities and convection, which is more prominent in other seasons (e.g. in summer). This leads to an increased dependency on the time of day towards the summer months and reaches a peak in August, when most of the cyclolyses occur early in the morning while cyclogenesis takes place in the afternoon hours (Trigo et al., 2002). However, Maheras et al. (2001) described a substantial diurnal variability for the Cyprus cyclogenesis center, in particular during winters. The time of day influences the dynamics and thus causes the cyclogenesis to occur in different locations. Whereas during the night, sea effects dominate, the Turkish Mountains play a more important role during daytime. In the western Mediterranean, they hardly found any diurnal variability during the winter in agreement with Trigo et al. (2002).

Another difference between the seasons is the lifetime of cyclones. Longer lasting cy-

clones, especially ones with a lifetime of more than one day, are significantly more frequent in winter (Campins et al., 2011). Campins et al. (2006) found a general distinction criterion for the seasons: In summer, cyclones are mostly found over land which is due to thermal effects which cause lower pressure over land. On the other hand, cyclones preferably develop over the sea during winter and autumn when the Mediterranean Sea forms a warm pool against the cold land.

2.3 Gulf of Genoa

The proximity of the Alps allows to identify Genoa cyclogenesis as lee cyclogenesis when taking the prevailing direction of air streams into account. Tsidulko and Alpert (2001) stated that during their time of research, there was a lack of understanding the key phenomena of lee cyclogenesis although there were a few mature theories. Some key dynamic processes are still unclear or badly understood. However, it is found that the upper-level dynamics play a significant role in the process of lee cyclogenesis. There is a strong connection between the upper-level potential vorticity and lee cyclogenesis. McGinley and Zupanski (1990) go even further and found out that the most powerful lee cyclones rather depend on the strength of the upper-level jet than on the strength of the lower-level cold front. However, weak cyclones tend to be more dependent on lower-level dynamics.

The lee cyclogenesis is related to the retardation of fronts by the Alps. The pressure in the lee falls mainly due to the approach of the upper-level trough but the cold air is retarded. Therefore, the pressure fall continues instead of a pressure rise due to the front passage and a new cyclone develops (Egger and Hoinka, 1992).

The following statements are based on analyses of the month January, where Genoa cyclones are most frequent and intense in the Mediterranean Sea. At the beginning of a Genoa cyclone's life cycle, there is a large negative height anomaly of the 1000 hPa surface over central Europe (Fig. 2.3 top left). This depression has the scale of a synoptic midlatitude perturbation in the order of 1000 km.

In northern Italy, a distinct secondary depression center can be found, were the air is forced to flow over or around the Alps. This is the usual and most described picture of Genoa cyclogenesis, which is orographically induced but as well linked to the existence of a synoptic scale upper-level east moving trough (Fig. 2.3 bottom). At the mature stage (Fig. 2.3 top right) the low is now elongated over the Italian peninsula. This is the result of two preferred cyclone tracks one of which is in the northern part of Italy. The second route is southeastward along the Adriatic coast.

If one considers the 850 hPa temperature, Genoa lows are linked to a high level of baroclinicity where a strong gradient is located in the Alpine region. The cyclogenesis is further maintained by cold air advection on the western flank of the larger synoptic system towards the relatively warm Mediterranean Sea (Fig. 2.4). However, this is not a crucial factor since Genoa cyclones are mainly orographically induced.

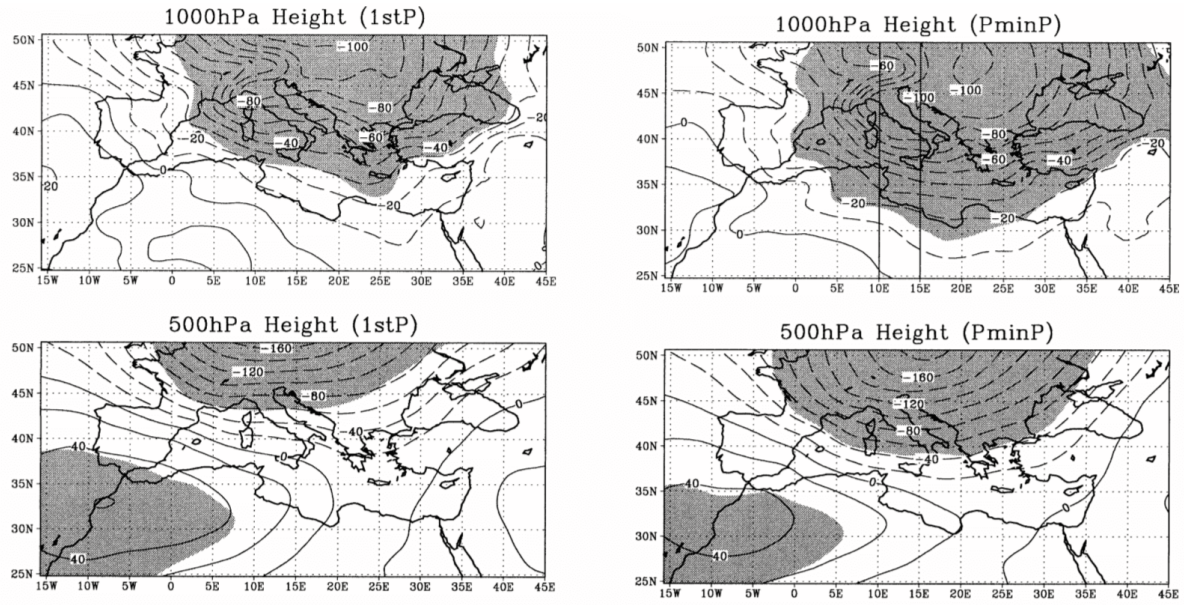

Figure 2.3: Anomalies of geopotential height in gpm at 1000 hPa and 500 hPa for Gulf of Genoa cyclones in January. Anomalies within the shaded regions are statistically significant at the 99 % confidence level. Left: At first detection of cyclone. Right: At the stage where the central pressure is lowest (Trigo et al., 2002)

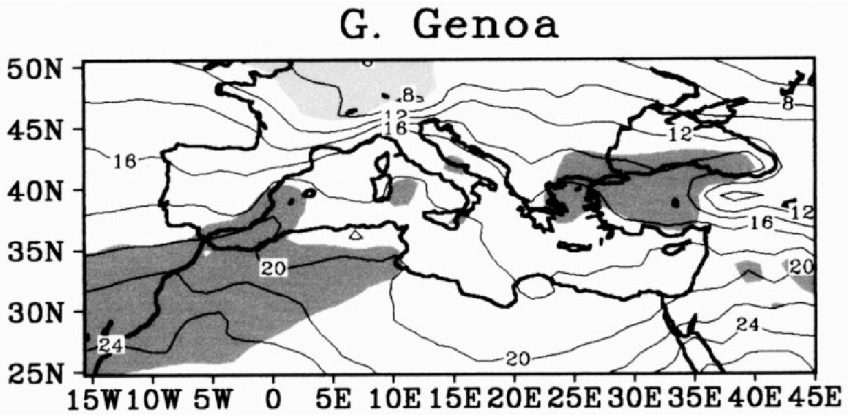

Figure 2.4: Potential temperature (contours every 2°C) at 850 hPa, obtained for the first detection of Genoa cyclones in January. light (dark) shaded regions are significantly colder (warmer) than the climatology, at the 99 % confidence level (Trigo et al., 2002).

2.4 Vb Cyclone Track

If a cyclone moves from the northern Mediterranean Sea (e.g. the Gulf of Genoa) northeastward over Hungary and Poland, this is called Vb cyclone. This was first defined by van Bebber (1891). He found cyclone track categories and labeled them with Roman numerals from one to five. Most of these categories are not in use any more nowadays. Vb tracks are associated with extremely strong winds and heavy precipitation in the northern Alpine region whereas heavy precipitation in the southern Alps is linked to deep upper-level troughs over the western Mediterranean or by Genoa cyclogenesis (Messmer et al., 2015). Many studies have investigated the factors that contribute to Vb-linked heavy precipitation. Evaporation from land surfaces, long-range advection of moisture , a quasi-stationary tropospheric trough or orographic lifting are suggested as contributing factors.

Recently, some studies that go beyond single case studies have been published. Hofstätter and Chimani (2012) analyzed ERA-40 from 1961 to 2002 and ERA-Interim data to be able to make quantitative statements about Vb cyclones. The results show that Vb is a rare event that happens on average 3.5 times per year with the highest probability of occurrence in April and a secondary maximum in Autumn. Mudelsee et al. (2004) studied floods in Central Europe in the past 500 years and found a significant, but weak relation between flood occurrence and meridional Vb-like weather situations.

Messmer et al. (2015) provided a study about the physical mechanisms that impact precipitation amounts of Vb cyclones. They applied a cyclone detection and tracking tool to the ERA-Interim reanalysis (1979-2013). A similar rareness of Vb cyclones was found with 2.3 appearances per year, and the probability maximum was found in spring as well. Extremely heavy precipitation events hardly occur in winter, which they explain with the present moisture due to the Clausius-Clapeyron equation. However, the moisture source varies from case to case and can be the Mediterranean or the Atlantic Sea or others. Not only in winter but also in summer, there is a large variability in precipitation intensity. Of all Vb events, only 23 % are associated with extreme precipitation. An important dynamic distinction criterion for heavy precipitation events is that they feature a distinct cut-off low pressure system extending over the whole atmosphere which allows a wind vortex to form. The low pressure system is not elongated over the whole atmosphere in weak events where the inflow takes place at the southern or southeastern side of the Alps. In contrast, the vortex causes inflow from the north or northeast in heavy events and in combination with orography, the conditions for heavy precipitation are met.

3 The Weather Research & Forecasting Model (WRF)

The Weather Research and Forecasting (WRF) model is a numerical weather prediction and atmospheric simulation system designed for both research and operational applications (Skamarock et al., 2008). The current release is Version 3. It is suitable for a broad span of applications ranging from global simulations to large-eddy simulations. Therefore, the scale ranges from several meters to thousands of kilometers (Wang et al., 2015).

The WRF model is fully compressible and nonhydrostatic with a hydrostatic option. It is developed by a cooperation of many institutes worldwide, mainly the National Center for Atmospheric Research (NCAR) and the National Centers for Environmental Prediction (NCEP), but also the Earth System Research Laboratory (ESRL), the Department of Defense's Air Force Weather Agency (AFWA), the Naval Research Laboratory (NRL), the Center for Analysis and Prediction of Storms (CAPS) at the University of Oklahoma and the Federal Aviation Administration (FAA) with the participation of university scientists (Skamarock et al., 2008).

WRF is available with 2 different cores:

ARW: Advanced Research WRF (NCAR)

NMM: Nonhydrostatic Mesoscale Model (NCEP)

The main difference between these two model cores is that ARW has more complex dynamics and physics settings than NMM (Rausch, 2012). Its vertical coordinate is a terrain-following hydrostatic pressure coordinate. Vertical coordinates are explained in detail in section 4. The grid staggering is the Arakawa C-grid (see Fig. 3.2). This means that the normal velocities are staggered one-half grid length from the thermodynamic variables. The column mass μ, the moisture variables q_m as well as the diagnostic variables, the pressure p and the inverse density α are also computed at the same point as the thermodynamic variables. The geopotential Φ and the vertical velocity w is vertically staggered (Skamarock et al., 2008). The model uses Runge-Kutta 2^{nd} and 3^{rd} order time integration schemes (default and used in this work), and 2^{nd} to 6^{th} order advection schemes in both the horizontal and vertical direction. (Wang et al., 2015).

3.1 Nesting

WRF-ARW comes with a nesting option, that allows you to introduce a higher resolution grid over a certain region. Newer implementations not only provide horizontal but also

vertical nesting. The nested grids allow any integer spatial and temporal refinements of the parent grid (i.e. the ratio of the coarse grid resolution of the parent grid and the fine grid resolution of the nested domain are integers). The ARW framework also comes with the option of a moving nested domain.

Nesting can be implemented as either 1-way nesting or 2-way nesting, which refers to the interaction between the nested domain and the parent domain. Both use the outer coarse grid as boundary conditions. The difference is as follows:

1-way nesting only allows information exchange from the parent grid to the nested domain by providing the boundary conditions.

2-way nesting: It allows flow of information from the nested domain to the parent domain. The fine gridpoints replace the coarse grid for gridpoints inside the nested domain. The coarse grid integrates one time step, then the fine grid integrates up to the same time and gives feedback to the coarse grid.

WRF-ARW offers the possibility of more than one finer grid (child grid). The coarse grid (parent grid) may have one or more child grids, each of which in turn may successively contain one or more child grids (Fig. 3.1(a)) or several child grids could share the same parent grid (Fig. 3.1(b)). Both of these options could be a static domain or a moving

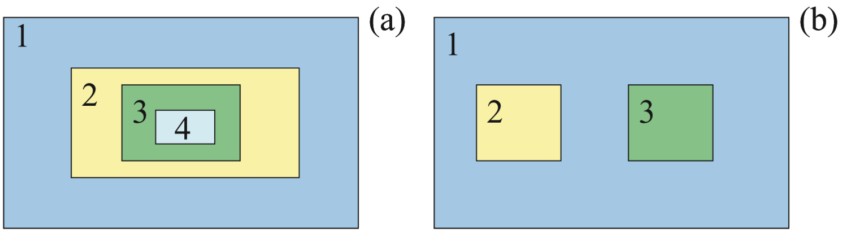

Figure 3.1: Allowed nest configurations for multiple grids. (a) Telescoping nests. (b) Nests at the same level with respect to a parent grid (Skamarock et al., 2008).

nest. The moving nest not only supports prescribed shifts (user specific) but also a vortex following shift. This is an automatic algorithm which maintains a well defined vortex in the center of the fine grid (Skamarock et al., 2008).

3.1.1 Staggering and Feedback

WRF-ARW uses an Arakawa-C grid staggering, where the wind components u and v are defined at the edges of the grid cell. The mass/thermodynamic/scalar/chemistry variables are defined at the center of each cell, as shown in Fig. 3.2. The wind components are representative for the cell-face, whereas all other quantities in the center of the cell represent the mean value throughout the cell. Since this is valid for the fine grid as well as the coarse grid, the feedback from the fine grid to the coarse grid is handled to preserve these mean values. All mass/thermodynamic/scalar/chemistry variables within a coarse

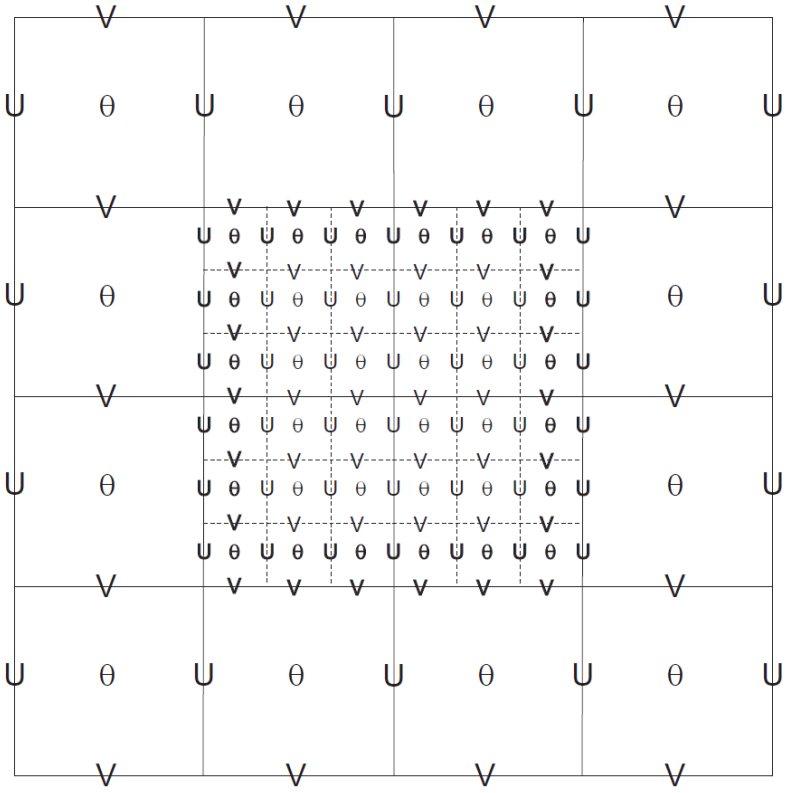

Figure 3.2: Arakawa-C grid staggering with a nested domain (odd 3:1 ratio). The solid lines denote the coarse grid, the dashed lines represent the fine grid. The horizontal wind components U and V are defined at the cell-faces, the thermodynamic variable (Θ) as well as the mass/scalar/chemistry variables in the cell center (Skamarock et al., 2008).

grid cell are averaged during the feedback from the fine to the coarse grid. The wind variables are averaged along the correspondent cell-face in the coarse grid.

The grid-distance ratio of the nested and the parent domain has to be an integer. However, there is a difference between odd and even ratios concerning the feedback from the fine to the coarse grid (Skamarock et al., 2008):

odd ratio: An often used odd ratio for nesting is 3:1. For all odd ratios, there are coincident points for the coarse and fine gridpoints. The center fine grid cell is coincident with the coarse grid cell. With a 3:1 ratio, the feedback averages 9 neighboring grid cells for the coincident coarse grid cell. For the horizontal momentum fields (i.e. the horizontal wind components), the mean of three fine gridpoints along the grid-faces is fed back to the coarse grid (Fig. 3.2).
There are masked fields where it does not make sense to compute mean values, such as soil temperature or sea ice. When averaging adjacent gridpoints to compute sea ice values, one neighboring gridpoint could be a land point. Therefore, for masked fields only, a so-called single point feedback is used, where only one fine grid cell is fed back to the coarse grid which is - in the case of odd ratios - the center grid cell.

even ratio: For even grid-distance ratios, there are no coincident points for single point

feedback mechanisms. There are always four fine grid cells equally close to a coarse grid cell. In this case, only one of those points is used for feedback which was arbitrarily chosen to be the south-west point. This arbitrariness gives odd ratios an advantage compared to even ratios when masked fields are included.

3.2 WRF Work-flow

WRF offers ideal case simulations to run experiments in conditions with given soundings and a simplified analytic topography. Ideal case simulations are not considered any further in this work since they are not in use for weather prediction.
Real case simulations are split into five separate, executable files written in Fortran 90 code (Rausch, 2012). The first three programs (geogrid, ungrib and metgrid) do different preparation steps before the next program (real) interpolates the data vertically. The first three programs together build the WRF Preprocessing System (WPS). A schematic of the working steps is illustrated in Fig 3.3.

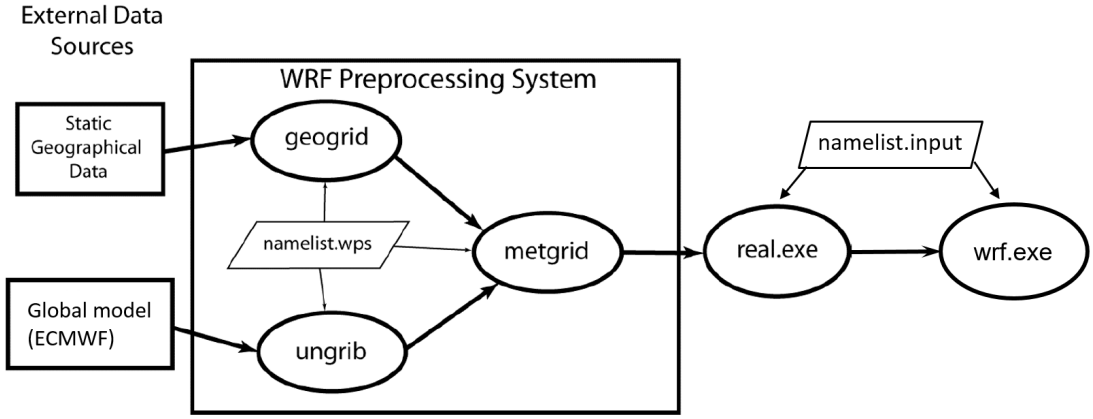

Figure 3.3: WRF work-flow for real case simulations. Elliptic symbols represent executable programs. The two parallelograms (namelist.wps and namelist.input) represent textfiles for editing and determining model settings. Adapted from Andersson (2015).

3.2.1 WRF Preprocessing System (WPS)

Each of the WPS programs reads parameters from a textfile named "namelist.wps". This namelist file features shared data that is used by all WPS programs as well as different parts for each individual program. Following programs are executed in chronological order (Andersson, 2015):

Program geogrid

Geogrid defines the model domain or domains and interpolates static and terrestrial data sets to the model grid. These are parameters that stay constant throughout the model

run. Examples are the map scale factor, soil categories, land use categories, the definition of gridpoints and distances (as defined in the file namelist.wps), the monthly albedo or the topography (i.e. the terrain height). These data sets are available on the WRF download page for free up to a resolution of 30". Since geogrid data is not time dependent, there is no need to run this program every time a new run is initialized as long as the domain stays unchanged.

Program ungrib

The purpose of ungrib is to read GRIB files, as usually provided by global models such as ECMWF or GFS, and convert the data into an intermediate format that is readable for WRF. Three formats are available, namely WPS, SI and MM5 format, although WPS is most commonly used and recommended. The GRIB files contain time varying meteorological parameters. GRIB files often contain more fields than actually needed by WRF. These fields are identified by codes (e.g. a triple digit number), which are provided by a textfile called Vtable, the variable table.

Program metgrid

The output of ungrib is needed by metgrid which horizontally interpolates the meteorological fields from the intermediate file (which is still on the grid of the global input model) to the model gridpoints. The interpolation method can even be specified separately for each parameter. For successful execution of metgrid, the following parameters must be available: 3-dimensional fields of temperature, relative humidity, horizontal wind components and 2-dimensional fields of surface pressure, sea-level pressure, of the layers of soil temperature, of soil moisture, snow depth, skin temperature, sea surface temperature and a sea ice flag (Rausch, 2012).
The domain is defined by geogrid. The space of time is written in the shared part of the file namelist.wps. The output of metgrid can be written in NetCDF files for easy visualization with external software.

3.2.2 WRF Initialization and Model Run

WRF can be initialized with two large classes of simulation: Those with an ideal initialization and those utilizing real data. Real data cases need pre-processed files from WRF Preprocessing. The function of the program real is to initialize meteorological variables, such as the horizontal wind components, potential temperature or the vapor mixing ratio. It also defines a vertical coordinate that is used to vertically interpolate input data according to the hydrostatic pressure coordinate of WRF, as defined in Eq. 4.4. Furthermore, it initializes static fields for the map projection and the physical surface (topography).

All these tasks are also performed in ideal case simulations with the program *ideal.exe* but *real.exe* for real cases does some additional processing:

- Real splits the geopotential and the column pressure into a reference state without

moisture and a perturbation part (with moisture) to prevent truncation errors in the numerics.

- It reads meteorological and static input data from the WRF Preprocessing System.
- It vertically interpolates soil fields to the required levels according to the used land surface scheme
- It creates a lateral boundary condition NetCDF file for WRF initialization and finally an input file with the initial conditions.
- ... and it does many further needed processing steps, as specified in Andersson (2015).

The program real.exe may be run parallelized which is often very useful due to the bigger workload compared to WPS. The actual numerical integration program is *wrf.exe* which is also possible to be run in a distributed memory configuration.

4 Vertical Coordinates

Pressure and height surfaces are not best suited for numerical weather prediction because they lead to difficult boundary conditions. Therefore, other surfaces have been developed, such as theta or sigma (σ) surfaces (Zhang et al., 2002). Theta surfaces are parallel to levels of constant potential temperature (Fig. 4.1 bottom left), σ levels (Fig. 4.1 bottom right) are explained in section 4.1. A comparison of different vertical coordinates is shown in Fig. 4.1, where a mountain is located in the middle of the region.

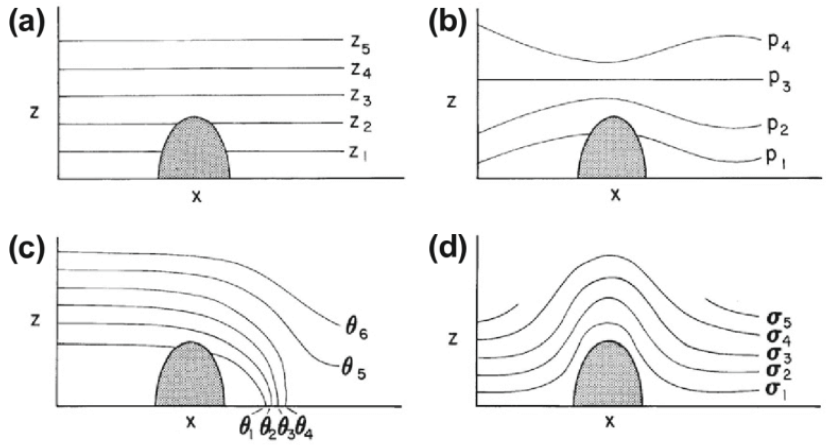

Figure 4.1: Schematic illustrations of (a) height, (b) pressure, (c) isentropic and (d) sigma coordinates (Pielke Sr, 2013)

Generally, a model surface not crossing the model topography allows more efficient use of computer resources as well as an easier implementation of the lower boundary conditions (Pielke Sr, 2013). This is why height, pressure or isentropic coordinates are hardly used in numerical weather prediction systems.

Many global models use a generalized vertical coordinate, based on a given pressure p as the physical altitude variable (which is not the same as pressure coordinates) and has the functional form

$$\eta = h(p, p_s) \tag{4.1}$$

where p_s is the surface pressure and $h(p, p_s)$ is a monotonic function of pressure. It is standard convention to define η to be dimensionless and normalized from 1 at the bottom to 0 at the top of the model. The dependence on p_s allows the definition of terrain-following σ coordinates (Eckermann, 2009), as shown in section 4.1. For a comparison of currently popular vertical coordinates used in numerical weather prediction, see Fig. 4.2.

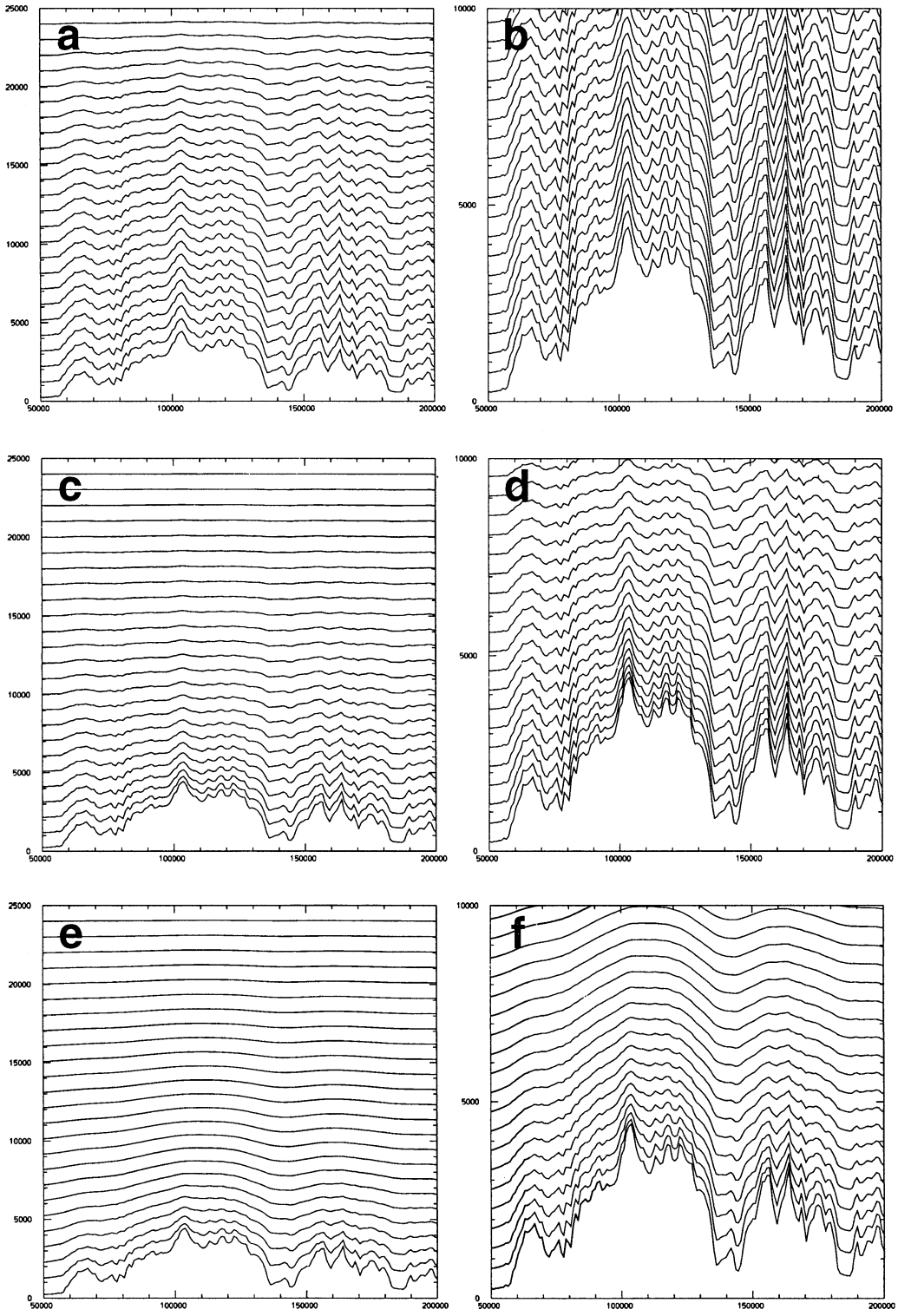

Figure 4.2: Comparison of popular vertical coordinates used in models. A vertical cross section showing three different vertical coordinates. Left-hand panels show the full model depth, while right-hand panels show the lowermost 10 km. (a) and (b) are terrain-following σ coordinates, (c) and (d) hybrid $\sigma - p$ coordinates, (e) and (f) SLEVE coordinates (Schär et al., 2002).

4.1 Terrain-following σ Coordinates

Terrain-following σ coordinates are defined as (Eckermann, 2009):

$$\eta = h(p, p_s) = \frac{p - p_{top}}{p_s - p_{top}} = \sigma \tag{4.2}$$

σ coordinates are often used in models. If p_{top} vanishes, one obtains the original Phillips σ coordinate of 1957

$$\sigma = \frac{p}{p_G} \tag{4.3}$$

where p is the pressure at any level and p_G is the surface pressure. Some also use height based σ coordinates, as height has the advantage of not being dependent on time (Pielke Sr, 2013).

In nonhydrostatic models, the incorporation of topography causes numerous metric terms in the equations when using terrain-following vertical coordinates based on height coordinates. Laprise (1992) developed an alternative formulation of the Euler equations where no metric terms appear by introducing terrain-following coordinates based on hydrostatic pressure. This coordinate has the interesting property that equations have a form that is similar to the hydrostatic equations in isobaric coordinates - even with nonhydrostatic conditions. This system uses hydrostatic pressure as the independent variable and it features a number of useful properties such as automatically reverting into the isobaric coordinate system when nonhydrostatic effects are neglected. The Euler equations expressed in a terrain-following version of this hydrostatic-pressure coordinate system are very similar to the hydrostatic equations in pressure coordinates. One widely known model which uses this form of vertical coordinate is WRF.
σ surfaces flatten out near the model top. In other words, the influence of the terrain is reduced in upper levels, as shown in Fig. 4.3.

4.2 Vertical Coordinate of WRF

The vertical coordinate η used in WRF is defined as follows (Skamarock et al., 2008):

$$\eta = \frac{p_h - p_{ht}}{p_{hs} - p_{ht}} \tag{4.4}$$

p_h is the hydrostatic component of the pressure and p_{ht} and p_{hs} stand for the hydrostatic component of the pressure on the top respectively surface boundaries. η varies from a value of 0 at the upper boundary to 1 at the bottom (Fig. 4.3).
These terrain-following coordinates based on vertical hydrostatic-pressure coordinates are also referred to as terrain-following mass vertical coordinate because the denominator

$$p_{hs} - p_{ht} =: \mu(x, y) \tag{4.5}$$

represents the mass unit per area within the air column.

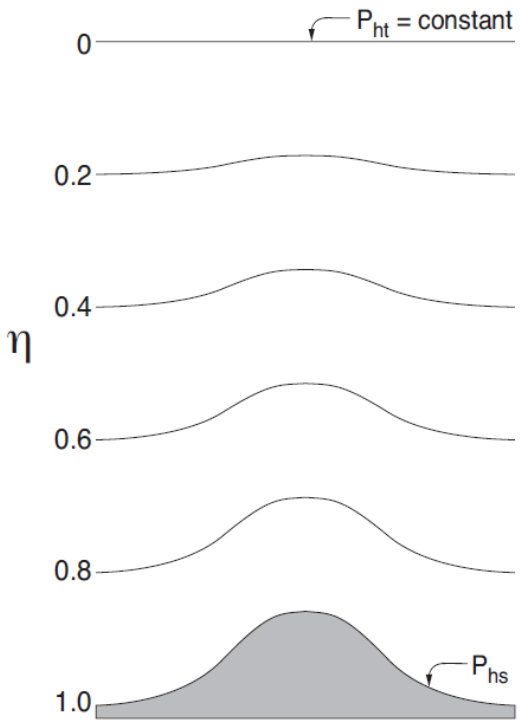

Figure 4.3: WRF-ARW η levels. p_{ht} and p_{hs} stand for the hydrostatic component of the pressure on the top respectively surface boundaries. (Skamarock et al., 2008)

4.3 Hybrid $\sigma - p$ Coordinates

Eckermann (2009) stated that there are numerical and practical advantages of choosing isobaric surfaces instead of terrain-following as model levels in higher levels, such as the upper troposphere or the stratosphere. This is accomplished by using a function that smoothly merges terrain-following coordinates in lower atmospheric levels to isobaric surfaces in higher levels, which was initially proposed by Simmons and Strüfing (1981):

$$p(\tilde{\eta}, p_S) = \hat{A}(\tilde{\eta})p_0 + \hat{B}(\tilde{\eta})p_S \tag{4.6}$$

p_0 is a nominal sea level pressure, typically 1000 hPa. $\tilde{\eta}$ is the vertical profile of η for $p_S = p_0$. It is independent from p_S and therefore constant in horizontal space. A newer form of this equation, generalized for nonzero p_{top} leads to:

$$p(\tilde{\eta}, p_S) = A(\tilde{\eta}) + B(\tilde{\eta})(p_S - p_{top}) \tag{4.7}$$

One obtains the explicit version for η if p is replaced in Eq. (4.2) with the definition given in Eq. (4.7):

$$\eta = \frac{p - p_{top}}{p_s - p_{top}} = \frac{A(\tilde{\eta}) - p_{top}}{p_S - p_{top}} + B(\tilde{\eta}) \tag{4.8}$$

such that $p_{top} \leqslant A(\tilde{\eta}) \leqslant p$ and $0 \leqslant B(\tilde{\eta}) \leqslant 1$. The two coefficients A and B - respectively their vertical profiles - control and define the vertical levels. This is a combination

of terrain-following and pressure coordinates, which can be easily seen if one of the coefficients is set to 0. On the one hand, $A = 0$ yields exclusively terrain-following coordinates. On the other hand $B = 0$ cause simply isobaric surfaces. Compared to pure σ coordinates, hybrid $\sigma - p$ coordinates have reduced terrain influence (Fig. 4.2). This form of vertical coordinates is used in the atmospheric general circulation model of ECMWF, the ECMWF IFS.

4.4 Vertical Coordinate of ECMWF

The ECMWF forecasting system consists of several components. One of these is the atmospheric general circulation model which is coupled to an ocean wave model. For the horizontal representation, ECMWF uses dual representation of spectral components and gridpoints. As the meridians converge towards the poles, it is computationally cheaper to use a *reduced Gaussian grid*. This keeps the east-west distance between two gridpoints almost constant by reducing the number of gridpoints polewards. Additionally, spectral representation is used for a subset of prognostic variables.
The vertical coordinates are finest in the lower levels within the planetary boundary layer where they are terrain following. Upper levels are levels of constant pressure. In between those two different vertical coordinates, there is a smooth transition from one coordinate system to the other (Andersson, 2015).
Since June 2013, ECMWF uses 137 vertical levels and a model top in 0.01 hPa, increasing the number of levels uniformly though the whole atmosphere from previously 91.

Bauer et al. (2013) observe just slight benefits from increasing the number of vertical levels compared to the great benefits from increasing the horizontal grid distance where topography and convection and thus many meteorological parameters are more realistically predicted. The vertical resolution increase is most effective in areas of strong vertical gradients, e.g. in frontal zones or in the planetary boundary layer. This is also where systematic model errors are most distinctive. A higher vertical resolution causes more variability and thus sometimes even negative skills compared to a less resolved model. This is one of the reasons why the vertical resolution is updated less frequently than the horizontal, next to other reasons like the strong dependency of data assimilation and parametrizations on vertical resolution (Bauer et al., 2013).

The ECMWF vertical levels contain the prognostic variables wind U and V, the temperature T and the specific humidity q which are defined at NLEV model layers. NLEV is the number of vertical levels. In between those layers are so called "half-levels", where the pressure and thus the vertical levels are given by:

$$p_{k+1/2} = A_{k+1/2} + B_{k+1/2} p_s \tag{4.9}$$

$A_{k+1/2}$ and $B_{k+1/2}$ are constants whose values effectively define the vertical coordinate (Ritchie et al., 1995). At the lowest level $p_{NLEV+1/2}$, the constants are $A = 0$ and $B = 1$ and thus the lowest model level is $p_{NLEV+1/2} = p_s$. The lowest model level follows the surface. At upper levels ($A \neq 0$ and $B = 0$), the surface pressure vanishes and the model

levels are pure pressure levels independent of topography (see Fig. 4.4). There is a smooth transition between pressure coordinates in the upper levels and terrain-following in the lowest level, where A and B are both greater than 0. These values for A and B are shown in Table 4.1.

Table 4.1: The definition of the ECMWF model levels k as currently in use. A and B are the coefficients defining the levels. The geometric altitude z and the pressure $p_{k+1/2}$ at the corresponding half-level layers are based and computed upon definitions of the ICAO Standard Atmosphere (ECMWF, 2013)

k	A [hPa]	B	$p_{k+1/2}$ [hPa]	z [m]
1	2.000365	0.000000	0.0200	80301.65
2	3.102241	0.000000	0.0310	74584.91
3	4.666084	0.000000	0.0467	71918.79
.....	.....	.....	.....	.....
135	3.757813	0.995003	1008.2239	53.92
136	0.000000	0.997630	1010.8487	30.96
137	0.000000	1.000000	1013.2500	10.00

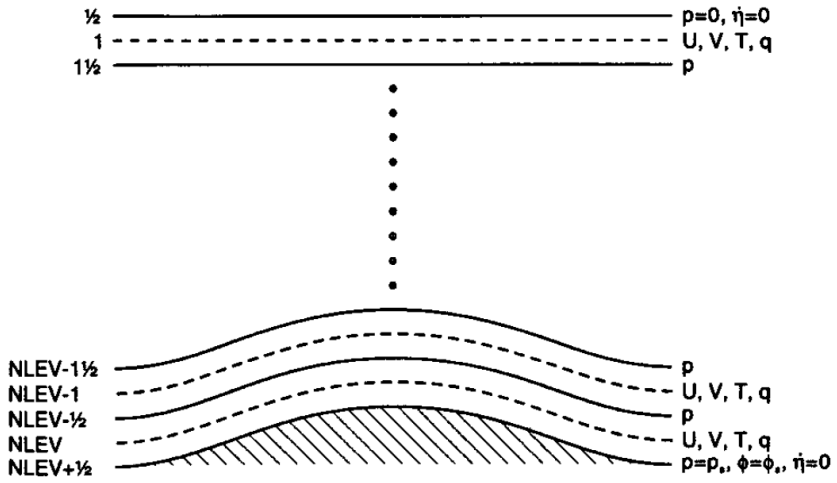

Figure 4.4: Vertical distribution of variables in the general circulation model of ECMWF. The number of levels are shown on the left side, the defined variables on the right side (Ritchie et al., 1995).

4.5 New vertical Coordinates

Terrain-following coordinates have important advantages (Schär et al., 2002):

- They map the atmosphere with a rectangular computational grid which is well suited for implementation on digital computers.
- The level closest to the topography features a vanishing vertical wind which allows certain simplifications of lower boundary conditions.

- The unequal spacing of computational levels allows an easy method to couple the model's dynamical part with the implementation of boundary and surface-layer parameterization schemes (again due to the level closest to the surface).

However, there are some disadvantages of terrain-following coordinates. When steep slopes are present in the topography, some patterns that are smooth in physical space may instead have very strong and rough patterns in the computational space. For instance, there is a detrimental impact caused by the numerical formulation of the pressure gradient term. Truncation errors associated with the deformation of the computational mesh have the same order of size or can even be greater than the classical regular-grid truncation error. These and other problems become even more evident when using high horizontal resolution models. In order to avoid numerical problems, the topography is usually digitally filtered or smoothed, although smoothing causes new problems such as underestimation of orographic blocking effects.

Therefore, Schär et al. (2002) proposed a new vertical coordinate system to cope with numerical problems over rough topography.

4.5.1 Smooth Level Vertical Coordinate (SLEVE)

SLEVE coordinates allow much smoother computational meshes and reduce the transformation or truncation errors that were mentioned above. The idea is to implement a scale-dependent decay of topography influence with height that assures that small-scale features decay at a faster rate than large-scale features. Fig. 4.2 (bottom) shows SLEVE levels in comparison to pure terrain-following and hybrid coordinates. With terrain-following coordinates, the shape of the terrain is still present even in upper levels. Hybrid levels provide a linear transition to pressure levels. But still, some upper levels are quite rough. SLEVE coordinates on the other hand show no imprint of the small-scale topography variations in upper levels. Only large-scale features are still present to a certain degree.

Later, Leuenberger et al. (2010) point out that terrain-following coordinates - but especially SLEVE coordinates - tend to compress vertical levels near mountain tops and cause very thin model layers. Since the slope of vertical levels may be very steep in these regions, a part of the horizontal advection in physical space goes into vertical advection terms in numerics. Large vertical advections force the model to use a small time step to be numerically stable. This causes undesired computational costs. In addition, assumptions of the planetary boundary layer schemes may be invalid if the first prognostic model level lies too close to the surface. This is why a renewed SLEVE formulation, which reduces the compression of the lowest levels to a large extent, was presented .

SLEVE coordinates have the following form:

$$z(x, y, Z) = Z + h_1(x, y)/b_1(Z) + h_2(x, y)/b_2(Z) \tag{4.10}$$

where z is the height, x and y are the horizontal coordinates and Z is a height-based vertical coordinate. The model orography h is split into a small-scale part h_2 and a large-

scale counterpart h_1, what is done by a digital filter, so that $h = h_1 + h_2$. The coefficients b_1 and b_2 determine the vertical levels. By using a generalized decay function for these coefficients, an exponential decay as well as the reduced compression of the lowest levels can be implemented.

5 Data and Methodology

5.1 Error Measures

5.1.1 Bias

Numerical weather predictions often contain systematic errors. They are usually rather small in short-range forecasts, but in longer-range forecasts, the error may get larger due to the drifting of a model into a preferred state (Jolliffe and Stephenson, 2003). An error measure for systematic errors is the bias b (Stanski et al., 1989; Jolliffe and Stephenson, 2003):

$$b = \frac{1}{N}\left[\sum_{i=1}^{N}(F_i - O_i)\right] \tag{5.1}$$

N is the number of forecasts, F_i represents the value of the i-th forecasts and O_i the corresponding observational value. To be more general, an observation operator H allows the comparison of different physical quantities:

$$b = \frac{1}{N}\left[\sum_{i=1}^{N}(\mathrm{H}(F_i) - O_i)\right] \tag{5.2}$$

The convention is to subtract the observation from the forecast so that a positive bias indicates higher values in the forecast compared to the observation. The bias does not provide information about the magnitude of the error but only the deviation from the observations. This is one reason why the bias should never be presented alone without other error measures.

5.1.2 Root Mean Square Error (RMSE)

The mean square error (MSE) respectively the square root of this quantity, the RMSE, are probably the most widely used error measures in meteorology. The RMSE is given by (Stanski et al., 1989):

$$RMSE = \left[\frac{1}{N}\sum_{i=1}^{N}(\mathrm{H}(F_i) - O_i)^2\right]^{\frac{1}{2}} \tag{5.3}$$

Again, N is the number of forecasts, F_i represents the value of the i-th forecasts and O_i the corresponding observational value. Because of the square, the RMSE is more sensitive to large errors compared to the mean absolute error (MAE) which sums the

absolute errors instead of the square errors. Also from a user's perspective, it may seem preferable and useful to penalize large errors. Problems with RMSE could arise from outliers in the sample, caused by data corruption or atypical events, where the RMSE is oversensitive (Jolliffe and Stephenson, 2003). Both MAE and RMSE have in common that they do not indicate the direction of the deviation. A disadvantage of RMSE compared to MAE is that conservative forecasts may be encouraged as they have a forecast closer to the climatological mean and avoid large errors which are strongly punished by RMSE (Stanski et al., 1989).

5.1.3 SAL (Structure-Amplitude-Location)

Traditional quality measures like root-mean-square error (RMSE), bias or anomaly correlations are reasonably simple and thus often used for verification in numerical weather prediction. However, precipitation is often measured in terms of categorical verifications scores, which require the specification of thresholds. Whereas synoptic scale structures are appropriately verified by gridpoint-based error measures, the limitations of those error measures is often described as follows (Wernli et al., 2008):
A precipitation field, that is correct in size, amplitude and timing but incorrect in location (see (a) or (b) in Fig. 5.1) is very poorly rated by categorical error scores and the RMSE. In that case, the RMSE is even worse than a forecast that completely missed the event. This is because the RMSE has a value greater than zero in the area where the forecast placed a precipitation field whereas no precipitation is observed in this. Vice versa the RMSE is greater than zero where precipitation is observed but not forecasted. This fact is often referred to as "double penalty problem". Therefore, global models or models with rough resolution may reach better error measures because big forecasted precipitation fields may include the actual observed smaller field. Also nor the nature neither the degree of the error are considered which are other disadvantages of the RMSE.
The double penalty problem led to new approaches of quantitative verifications that can be divided into three groups:

- "Fuzzy" scores consider neighboring gridpoints.
- Techniques, that focus on spatial scales, such as wavelet decomposition.
- Object-based approaches that identify precipitation objects.

Wernli et al. (2008) developed a new object-based error measurement system, called SAL (S for structure, A for amplitude and L for location).

The computation of the location and structure components require the definition and identification of precipitation objects. One of the easier methods to define those objects is to set a threshold value R^*:

$$R^* = fR^{max} \tag{5.4}$$

R^{max} is the maximum value of precipitation within the domain. The choice of the coefficient f is empiric. However, in this thesis it was regarded as more practical to choose

an absolute value as threshold. SAL was developed for accumulated precipitation but in this work, precipitation rates are verified. If the precipitation is very weak, the often used value for $f = 1/15$ leads to problems. Therefore, in this work, R^* is set to an absolute value of 0.05 mm/h.
The identified precipitation objects are denoted as $\mathcal{R}_n, n = 1..., M$ with M being the number of objects in the domain $\mathcal{D}$.
A perfect forecast is $S = A = L = 0$. A few examples for different configurations and the resulting values for each component can be seen in Fig. 5.1. The three components of SAL are described in detail in the following sections.

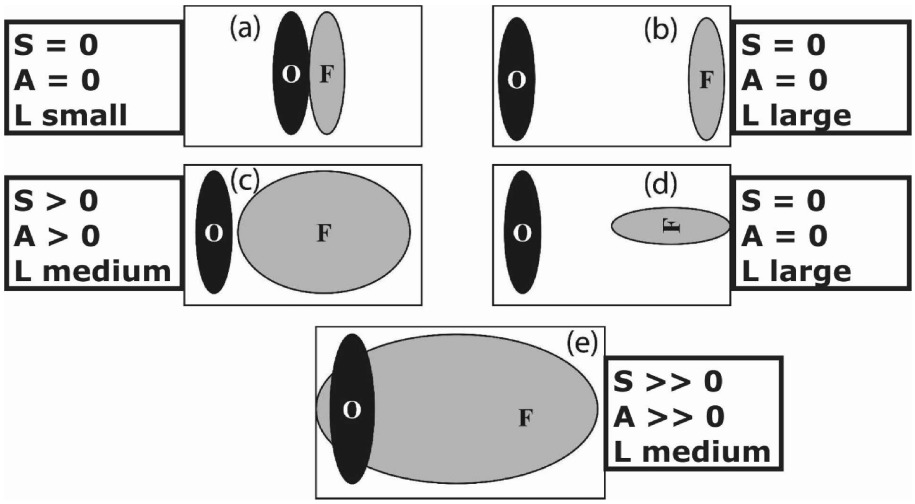

Figure 5.1: Qualitative examples of SAL of various forecast and observation combinations of precipitation fields. Precipitation rates are assumed to be uniform in all objects (Wernli et al., 2008).

The amplitude component (A)

The amplitude corresponds to the domain-averaged precipitation total. It compares the normalized difference between the observation and forecast:

$$A = \frac{D(R_{mod}) - D(R_{obs})}{0.5[D(R_{mod}) + D(R_{obs})]} \tag{5.5}$$

$D(R)$ is the domain average of the precipitation R:

$$D(R) = \frac{1}{N} \sum_{(i,j)\in\mathcal{D}} R_{ij} \tag{5.6}$$

R_{ij} are the precipitation gridpoint values in the domain. A is within $[-2 \ldots +2]$, while 0 corresponds to a perfect forecast.

The location component (L)

The location component L consists of two inputs, $L = L_1 + L_2$. L_1 is the normalized distance between the center of mass of the modeled and observed precipitation fields:

$$L_1 = \frac{|\mathbf{x}(R_{mod}) - \mathbf{x}(R_{obs})|}{d} \tag{5.7}$$

where d is the largest possible distance between two gridpoints and $\mathbf{x}(R_{mod})$ or $\mathbf{x}(R_{obs})$ denote the centers of mass of the modeled and observed rain fields. L_1 is in the range of [0 ... 1]. $L_1 = 0$ refers to identical centers of mass but not to a perfect location since different precipitation fields may have the same center of mass. For instance, a precipitation field in the center of the domain as well as two fields placed symmetrically to the left and the right of the center would yield $L_1 = 0$. Taking account of this circumstance, a second part L_2 allows to distinguish between individual centers of mass. For every precipitation object $\mathcal{R}_n$, the integrated amount of precipitation R_n is calculated as

$$R_n = \sum_{(i,j)\in\mathcal{R}_n} R_{ij} \ . \tag{5.8}$$

The weighted averaged distance r between the centers of mass of the individual objects $\mathbf{x}_n$ and the total center of mass $\mathbf{x}$ is as follows:

$$r = \frac{\sum_{n=1}^{M} R_n |\mathbf{x} - \mathbf{x}_n|}{\sum_{n=1}^{M} R_n} \tag{5.9}$$

Finally, the weighted averaged distance of the forecast and the observation is compared and normalized to [0 ... 1]:

$$L_2 = 2\left[\frac{|r(R_{mod}) - r(R_{obs})|}{d}\right] \tag{5.10}$$

L_2 considers the averaged distance from the center of mass of all precipitation fields to each individual field. L is then in the range of [0 ... + 2]. But still, L is not perfect and different precipitation fields may have the same location component. For instance, it is not sensitive to rotation around the center of mass. So $L = 0$ does not conclude that the modeled and observed fields are completely coincident.

The structure component (S)

The structure provides information about the volume of normalized precipitation objects as well as shape and size. However, it does not include information about the amount or amplitude of precipitation. After having identified the individual precipitation objects, each scaled volume V_n is calculated as a sum and can subsequently be expressed without the sum using Eq. 5.8:

$$V_n = \sum_{(i,j)\in\mathcal{R}_n} R_{ij}/R_n^{max} = R_n/R_n^{max} \tag{5.11}$$

R_n^{max} is the maximum gridpoint value in the n-th precipitation field. This is a scaling method to make the structure component uncorrelated with the amplitude component.

For both observation and forecast, the scaled volumes are weighted with the integrated amount of precipitation R_n and put together in a weighted mean:

$$V(R) = \frac{\sum_{n=1}^{M} R_n V_n}{\sum_{n=1}^{M} R_n} \tag{5.12}$$

The structure component S is the difference of the weighted mean volume for the forecast and the observation, normalized to $[-2 \ldots +2]$:

$$S = \frac{V(R_{mod}) - V(R_{obs})}{0.5[V(R_{mod}) + V(R_{obs})]} \tag{5.13}$$

The key characteristic of the structure component is that it is able to distinguish between convective and stratiform precipitation, since the former is more concentrated in space and the latter is widespread.

5.2 Data

The aim of this thesis is to reach better short-range (72 hours) forecast scores for Mediterranean cyclogenesis. For that, 14 cases were chosen which are all shown in Table 5.1 and consecutively numbered according to chronological order.

5.2.1 Cases chosen

All of the 14 cases occurred after the last upgrade of the ECMWF model resolution in June 2013 (Bauer et al., 2013), where the number of vertical levels was increased. The idea is that all of the cases should be comparable and no major change in the formulation of the ECMWF model should have happened in the considered time interval. All cases were noteworthy precipitation events in the Eastern Alps. Heavy precipitation over eastern Austria would be preferable which is often linked to the presence of a Vb-low (e.g. the 12^{th} case in table 5.1) or at least a Vb-like-low (e.g. the 7^{th} or the 8^{th} case). Since the available time window was shorter than two years, there were not enough Vb cases. However, at least some of the cases actually had strong precipitation in Eastern Austria (7^{th}, 8^{th} or 9^{th} case in table 5.1). For other cases, the operational WRF forecast heavy precipitation which did not occur then, e.g. the 13^{th} case. The operational WRF forecast is the 1. configuration in this study, named CONTROL16, as defined in section 5.3.

All of the time intervals are chosen such that most of the cyclogenesis is within the model run. The heaviest precipitation usually occurs between 24 and 48 hours after initialization.

5.2.2 Domain

The model domain should be large enough to cover all areas where nothern Mediterranean lows evolve and move but should also not cut through high mountain ridges at the domain borders. This is why the domain may be a little bit more elongated to the west

Table 5.1: Chosen dates for WRF runs. Displayed dates are the dates for model initialization. Time of day is always 0 Z. Forecast ranges are 72 hours.

1.	2013-09-15
2.	2014-01-19
3.	2014-03-22
4.	2014-05-14
5.	2014-07-20
6.	2014-07-28
7.	2014-08-31
8.	2014-09-10
9.	2014-09-12
10.	2014-11-04
11.	2015-01-23
12.	2015-01-29
13.	2015-02-04
14.	2015-02-23

than necessary. Countries like Ireland or Portugal are still included. Large parts of the Mediterranean should be located within the domain, that includes southern Spain, Sicily or the Peloponnese. Bulgaria and most parts of Romania are within the domain in the east, Germany and Poland in the north. The domain lies between latitudes 36.45° and 55.82° N and longitudes 10.47° W and 28.47° E. A map of the domain is shown in Fig. 5.2.

5.2.3 Verification Sources

Several observations are used for verification.

Radio soundings: Radio soundings are one of the most reliable observations in the atmosphere. They measure temperature, dewpoint, wind and geopotential height of pressure levels. Since the area of interest is not the whole domain, the soundings were chosen in the area where most of the cyclogenesis usually happens, that is the Gulf of Genoa or the Adriatic Sea and all adjacent areas. Concerning precipitation, most parts of Central Europe are of great interest. This is why stations in many countries surrounding Austria are also included. Another major requirement was that the ascents of radiosondes take place on a regular basis at 0 Z and 12 Z, so that all observations are easily comparable. This means, that there are seven soundings for each location for each case in the 72 hours of forecast. 26 radio sounding stations match the requirements, eight of them lie within the nested domain - respectively in the Alpine region. All radiosondes are listed in Table 5.2. Fig. 5.2 shows their location within the domain.

VERA: The "Vienna Enhanced Resolution Analysis" is a mesoscale real-time analysis tool developed at the "Institut für Meteorologie und Geophysik der Universität Wien". The tool takes the information from weather stations and displays the spatial distribution of several meteorological parameters. Many methods have been implemented

Station number	Name of location
07761	Ajaccio
13275	Beograd
16320	Brindisi
12843	Budapest
16113	**Cuneo-Levaldigi**
10410	Essen
10618	Idar-Oberstein
10771	Kümmersbruck
12374	Legionowo
10393	Lindenberg
10548	Meiningen
16080	**Milano**
10868	**München-Oberschlossheim**
07645	Nimes-Courbessac
06610	**Payerne**
11952	Poprad-Ganovce
11520	Praha-Libus
16245	Pratica Di Mare
11747	Prostejov
10739	Stuttgart
12982	Szeged
16044	**Udine**
11035	**Wien**
12425	Wroclaw
14430	**Zadar**
14240	**Zagreb**

Table 5.2: Chosen radio soundings for WRF verification. Stations in bold font are within the nested domain.

to gain better results than one would get from simple spatial interpolation. For example, the measured values are combined with measurement-independent a priori information due to topographic forcing (Steinacker et al., 2006). Furthermore, a quality control, that is based on data self consistency, is implemented. It offers objective correction proposals for each observation (Mayer et al., 2012). VERA splits the observed fields into an unexplained part and an explained part. The explained part quantifies the influence of factors like height or land-sea mask. The unexplained part contains the rest. With this method, it is possible to project the meteorological fields onto almost any topography.
VERA is used for verification of mean sea level pressure (MSLP), 2 m temperature and specific humidity and is available at every full hour since March 2014. Therefore, the first two cases in Table 5.1 were not available in VERA.

Weather radar: Weather radars deliver information about precipitation. This is not ideal for the verification with SAL as it only provides precipitation rates at a specific

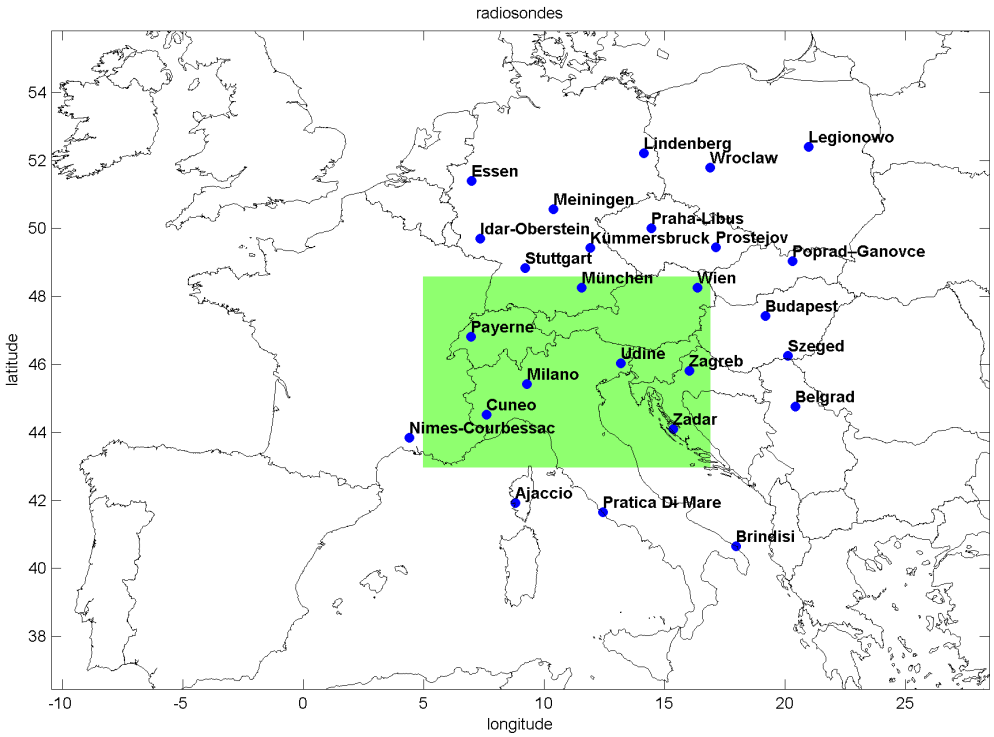

Figure 5.2: Location and names of all 26 used radiosondes in the verification. The map sector is equivalent with the domain used in all WRF runs. The green central area indicates the nested, high-resolution domain for HYBRID1.

moment and not accumulated precipitation values. However, at the time of this work, weather radar was the only observation available for object-based precipitation verification.

The used data comes from CERAD, the Central European Radar Data Network, where eleven countries are involved. Those countries include Belgium, Germany, the Netherlands, Croatia, Austria, Poland, Switzerland, Slovakia, Slovenia, the Czech Republic and Hungary. Since the CERAD-composite consists of several national radar data, the Z-R relation is different in each country. In general, the Z-R relation describes the relation of precipitation rate R in mm/h and the radar reflectivity factor Z in $\mathrm{mm^6m^3}$ (Brugger, 2004):

$$Z = aX^b \tag{5.14}$$

where a and b are empirical coefficients that have to be specified. The distribution of droplet sizes is generally unknown, which makes it impossible to specify a universally valid Z-R relation. If the worst comes to the worst the relative error can go up to 50 %. The relation used in this work is the one that is common in Austria:

$$Z = 200R^{1.6} \tag{5.15}$$

The radar reflectivity is usually given in dBZ. The dBZ-values are defined as follows:

$$\mathrm{dBZ} = 10 \log_{10} \left(\frac{Z}{Z_0} \right) = 10 \log_{10}(Z) \tag{5.16}$$

where Z_0 is $1\,\mathrm{mm}^6\mathrm{m}^3$. If one combines Eq. 5.14 and 5.15, a simple conversion from dBZ to the rain rate R is the result:

$$R = 10^{\mathrm{dBZ}/16} 200^{-5/8} \tag{5.17}$$

Unfortunately, not all 14 cases are covered with provided CERAD data. The year 2013 is not available which makes the first case not accessible for radar verification. dBZ does not refer to a precipitation rate of 0 mm/h because of the definition with the logarithm. A radar reflectivity of $\mathrm{dBZ} = 0$ corresponds to a precipitation rate of $R \approx 0.0365\,\mathrm{mm/h}$. To avoid computational problems with a precipitation rate of 0.0365 mm/h as it takes up the whole domain, all those values are set to $R = 0\,\mathrm{mm/h}$.

5.3 WRF Runs

Different configurations are run in WRF. Since the sea surface temperature (SST) is considered to be crucial for a good forecast of Mediterranean cyclogenesis, the SST from ECMWF is replaced by high-resolution SST data. All runs share many configurations, which are as follows:

Global model: The global model is the Integrated Forecasting System (IFS) from the European Centre for Medium-Range Weather Forecasts (ECMWF).

Number of vertical levels: All runs have the same number of vertical levels, namely 41 levels.

Microphysics: WRF Single-Moment 6-class scheme with ice, snow and graupel precesses

Longwave radiation: RRTMG scheme, that accounts for multiple bands and microphysics species and includes a method of random cloud overlap

Shortwave radiation: RRTMG shortwave scheme that includes a method of random cloud overlap

Planetary boundary layer (PBL): Mellor-Yamada Nakanishi and Niino Level 2.5 order PBL scheme. It includes sub-grid turbulent kinetic energy terms.

Cumulus parameterization: Grell 3D, which is a scheme that may also be used on high resolutions

Vertical velocity damping: Vertical motion is damped to prevent instability with large vertical velocities

Lateral boundary options: The first row and column are specified with external model values (from ECMWF). The next four rows and columns are blended values of the external model and WRF.

Further information about these and more configuration options can be found in Wang et al. (2015).

Following different configurations are run with all cases given in Table 5.1:

CONTROL16: 1. configuration of WRF with pressure level initialization from ECMWF. There are 25 ECMWF pressure levels, starting from 1000 hPa to 1 hPa as shown in Table 5.3. The ECMWF topography is used as topography for WRF. The correspondent topography can be seen in Fig. 5.3. The horizontal resolution is 4 km which is almost a forth of the resolution of ECMWF. Therefore, the topography from ECMWF can be considered as strongly smoothed.

Table 5.3: ECMWF pressure levels as used in the WRF initialization in hPa.

1	10	100	400	850
2	20	150	500	900
3	30	200	600	925
5	50	250	700	950
7	70	300	800	1000

HYBRID16: 2. configuration which is the same as above but with an initialization on 137 ECMWF hybrid levels instead of 25 pressure levels. Therefore, meteorological information is available on more levels compared to pressure initialization.

HYBRID4: 3. configuration. Again, WRF is run with ECMWF hybrid level initialization. However, a slightly smoothed topography is used, as provided by the WRF model (Fig. 5.4). The smoothing is necessary to avoid numerical instability. But still, this topography is much more realistic compared to the topography in the first two groups of experiments.

HYBRID1: 4. configuration. As the topography in the Greater Alpine Region is supposed to have a great influence on cyclogenesis, a nested domain in this area is used. The parent domain stays as described above. The nested domain lies between latitudes 42.96° and 48.57° N and longitudes 4.97° and 16.88° E and has a horizontal resolution of 1.33 km, that is a factor of 3:1 compared to the parent domain. As the aim was to get the best topography possible, a simple smoothing was considered as unsatisfactory. Especially in this resolution, many valleys and basins are visible and therefore, a lot of slopes and mountain ridges would have been smoothed. A limitation of the maximum slope seemed to be a much better solution. The topography is shown in Fig. 5.5. By trial and error, a maximum slope of 30 percent was found to be approximately the upper limit where the model could run stable with a reasonable time step. The valleys and basins remain at the same height, only

mountains with too steep slopes are lowered. As a result, only approx. 4.5 percent of the gridpoints are changed, whereas with simple smoothing, the topography at almost every gridpoint would have been changed.

All four configurations are shortly summarized in Table 5.4.

Table 5.4: Summary of all four different configurations that were run with WRF.

configuration	Initialization (ECMWF)	Resolution [km]	Topography [km]
CONTROL16	Pressure levels	4	ECMWF (approx. 16)
HYBRID16	Hybrid levels	4	ECMWF (approx. 16)
HYBRID4	Hybrid levels	4	4
HYBRID1	Hybrid levels	4 and 1.33	4 and 1.33

The aim was to change as little as possible between the different runs aside from those changes mentioned above. Some little adoptions with the time step had to be done to keep the model stable at higher resolutions. However, it is supposed to have only negligible influence on the results. For realistic results, some little modifications were done in the model physics: In the highest resolution (HYBRID1), slope and shading effects were added, namely two schemes influencing the radiation budgets. The option slope_rad modifies the surface solar radiation flux according to terrain slope. The option topo_shad allows shadowing of neighboring grid cells (Andersson, 2015).

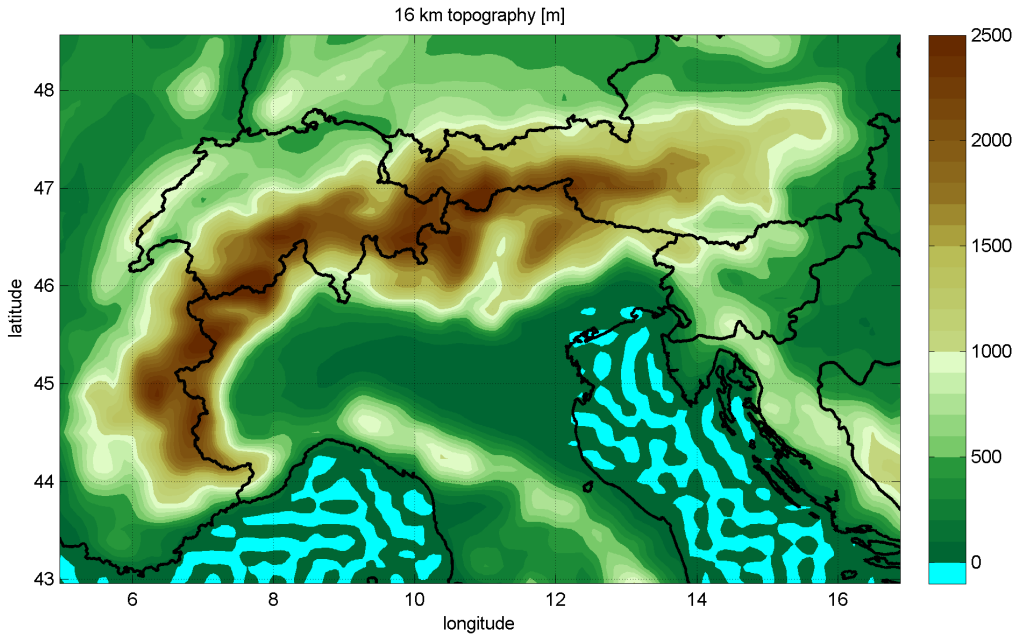

Figure 5.3: ECMWF topography, as used in the first two groups of runs (CONTROL16 and HYBRID16). The wave-like pattern in the sea is a remnant of the spectral method of ECMWF. The altitude is given in meters.

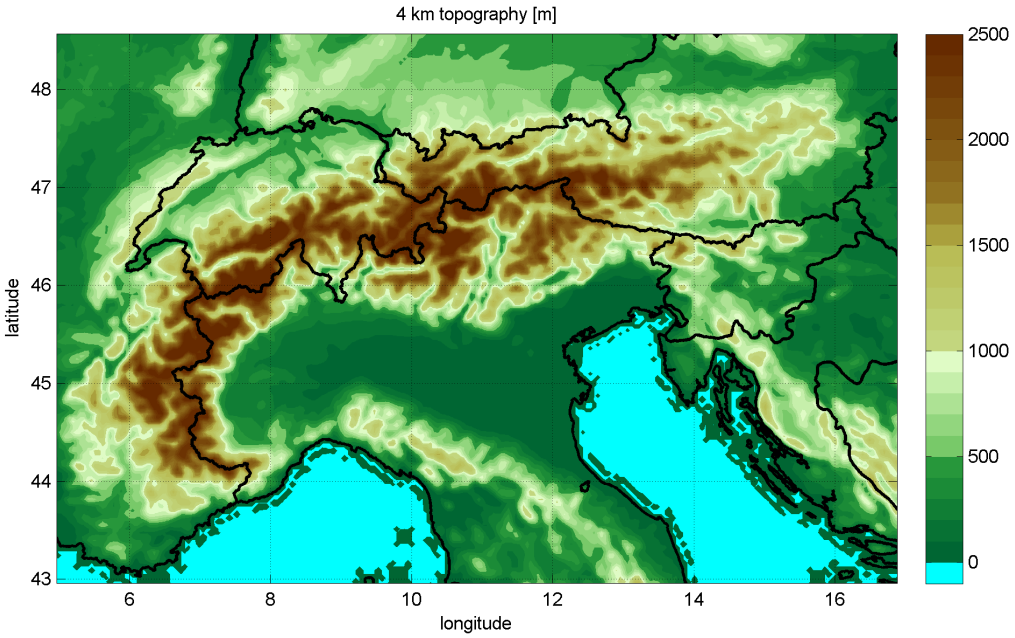

Figure 5.4: Slightly smoothed 4 km topography for HYBRID4, generated with WRF.

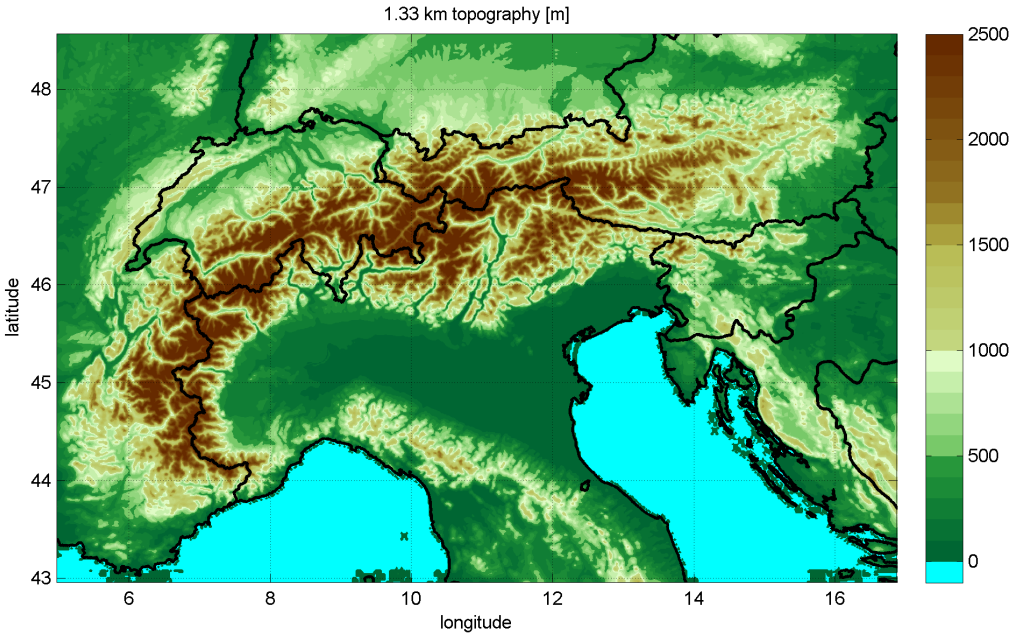

Figure 5.5: 1.33 km topography with limited slopes (30 % limit), as used for HYBRID1.

6 Case Studies

6.1 13th Case: 2015-02-04 until 2015-02-07

One case that stands out in many error measures with the largest errors is the one initialized on 2015-02-04. At the time of initialization at 0 UTC, a large trough in 500 hPa covers a big part of Europe. This trough includes a smaller trough over Ukraine and a cut-off low in France and northern Spain. A low pressure system already exists in the western Mediterranean Sea featuring two cores, one in eastern Spain and one with even lower pressure over Corsica (Fig. 6.1).

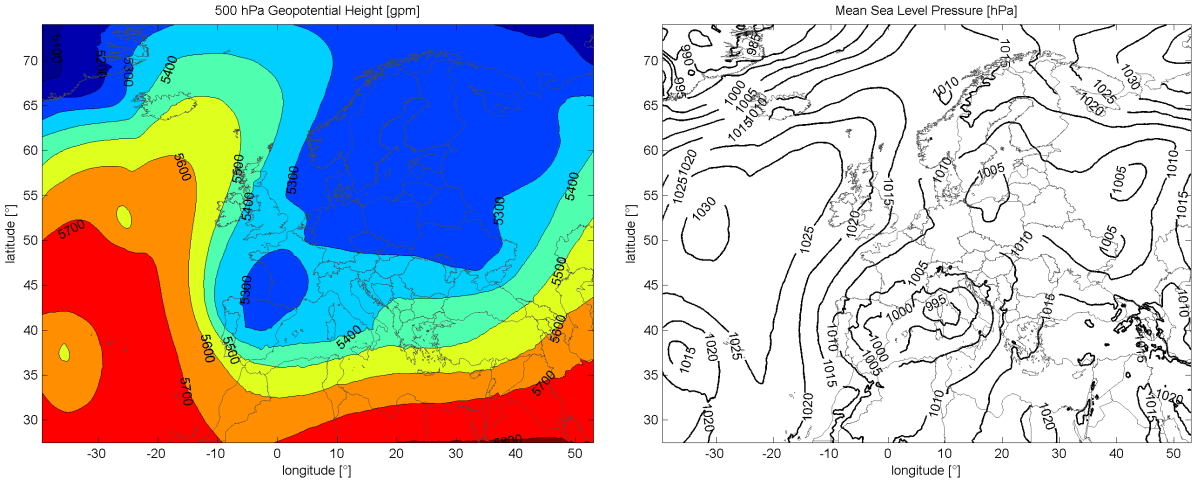

Figure 6.1: Synoptic weather conditions for 2015-02-04 0 UTC. The left panel shows the 500 hPa geopotential height in gpm, the right panel the mean sea level pressure in hPa. The data is from the analysis time step of the ECMWF run at 2015-02-04 0Z.

The cut-off low over France moves further south. 36 hours later, the cut-off low is located in northern Algeria. The low pressure system at sea level moves slowly eastwards. The eastern core over Corsica weakens, the western core strengthens as it moves from Spain towards Italy (Fig. 6.2). The strong pressure gradient over the Alps increases. Since there are no reliable observations of the upper atmosphere aside from a few radio soundings, the analysis time step of global models is considered to describe the atmospheric state.

The precipitation in the northernmost part of Italy as well as south of the main chain of the Alps in Austria starts around 24 hours after initialization and lasts approximately till the end of the run on 2015-02-07 at 0 UTC.

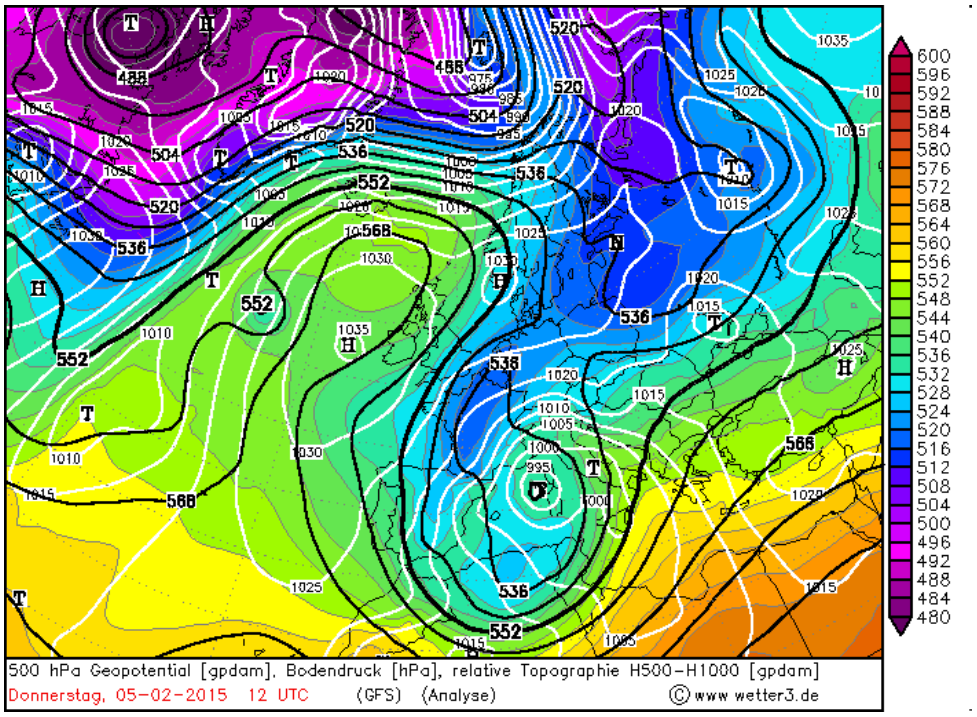

Figure 6.2: Synoptic weather conditions for 2015-02-05 12 UTC (36 h after initialization). The white lines indicate the mean sea level pressure in hPa and the black lines indicate the relative topography which is the difference in gpdam of the 1000 hPa and 500 hPa level. The filled color fields show the 500 hPa geopotential height in gpdam. The data is from the analysis time step of the GFS run at 2015-02-05 12Z. Source: `http://www1.wetter3.de/Archiv/`

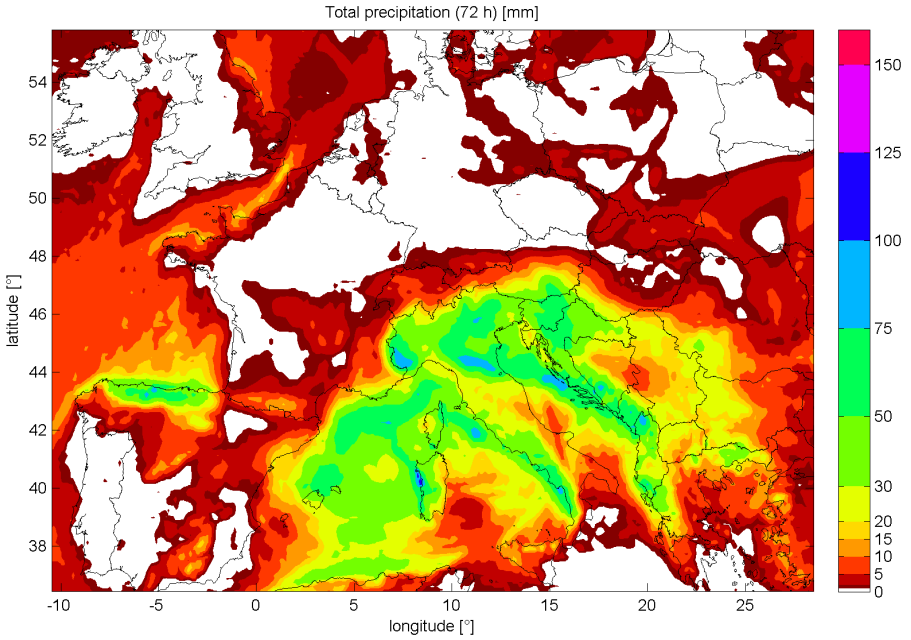

Figure 6.3: Total precipitation forecast of ECMWF from 2015-02-04 at 0 UTC until 2015-02-07 (72 hours) at 0 UTC. The initialization time is 2015-02-04 at 0 UTC.

To allow a comparison, the precipitation forecast totals of ECMWF and WRF are provided in Fig. 6.3 and 6.4. The most striking difference is between Fig. 6.3 and all four WRF configurations in Fig. 6.4, also the ones with ECMWF topography on top. However, orographic effects seem to be at least partially responsible for stronger precipitation hot spots. Overall, in WRF, the precipitation fields are a little bit shifted to the north, especially in southern Italy, Greece and many countries further north, e.g. Austria, Hungary, Poland and Romania. The difference is quite big in Vienna and lower Austria where there is hardly any precipitation in the ECMWF forecast but as much as 20 mm and more in the WRF forecasts.

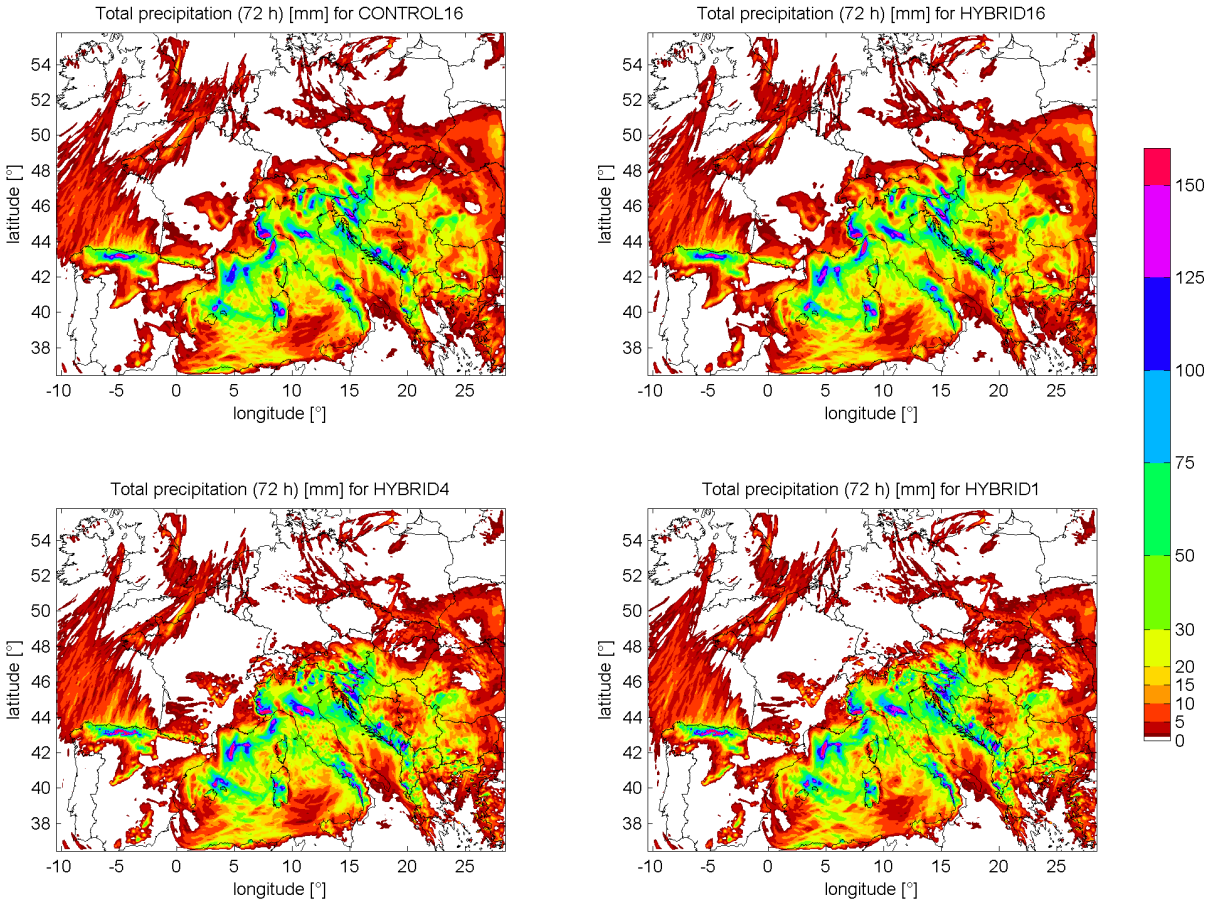

Figure 6.4: Total precipitation forecasts for all four WRF runs from 2015-05-04 until 2015-02-07 (72 hours) at 0 UTC. The initialization time is always 2015-02-04 at 0 UTC. Top left: CONTROL16. Top right: HYBRID16. Bottom left: HYBRID4. Bottom right: HYBRID1

Compared to this substantial discrepancy, the differences between the WRF forecasts are much smaller. At a closer look, there are small differences in valleys, e.g. the Inn valley or in some valleys in Carinthia in Austria. Surprisingly, there are small discrepancies in areas where the influence of the topography should be negligible, for example over the sea. The precipitation fields in the western Mediterranean Sea show differences, even if one compares the bottom panels in Fig. 6.4 where the only difference is the nested domain over the Alps. Nothing in the domain outside the nested domain was changed, even all

model physics schemes remained the same in the parent domain.

The domain mean of precipitation is 8.49 mm for HYBRID16 (Fig. 6.4 top right) and decreases with high resolution topographies. 8.14 mm is the average precipitation for HYBRID4 (Fig. 6.4 bottom left) and 8.08 mm the average precipitation for HYBRID1 (Fig. 6.4 bottom right). Most striking is the difference to the ECMWF global model (Fig. 6.3) where the averaged precipitation for the domain used is 9.48 mm, which is roughly 15 % more than in the WRF forecasts. The precipitation is much more widespread in ECMWF but the hot spots are less pronounced.

As mentioned above, the low-pressure system has two cores but the western core strengthens during the first day. This is also shown in the cyclone tracks in Fig. 6.5. It should be mentioned that aside from the observations (VERA), the track is computed with the 850 hPa geopotential minimum instead of the MSLP minimum to avoid strong disturbances. The MSLP would be highly influenced by topography. The observation by VERA is computed out of weather stations and therefore, the track is computed using the MSLP. Nearly all four model runs as well as ECMWF locate the main pressure minimum over Corsica in the beginning. A few hours later, all four models and the ECMWF run show the pressure minimum over the Balearic Islands, which then moves eastward.

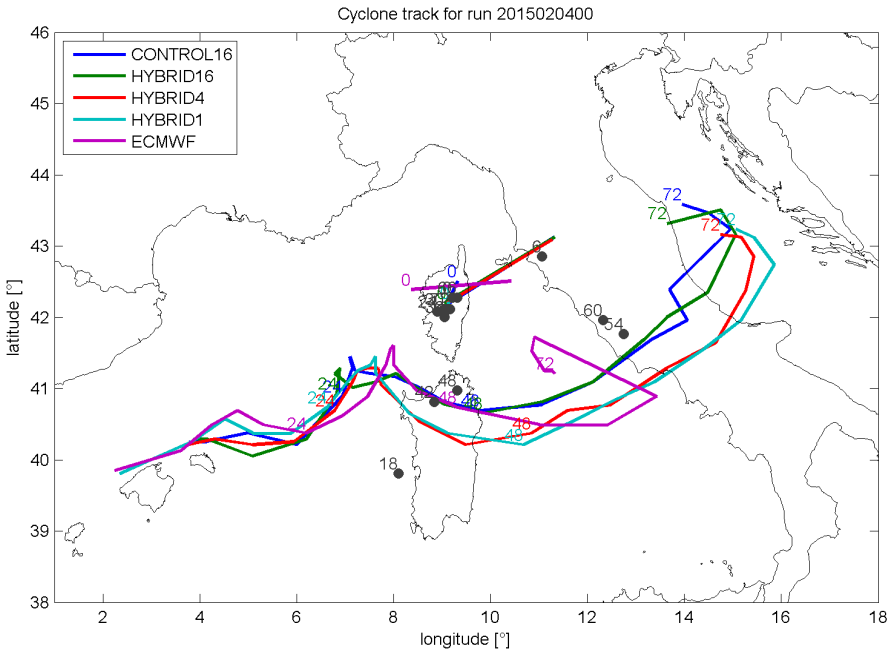

Figure 6.5: Cyclone tracks for all four different WRF runs, the global model ECMWF (see legend) and the verification with VERA, denoted by dark gray dots. The time ranges from 2015-02-04 at 0 UTC until 2015-02-07 at 0 UTC (72 h). The cyclone path is the minimum of geopotential height in 850 hPa. VERA dots are the pressure minimum of the mean sea level pressure (MSLP) and are shown every 6 hours. The numbers indicate the corresponding forecast hour since the initialization on 2015-02-04 at 0 UTC. All fields have been smoothed before the minimum was searched.

Overall, the difference between the pressure (CONTROL16) and the hybrid initial-

ization (HYBRID16) is very little. The higher resolution topographies (HYBRID4 and HYBRID1) in turn show a more southern and eastern cyclone track, but are - for their part - quite similar again. The ECMWF model has a completely different cyclone track especially after 48 hours as the path does not cross Italy while all others do. It is hard to tell which model run has the most accurate forecast, as the observed VERA pressure minima are very scattered due to a lack of weather stations in the Mediterranean.

Most of the precipitation in Austria falls between 24 and 60 hours after initialization. In all WRF runs, the precipitation is located further north than in ECMWF. This corresponds to the air pressure distribution: Fig. 6.6 shows that the modeled isobaric lines are shifted to the north. To allow a comparison, the ECMWF isobaric lines are also shown: It seems that ECMWF is slightly more accurate, e.g. over the western Alps. Furthermore, the pressure system's core pressure is too low in the WRF model. The three other model configurations not shown in the figure show a similar or even stronger shifting to the north.

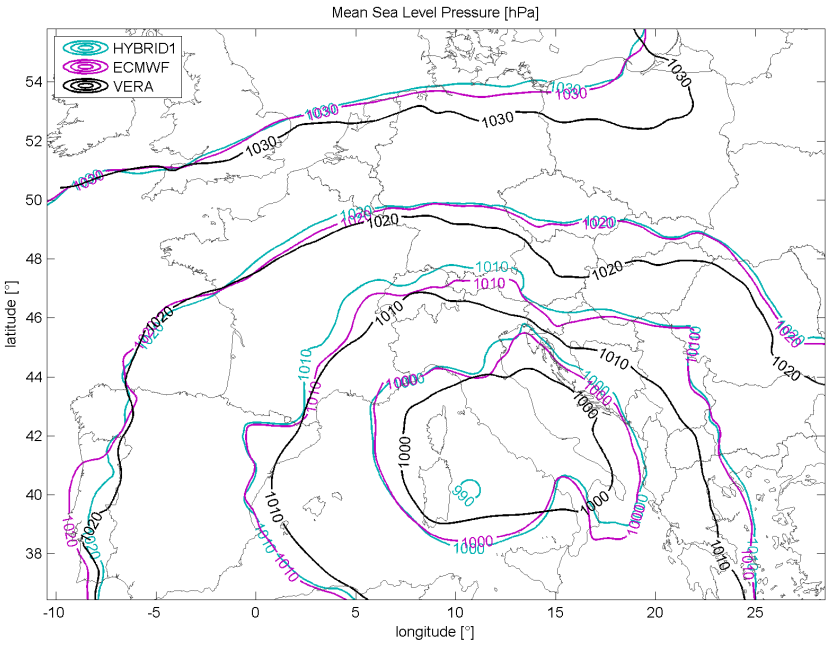

Figure 6.6: MSLP for 2015-02-06 at 0 UTC in hPa, that is a 48 h forecast. The cyan line represents the smoothed WRF model with nesting (HYBRID1), the purple one the ECMWF model and the black one is the observation (VERA).

The error of geostrophic height averaged over many levels is largest near the Alps (Radio soundings verification in Fig. 6.7) where the gradient of pressure is the strongest (Fig. 6.6 or Fig. 6.2). This is shown by dots in reddish color, which applies to Genoa, Milano, Udine or Zagreb. However, the higher resolution runs (HYBRID4 and HYBRID1 in bottom panels) feature a considerably smaller error in this area. This is due to the fact that the northward shifting is less pronounced than in the runs with ECMWF topography. The difference between the different initializations (CONTROL16 and HYBRID16) is negligibly small. Other parameters, such as temperature, dewpoint or wind, have similar

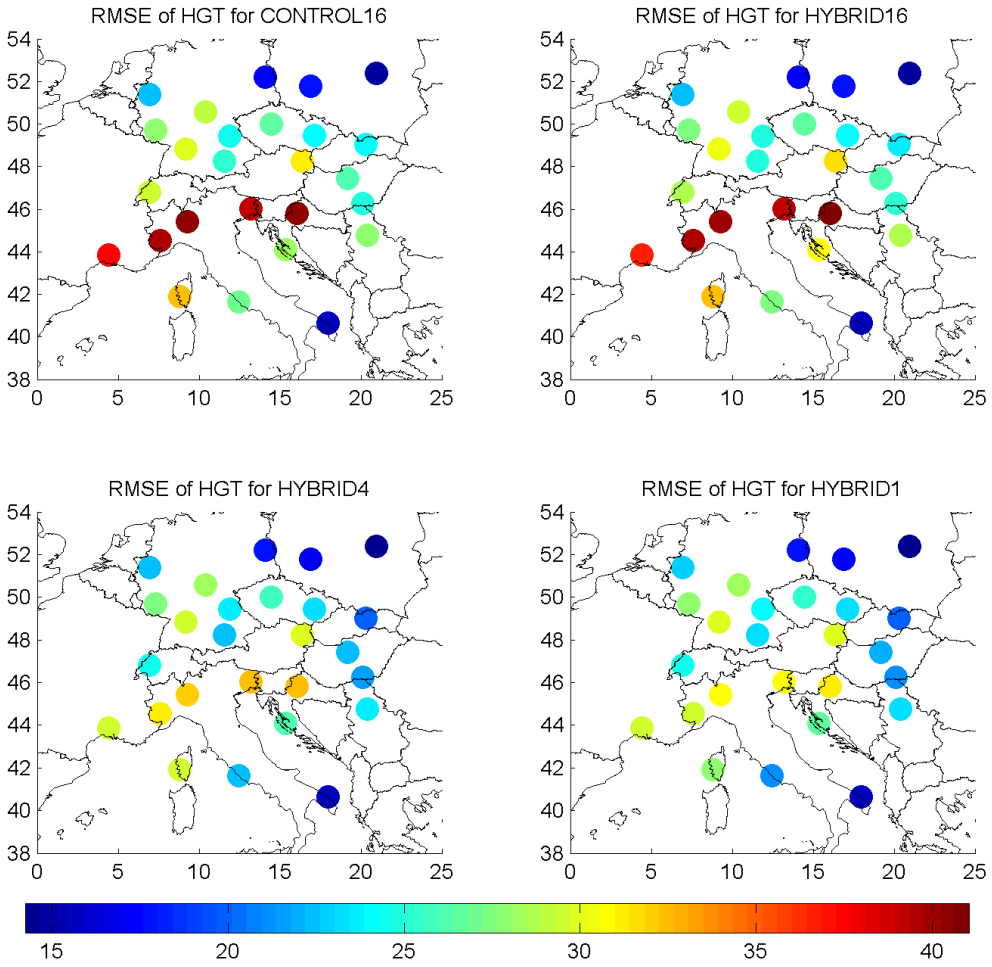

Figure 6.7: Mean RMSE of geostrophic height [m] in 16 isobaric levels (from 925 hPa to 200 hPa) and over 7 consecutive radio soundings (at 0 UTC and 12 UTC every day) in the forecast period of 72 h from 2015-02-04 to 2015-02-07 for all four WRF configurations (from top left to bottom right). Each dot represents one location where the WRF model was verified with radio soundings. The color denotes the magnitude of the error.

pattern (Figures not shown): Concerning all these parameters, the largest errors are located in the Alpine region and the higher resolution decreases the high errors near the Alps.

To show the differences between the four WRF configurations as well as the observation, a time series of the precipitation rate is shown in Fig. 6.8 for Vienna. This area is of particular interest for the author. The first two WRF configurations (CONTROL16 and HYBRID16) show very similar precipitation rates throughout the whole series. The configurations with high resolution topographies (HYBRID4 and HYBRID1) hold a lot less precipitation. However, the radar observation does not show any precipitation at all. Although ECMWF is not explicitly verified here, one can assume that ECMWF is not more defective than all WRF configurations by analyzing Fig. 6.3 and 6.4.

Fig. 6.9 shows the cumulative precipitation in comparison to the measured in-situ values

in Vienna. In addition, the ECMWF model is shown. As there was no precipitation at all, the ECMWF performs best since it has the least precipitation. Nevertheless, a more realistic topography seems to have a large influence on precipitation forecast quality in this case. This is also consistent with Fig. 6.4. The precipitation in all four WRF model runs is too far north whereas the ECMWF precipitation comparatively is further south.

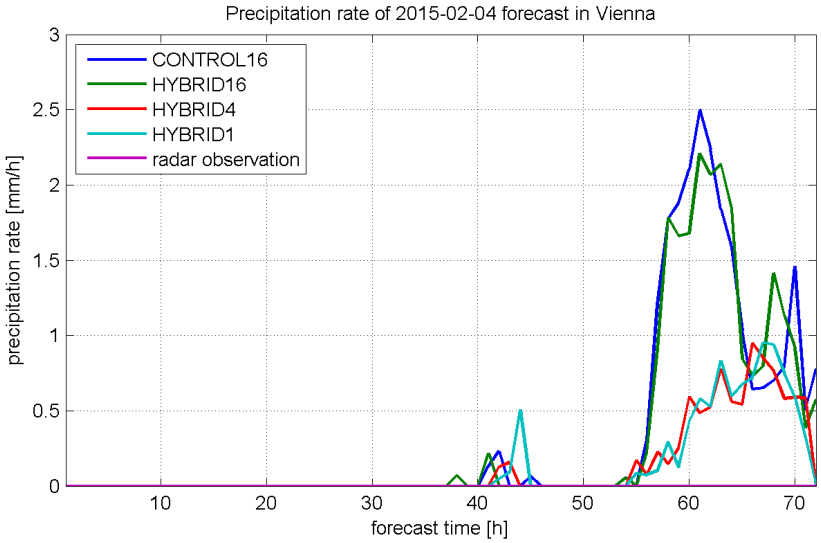

Figure 6.8: Precipitation rates in Vienna from 2015-02-04 0 UTC to 2015-02-07 0 UTC at every full hour. The radar reflectivity is the maximum radar reflectivity of CERAD for the entire atmosphere. The modeled reflectivity as well as the observed reflectivity is converted into the precipitation rate with Eq. 5.17. The purple line represents the radar observation.

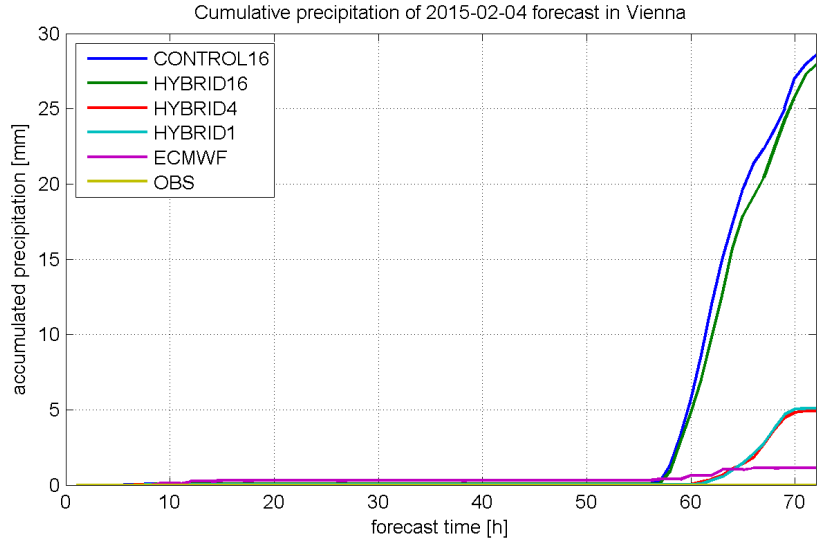

Figure 6.9: Cumulative precipitation in Vienna from 2015-02-04 0 UTC to 2015-02-07 0 UTC at every full hour. The observations (OBS) are hourly accumulated precipitation values of a weather station in Vienna, Hohe Warte (Station number 11035).

To verify the precipitation over the domain, the SAL method is used. Due to the lack of radar data for the whole domain, only a rectangular sector was taken where CERAD data is available. That is, roughly speaking, southern Germany, Austria and some parts of the Czech Republic, Slovakia and Hungary (see maps in Fig. 6.10).

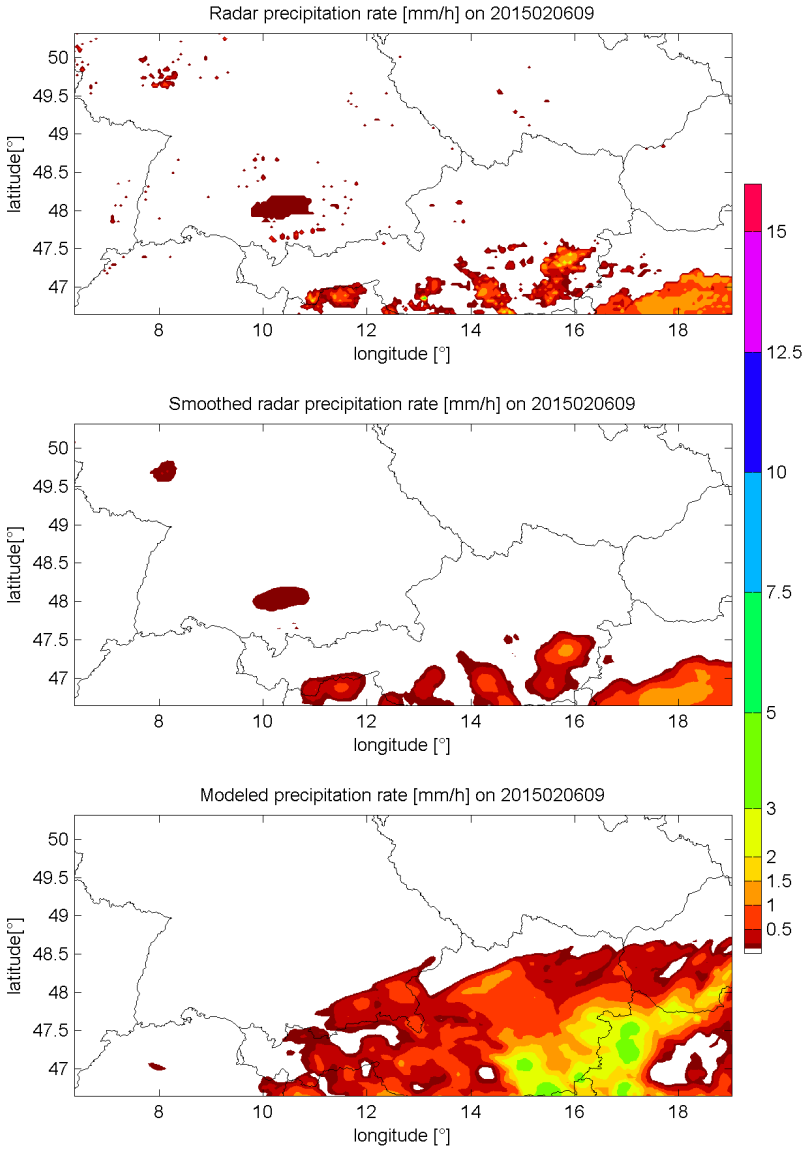

Figure 6.10: Precipitation rate for 2015-02-06 at 9 UTC. Upper figure: Precipitation rate converted from maximum radar reflectivity over the entire atmosphere. Middle figure: Smoothed precipitation rate from radar. Lower figure: Modeled precipitation rate from WRF (HYBRID1)

Since the Structure S and the Amplitude A can have negative values, a mean over many values would just refer to a bias, which is neither useful nor desirable in this case.

Therefore, absolute values have been used. For each full hour, all three components of SAL have been computed. Afterwards, a mean value over all 72 forecast hours delivers the wanted values. The radar data is very rough compared to WRF data (see Fig. 6.10 top). Therefore, no useful statement can be made without smoothing. This was achieved by a running arithmetic mean in a circular area around each gridpoint. By trail and error, a radius of 3 gridpoints was found to be suitable. The values for SAL for smoothed weather radar data are shown in Table 6.1. Still, the results are highly unsatisfying. It appears that HYBRID1 is even slightly worse than the others despite the high resolution topography. In this case - between 2015-02-04 and 2015-02-07 - there is hardly any precipitation in the first 48 hours (see also Fig. 6.8). Thus, it is beneficial to weight each value of SAL with the domain averaged precipitation value so that data with strong precipitation is higher weighted than data with only light precipitation. The weighting coefficient is a mean value of observed and modeled precipitation rate at each full hour. All weighting coefficients are normalized, so that the order of magnitude of SAL is maintained. Table 6.2 shows the final SAL values.

With weighting, a large improvement is observed with every step from CONTROL16 to HYBRID1 for all three parts of SAL. This also means, that hybrid initialization improves the precipitation forecast concerning structure, amplitude and location. The largest improvement is reached by changing the topography from the ECMWF topography to a 4 km topography. Overall, it can be stated, that in this case - where the forecasts are generally weak - all other WRF configurations at least do a better job than CONTROL16.

Table 6.1: Absolute values of Structure, Amplitude and Location for the period 2015-02-04 till 2015-02-07. Mean over all forecast hours without weighting. The observed radar data is smoothed.

	CONTROL16	HYBRID16	HYBRID4	HYBRID1
S	0.840	0.841	0.918	0.957
A	1.355	1.338	1.323	1.298
L	0.446	0.465	0.464	0.513

Table 6.2: Absolute values of Structure, Amplitude and Location for the period 2015-02-04 till 2015-02-07. Mean over all forecast hours, which were weighted with the domain averaged precipitation rate of both the radar observation and the modeled precipitation rate. The observed radar data is smoothed.

	CONTROL16	HYBRID16	HYBRID4	HYBRID1
S	1.438	1.264	0.950	0.887
A	1.857	1.700	1.209	1.078
L	0.498	0.464	0.362	0.354

6.2 7th Case: 2014-08-31 until 2014-09-03

This case stands out with large differences in many error measures between the model runs although the errors are not as big as in the 7th case. In contrast to the 7th case, this case took place in summer. Therefore, the pressure patterns are flatter than in winter. At the beginning at the analysis time step on 2014-08-31 at 0 UTC, there is a flat low in the 500 hPa level over the North sea and a weak upper level trough over the Benelux Union and eastern France (Fig. 6.11).

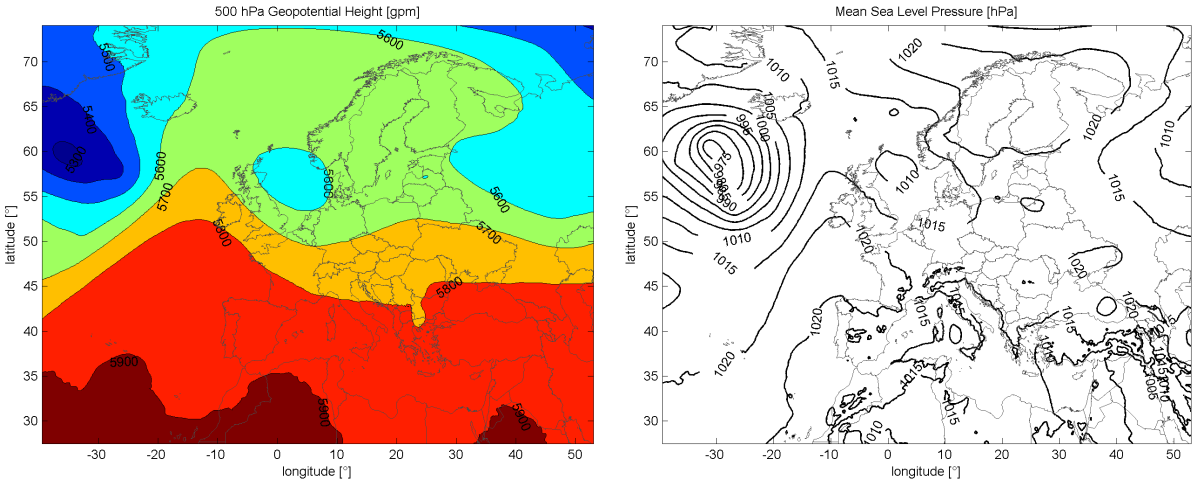

Figure 6.11: Synoptic weather conditions for 2014-08-31 0 UTC. The left panel shows the 500 hPa geopotential height in gpm, the right panel the mean sea level pressure in hPa. The data is from the analysis time step of the ECMWF run at 2014-08-31 0Z.

36 h after the initialization time step, a distinct Mediterranean low has developed. The development started in the Gulf of Genoa and the system moves southeastwards along the Adriatic Sea. A channel of low pressure also extends to the Northeast over Hungary which shows some characteristics of a Vb-low (Fig 6.12). In 500 hPa, a cut-off low develops at 12 UTC on 2014-09-01 that also moves southeastward during the next few hours.
As the pressure system shows a Vb-like pattern, the precipitation not only takes place in the surroundings of the Adriatic Sea but also elongated over Austria and the Czech Republic. Most of the precipitation in the Alpine Region happens between 24 and 72 hours after initialization.

Similar differences between the models and WRF configurations are observed, as shown in section 6.1. Although using the same topography (but not the same resolution), precipitation hot spots are much more pronounced in CONTROL16 and HYBRID16 (Fig. 6.14 top) than in the global model of ECMWF (Fig 6.13). Again, there is a northward shifting of precipitation fields compared to the global model, especially in the southern part of the domain. This is the most striking in countries like Bulgaria or Serbia. In contrast to the other case study, the ECMWF features less domain averaged precipitation (6.19 mm) compared to the averaged precipitation of WRF (between 7.39 mm and 7.72 mm).

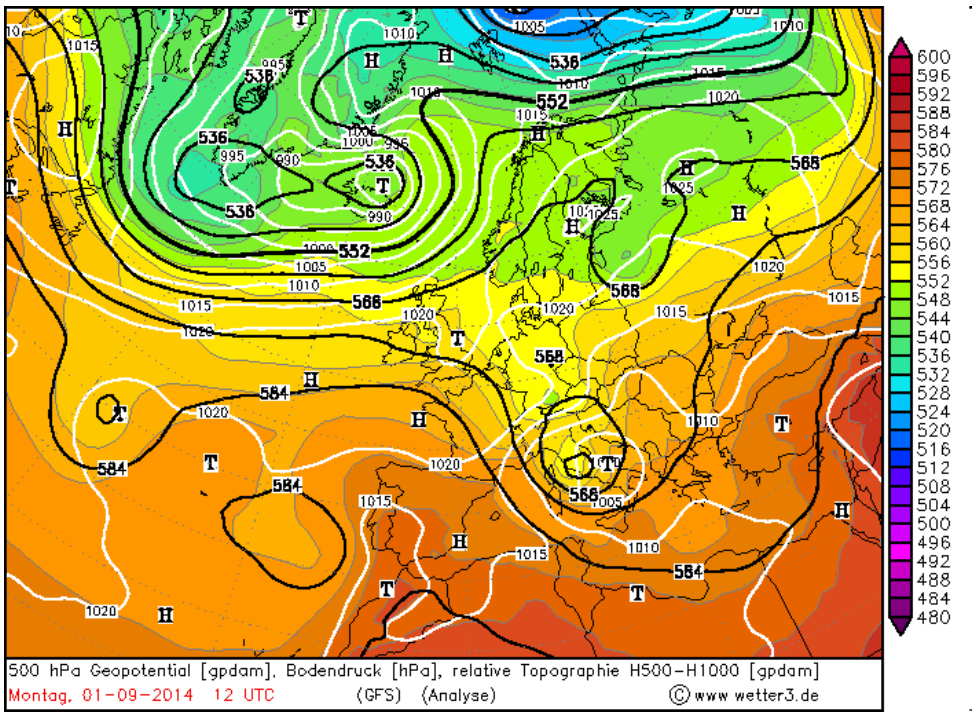

Figure 6.12: Synoptic weather conditions for 2014-09-01 12 UTC. The white lines indicate the mean sea level pressure in hPa. The black lines represent the relative topography which is the difference in gpdam of the 500 hPa and 1000 hPa level. The filled color fields show the 500 hPa geopotential height in gpdam. The data is from the analysis time step of the GFS run starting at 2014-09-01 12Z. Source: `http://www1.wetter3.de/Archiv/`

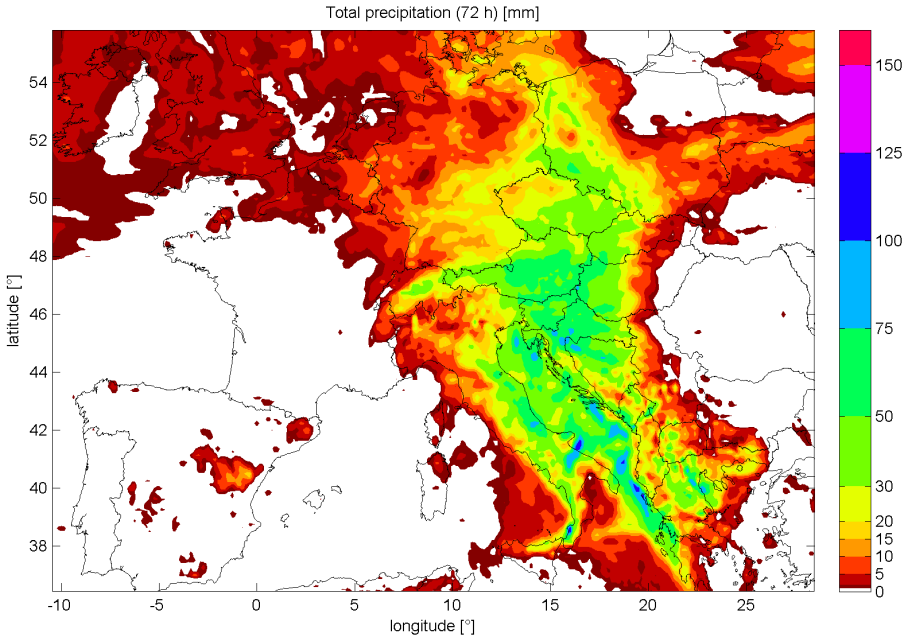

Figure 6.13: Total precipitation forecast of ECMWF from 2014-08-31 at 0 UTC until 2015-09-03 (72 hours) at 0 UTC. The initialization time is 2015-08-31 at 0 UTC.

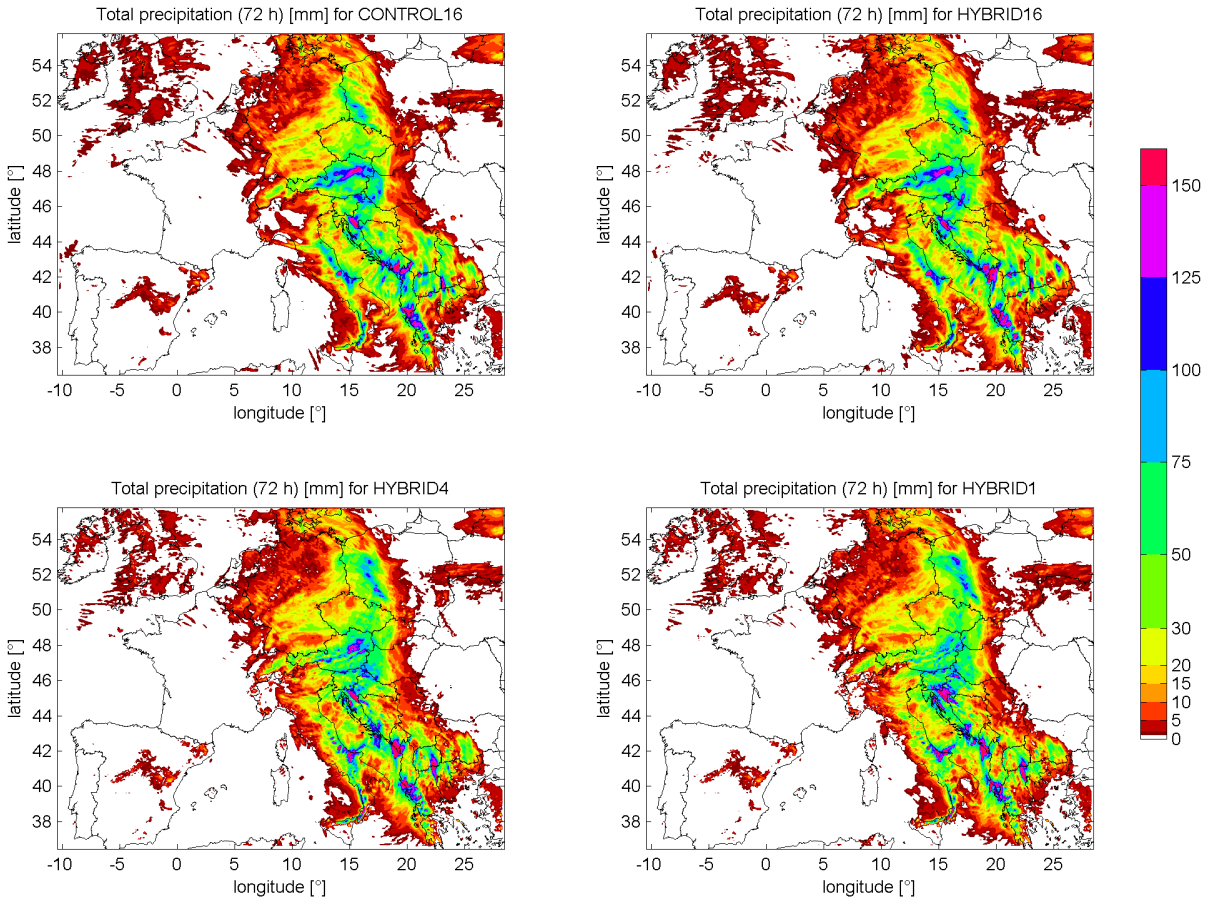

Figure 6.14: Total precipitation forecast of all four WRF runs from 2014-08-31 until 2014-09-03 (72 hours) at 0 UTC. The initialization time is always 2014-08-31 at 0 UTC. Top left: CONTROL16. Top right: HYBRID16. Bottom left: HYBRID4. Bottom right: HYBRID1

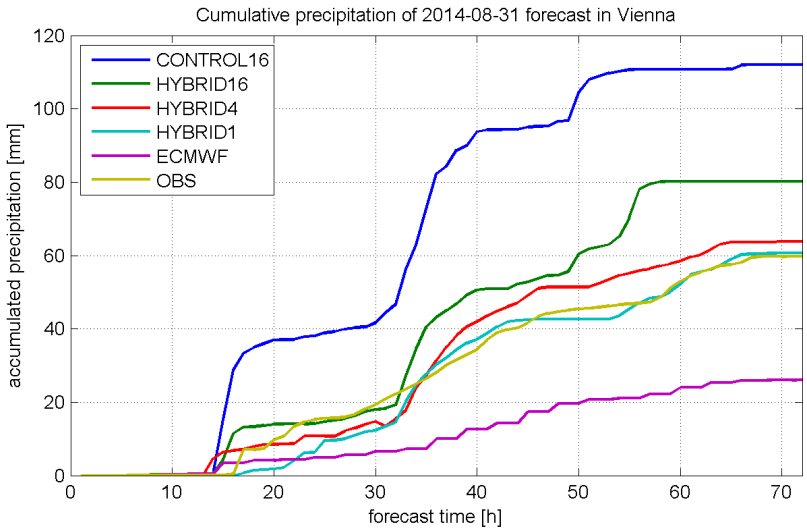

Figure 6.15: Cumulative precipitation in Vienna from 2014-08-31 0 UTC to 2014-09-03 0 UTC at every full hour. The observations (OBS) are hourly accumulated precipitation values of Vienna, Hohe Warte (Station number 11035).

The difference between the four WRF runs is less than expected as this is the case where the differences are largest of all 14 dates according to several error measurements. The WRF runs with more realistic topography tend to have more pronounced and slightly more widespread precipitation hot spots, as seen e.g. along the eastern Adriatic coast or in southwestern Poland. On the other hand, some valleys or basins feature less precipitation, maybe because of a too strong descending air on the Lee sides of mountain ridges. A more eye-catching difference is the slighter precipitation around the Ore Mountains in HYBRID4 and HYBRID1. Also quite striking is the reduced precipitation in HYBRID1 (bottom right) in eastern Austria.

Fig. 6.15 shows the cumulative precipitation in comparison to measured in-situ values in Vienna. In this case, HYBRID4 and HYBRID1 perform much better than ECMWF. In fact, HYBRID1 is extremely close to the observed precipitation on the ground.

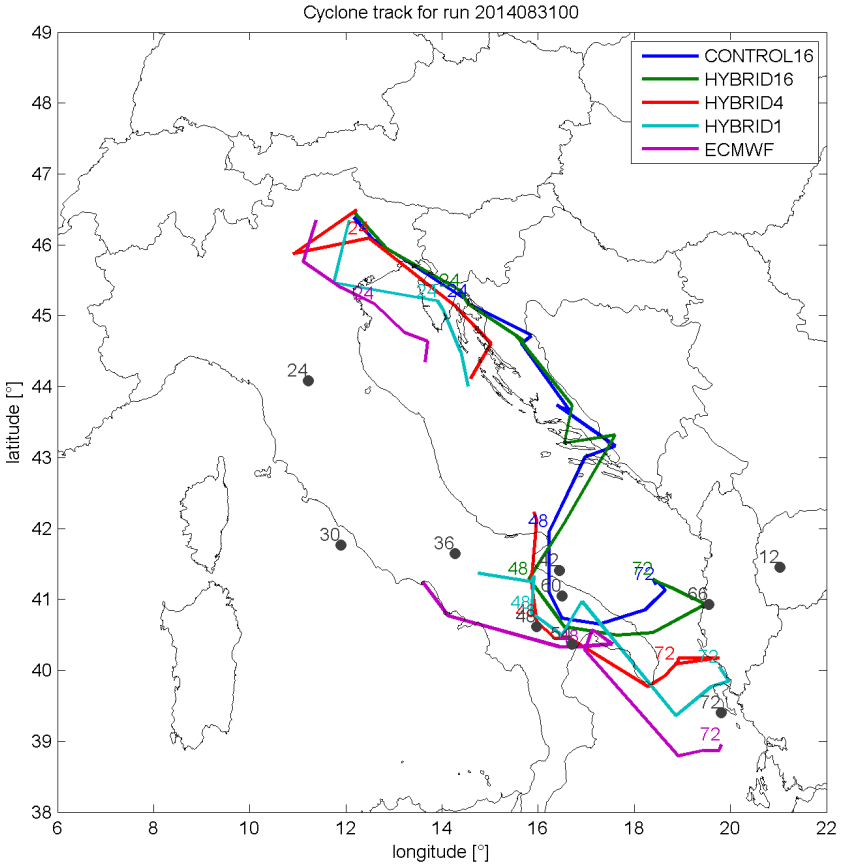

Figure 6.16: Cyclone tracks for all four different WRF runs, the global model ECMWF (see legend) and the verification with VERA, denoted by dark gray dots. The time ranges from 2014-08-31 at 0 UTC until 2014-09-03 at 0 UTC (72 h). The cyclone path is the minimum of geopotential height in 850 hPa. VERA dots are the pressure minimum of the mean sea level pressure and are shown every 6 hours. The numbers indicate the corresponding forecast hour since the initialization on 2014-08-31 at 0 UTC. All fields have been smoothed before the minimum was searched.

The cyclone tracking (Fig 6.16) shows a confusing pattern, although certain aspects are visible:

- There is no distinct pressure minimum in the first 24 h. The gray dots indicate the observation (VERA) and show a path over Italy and the southern Adriatic Sea. Yet it has to be said that only in situ weather stations on the ground are incorporated in this observation analysis, so that a pressure minimum over the ocean can not be observed.
- A northward shift of all models is present until forecast hour 48. However, this shift is less pronounced in HYBRID1.
- At the end at forecast hour 72, ECMWF and HYBRID1 are closest to the observed pressure minimum

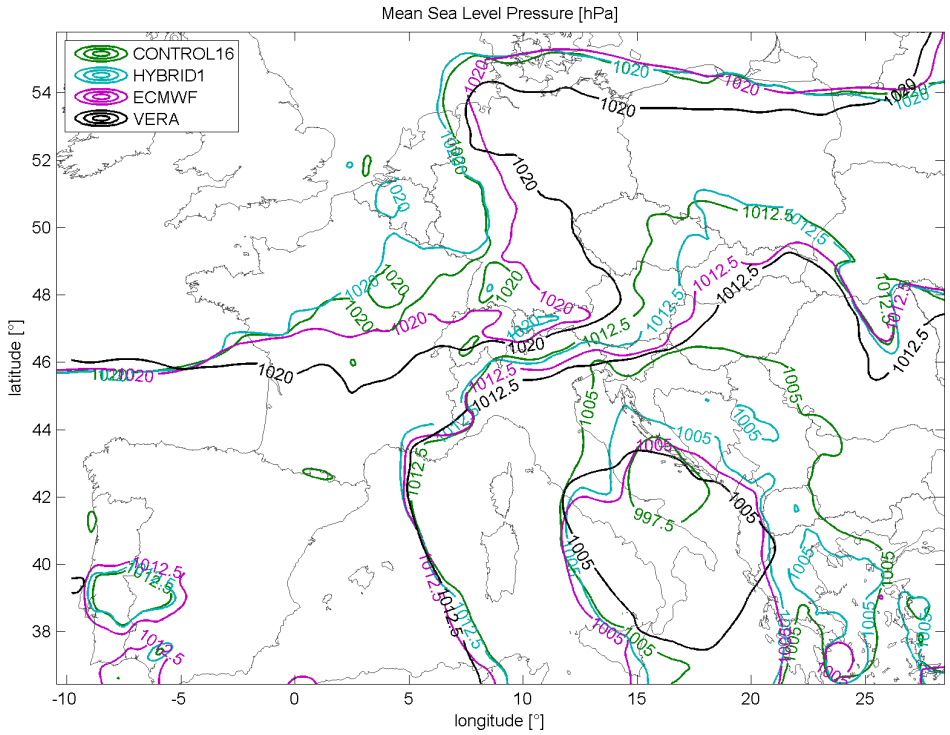

Figure 6.17: MSLP for 2014-09-02 at 0 UTC in hPa, that is a 48 h forecast. The black line represents the observation (VERA), the green one the WRF model with pressure initialization (CONTROL16), the cyan one the WRF model with nesting (HYBRID1) and the purple line represents the global ECMWF model. The isolines are shown in 7.5 hPa intervals.

In Fig. 6.17, the isobaric lines after 48 hours of forecast are shown. At this point of time, a pronounced Adriatic low has developed. The core pressures of the WRF runs are generally too low, especially in CONTROL16 (which is supposed to be the least accurate) where even the 997.5 hPa isoline exists. CONTROL16 is strongly shifted to the north. HYBRID1 (which is supposed to be the most accurate) has a much better forecast of

the 1005 hPa isoline. However, the isolines of ECMWF are mostly closer to the VERA analysis than all of the WRF runs.

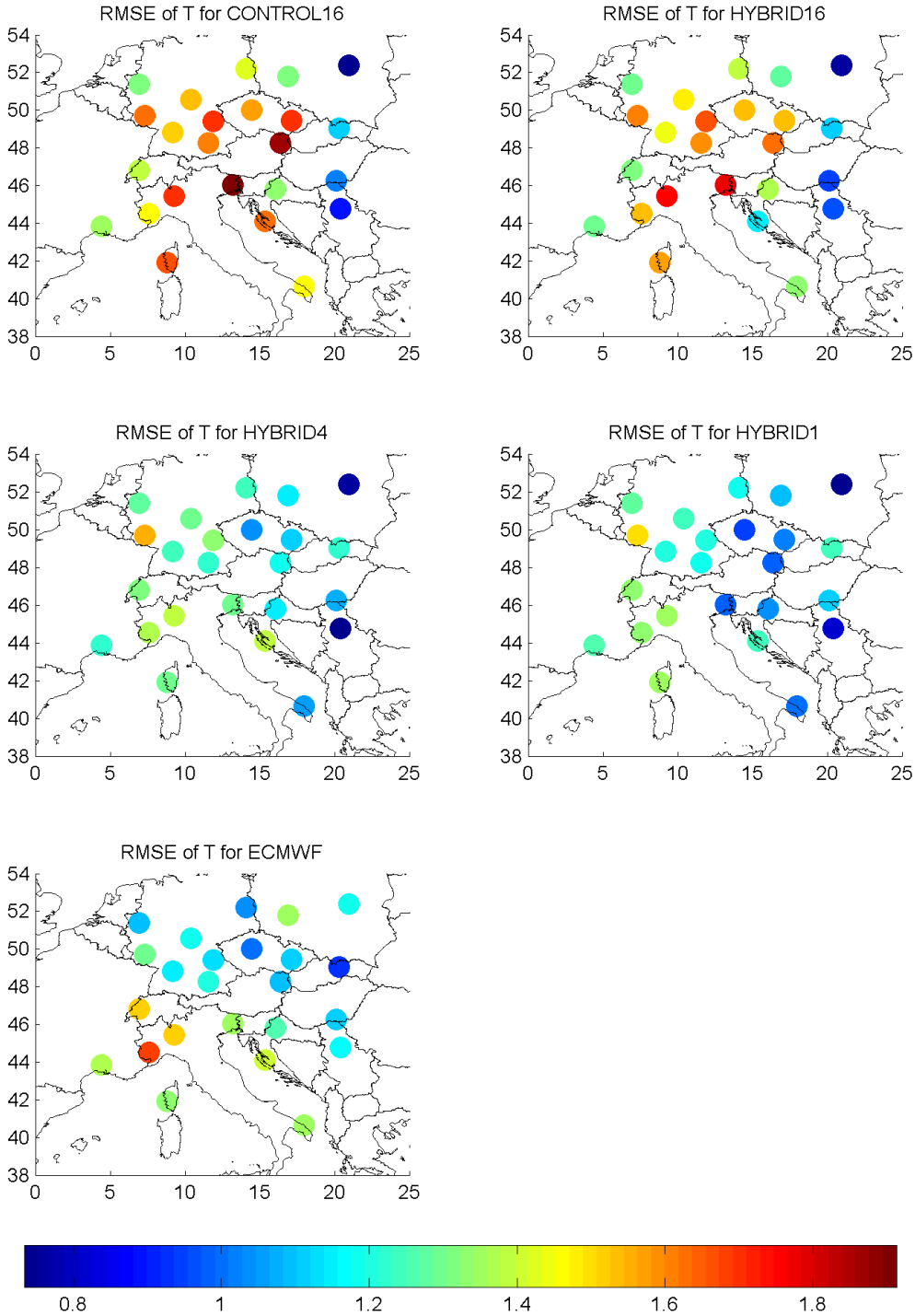

Figure 6.18: Mean RMSE of temperature [°C] in 16 isobaric levels (from 925 hPa to 200 hPa) and over 7 consecutive radio soundings (at 0 UTC and 12 UTC every day) in the forecast period of 72 h from 2014-08-31 to 2014-09-03 for all four WRF configurations and ECMWF (bottom left). Each dot represents one location where the WRF model was verified with radio soundings. The color denotes the magnitude of the error.

Fig. 6.18 shows the temperature RMSE, verified with radio soundings. Each configuration achieves further improvement in many locations, almost all stations in the greater Alpine region to be exact. The ECMWF forecast performs slightly worse than HYBRID4 and HYBRID1 but is still considerably better than CONTROL16 and HYBRID16.

Also other parameters, which are not shown here, show significant and widespread improvements in the WRF runs with high resolution topography, especially the RMSE of wind speed and geostrophic height. This is mostly caused by a more accurate pressure forecast in the Balkans.

The absolute, weighted values of SAL (Table 6.3) show a large improvement for the amplitude and location component. Surprisingly enough, the structure component has the smallest error in the HYBRID16 run. Obviously, the difference between hybrid level and pressure level initialization is considerably larger than in most other cases, where there is hardly any difference between CONTROL16 and HYBRID16.

Table 6.3: Absolute values of Structure, Amplitude and Location for the period 2014-08-31 till 2014-09-03. Shown are the mean over all forecast hours, which were weighted with the domain averaged precipitation rate of both the radar observation and the modeled precipitation rate. The observed radar data is smoothed.

	CONTROL16	HYBRID16	HYBRID4	HYBRID1
S	0.453	0.396	0.430	0.432
A	0.474	0.406	0.384	0.363
L	0.129	0.110	0.090	0.096

6.3 Other Cases

All other 12 cases are shorty described below. The figures for the synoptic weather conditions and the precipitation totals are in the appendix at the very end of this thesis:

1th Case: 2013-09-15 until 2013-09-18: A weak low in the MSLP elongates from the Adriatic Sea to Poland. The core low develops in the Gulf of Genoa and moves northeastward. High precipitation amounts are found almost everywhere in the Eastern Alps.

2th Case: 2014-01-19 until 2014-01-22: A strong MSLP low develops west of the Italian Peninsula. Strong precipitation is found especially in the Southern Alps.

3th Case: 2014-03-22 until 2014-03-25: A low pressure belt is located from the Gulf of Genoa to Poland. Large amounts of precipitation are found all over the Alps.

4th Case: 2014-05-14 until 2014-05-17: A MSLP low over eastern Hungary makes this case one of the Vb-like cases. Therefore, the heaviest precipitation areas are located in the northern parts of the Eastern Alps.

5th Case: 2014-07-20 until 2014-07-23: A weak MSLP low develops over the Gulf of Genoa with a secondary low over the Czech Republic and Hungary. The precipitation hot spots are located in the Western Alps.

6th Case: 2014-07-28 until 2014-07-31: A MSLP low moves slowly from northern Italy to Hungary which shows Vb-like patterns. Strong rain events cause floodings in parts of Austria.

8th Case: 2014-09-10 until 2014-09-13: Most of the precipitation is concentrated over the Eastern Alps and southward along the east Adriatic coast. This is one of the Vb cases, as the pressure low moves northeastward from the Adriatic Sea towards Hungary.

9th Case: 2014-09-12 until 2014-09-15: Similar synoptic conditions as shown above.

10th Case: 2014-11-04 until 2014-11-07: A MSLP low over Corsica and Sardinia is linked to strong precipitation in the Southern Alps.

11th Case: 2015-01-23 until 2015-01-26: A distinct large low pressure system is located over the Mediterranean Sea with a secondary low developing over Eastern Europe. Therefore, this is one of the Vb-like cases.

12th Case: 2015-01-29 until 2015-02-01: A Vb low can be found as a secondary low of a large low pressure system in the Mediterranean Sea. However, most of the precipitation falls east of the Alps.

14th Case: 2015-02-23 until 2015-02-26: This case is a Genoa cyclogenesis that develops Vb like patterns, as it moves northeastward. The precipitation hot spot is in eastern Austria and western Hungary.

7 Results

7.1 Verification with Radio Soundings

Since reliable observations of the upper atmosphere are rare, radio soundings are one of the few upper air observations and thus, used in this work.

7.1.1 Pressure vs. hybrid Initialization (CONTROL16 and HYBRID16)

Fig. 7.1 compares CONTROL16 with HYBRID16. The left illustration shows that the RMSE of temperature slowly decreases with height. Above 350 hPa, there is a fast increase in RMSE which is due to a positive bias above this level (right illustration). This bias is not necessarily a model bias. One possible reason for this error could also be the measurement error of radio soundings. Since the upper measurements may be above the troposphere, the radiosonde itself could have a cold bias due to the inertia of measurement. As it reaches warmer areas above the tropopause, the inertia would cause the model to have a warm bias.
The comparison of the two initializations shows that there is very little difference between pressure and hybrid level initialization. In the overall mean, there is a negligible improvement in upper levels where the 137 ECMWF hybrid levels deliver much more information.

However, at forecast hour 0 (analysis time step), there is a significant improvement (Fig. 7.2). In those levels where there is no information with the initialization on pressure levels, the hybrid level initialization (HYBRID16) has smaller errors. In particular, these are the pressure levels 750, 650, 550, 450 and 350 hPa. Furthermore, the bias is smaller at almost all levels. The mean RMSE of temperature is reduced from 0.70 to 0.65.
Similar patterns are observed with other parameters, like dewpoint or geostrophic height (Figures not shown). This improvement is still present for the forecast hour 12. However, longer-range forecasts (more than 24 h) just show very little improvement with initialization on hybrid levels. That is why the overall mean does not show any significant change in error measurements.

7.1.2 Topography: HYBRID16, HYBRID4 and HYBRID1

To fully account for the nested domain, this section only treats the eight radio soundings within the nested domain. Since the difference between the two different initializa-

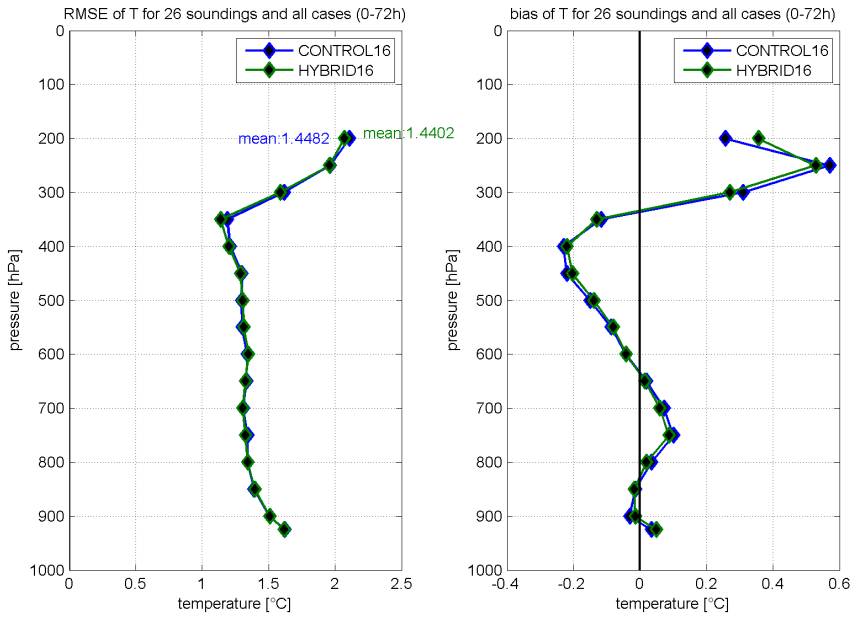

Figure 7.1: Verification of temperature with data from radio soundings for the two different initializations (CONTROL16 and HYBRID16) averaged over all forecast hours. The left illustration shows the RMSE of temperature and the right the bias of temperature. A negative bias corresponds to a cold model bias. The values are averaged over all 26 soundings (Table 5.2), all 14 dates (Table 5.1) and all 72 forecast hours (7 soundings per location).

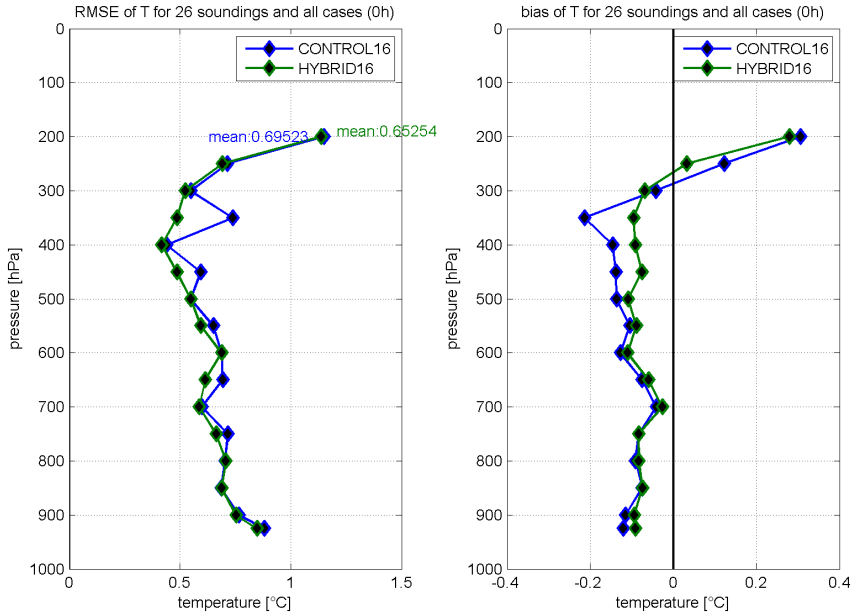

Figure 7.2: As in Fig. 7.1, but only for the analysis time step (0 h).

tions is small, only the influence of resolution and topography is discussed in this section (HYBRID16, HYBRID4 and HYBRID1).

The change from the coarse ECMWF topography to the 4 km topography achieves a big improvement over all pressure levels (Fig. 7.3). These improvements grow gradually with forecast time. There is no improvement at the analysis time step but significant improvement after 24 hours or more (No Fig. shown). However, it goes along with a positive bias of temperature in lower levels. This could be explained by descending air or Foehn-like effects, since all eight locations lie near the Alps. A more realistic topography features deeper valleys and higher mountains which could favor such conditions. Above 700 hPa, both bias and RMSE are improved with better topographies.
Although the forecast of ECMWF features a distinct negative temperature bias over almost all pressure levels, the RMSE is lower compared to all WRF configurations at lower levels. However, the RMSE is larger in the mid-troposphere between 550 hPa and 350 hPa where the WRF runs perform better.

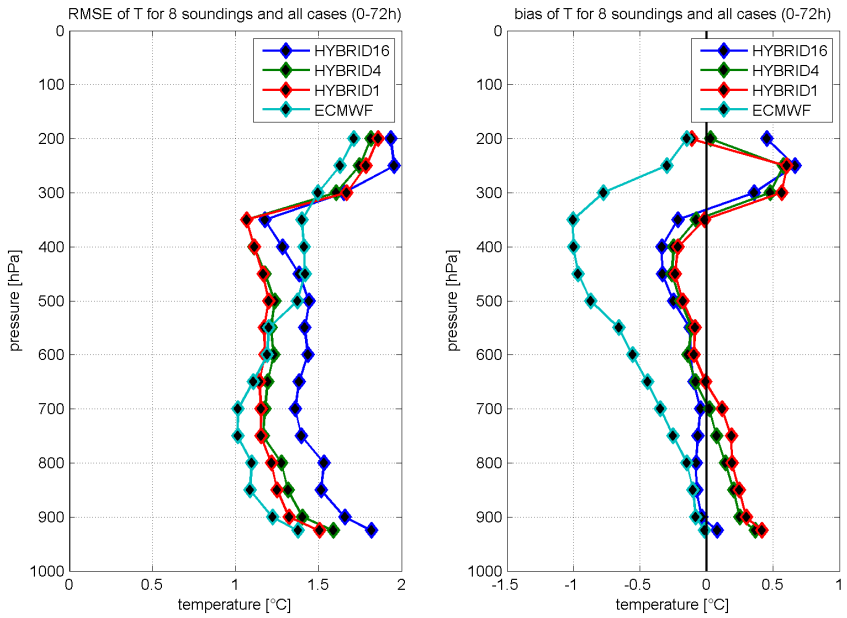

Figure 7.3: Verification of temperature with data from radio soundings for HYBRID16, HYBRID4, HYBRID1 and ECMWF. The left illustration shows the RMSE of temperature and the right the bias of temperature. Only radio soundings from inside the nested domain are used. The values are averaged over the 8 soundings that lie within the nested domain (Bold locations in Table 5.2) and all 14 dates (Table 5.1) and all 72 forecast hours (7 soundings per location).

The nested domain shows some signs of improvement concerning RMSE, especially in lower and mid-troposphere. In upper levels, the influence of the comparatively small nested domain vanishes. Again, the positive bias increases even more with the nested domain, which supports the theory of Foehn-like effects that warm the air in lower layers as the air descends. Overall, the 4 km topography features significant improvements concerning the temperature forecast, whereas the nested domain reduces the RMSE of

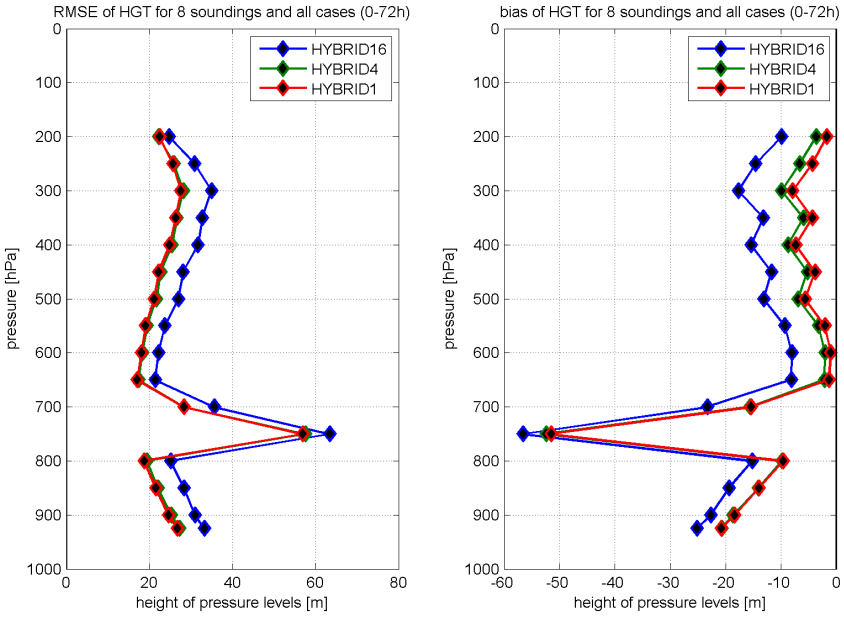

Figure 7.4: As in Fig. 7.3, but for the geometric height of isobaric levels in meters. ECMWF height data on pressure levels is not available.

temperature only slightly more.

In Fig. 7.4, the verification for the height of pressure levels is shown. First of all, it must be said that the peak in 750 hPa can not be explained. If this peak is caused by a bug in the programs, this bug could not be found. If, on the other hand, this is not a mistake but a signal for large errors in the model, no comprehensible explanation could be found.

Even more pronounced than in the temperature verification, there is an overall improvement of the height of pressure levels with the use of a more realistic topography (HYBRID4) in both RMSE and bias. The nested topography, in contrast, just shows some slight improvements in some levels, e.g. the bias is reduced in upper tropospheric levels. Surprisingly, all configurations show a negative bias of geostrophic height. After all, this negative bias can be reduced by higher resolution topographies. In other words: The modeled pressure is too low on average or lows are too deep, especially near surface since the bias is largest below 900 hPa (except for the unexplained peak in 750 hPa). This is also consistent with the case studies in chapter 6, where the core pressures were too low. The two case studies also indicate, that the pressure or geopotential bias is not evenly distributed. This would raise the pressure gradients and thus, have important impacts on weather. The RMSE and bias of geometrical height grow gradually with forecast time. However, there already is a bias of approx. 13 m at the analysis time step (Fig. 7.5). It appears that an error of the height of pressure levels that is already present in the analysis, evolves through time and grows.

As last parameter, the wind speed is verified. Fig. 7.6 shows a rather constant RMSE of wind speed with height, although there is a peak near the tropopause. This is not

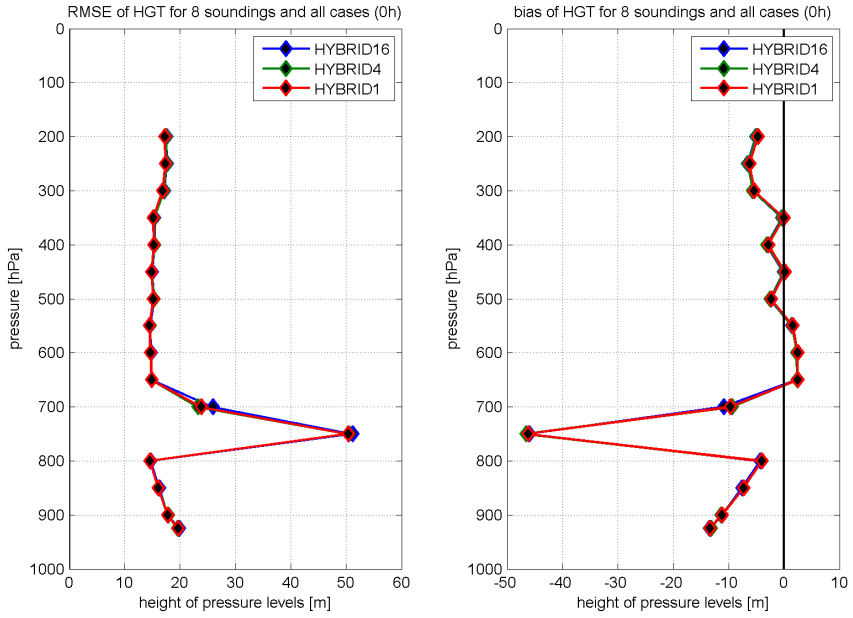

Figure 7.5: As in Fig. 7.4, but for the first time step only (analysis time step).

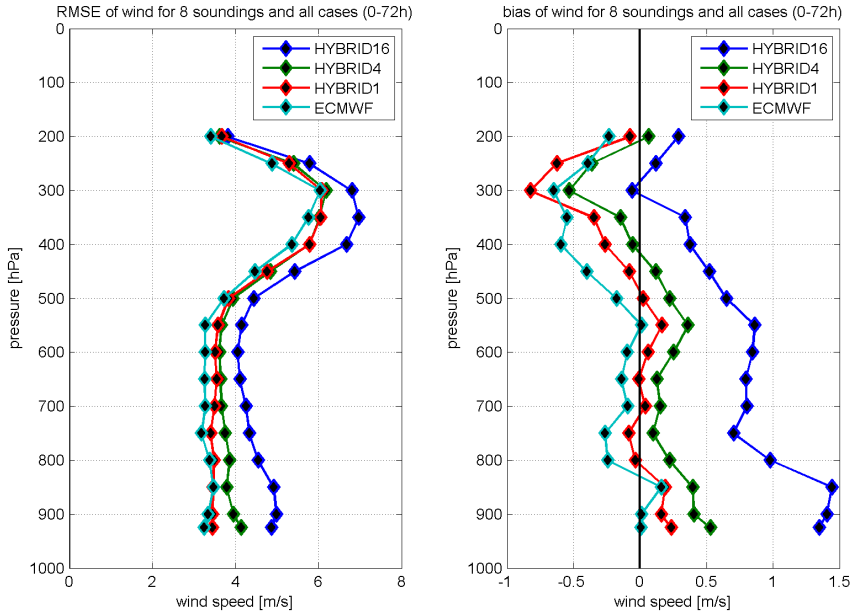

Figure 7.6: As in Fig. 7.3, but for wind speeds in meters per second.

surprising since one assumes stronger wind speeds in this height which causes larger absolute errors. It is more striking that there is a positive bias of wind speed below 450 hPa in almost all configurations. This is consistent with the assumption of too strong pressure gradients which cause stronger winds. In particular, HYBRID16 features winds that are too strong. HYBRID4 still suffers from a positive bias. Only HYBRID1 has a bias that evens out close to zero. This could be explained with the influence of topography

on friction and roughness lengths. Rougher topography lowers the roughness length and enables lower wind speeds. However, the ECMWF model still performs at least as good as the best WRF configuration (HYBRID1) or even better.

All in all, using a more realistic topography with 4 km resolution improves temperature, wind speed, geostrophic height and also dewpoint forecasts (no Fig. shown). Further significant improvement can be achieved by the nested domain, particularly concerning wind speed. However, this improvement comes with approximately three times the computational costs.

Other figures of parameters not shown in this section are in the appendix at the very end of this thesis.

7.2 Verification of Precipitation with Weather Radar Data

Radar data is used to verify the model by applying the SAL method (Wernli et al., 2008). As already stated in Section 6.1, the radar data was smoothed to achieve a similar shape compared to WRF precipitation fields. It is said once again that the verification is only valid for a small part of the domain, which is shown in Fig 6.10. There was no radar data available in the year 2013. This is why the first case in 2013 is not included in the results.

The structure component S (see Fig. 7.7 top) is strongly dependent on the strength of the smoothing. The best smoothing was found by trial and error. Although it is not easy to draw any conclusions, because the lines are very close to each other, the cyan line (HYBRID1) is mostly closest to $S = 0$. The amplitude component A shows that the first forecast hours are of no use because it takes some time for the model to allow precipitation to form. However, there seems to be a negative bias (too little precipitation) in the first 20 hours, whereas after 30 hours, all model configurations feature a positive precipitation bias. At the end of the forecast period, the amplitude component gets slightly negative again. Overall, HYBRID1 tends to have the least precipitation of all four configurations. The location component L shows a slight increase over time. This is not surprising since models errors usually grow with time and the location component can only have positive values. There is no clear difference between the four different WRF model configurations.

To clearly arrange the SAL results, it was tried to average the SAL values but this is not trivial. First of all, it does not make any sense to average the SAL values because the result would be some kind of bias. Therefore, the SAL values are squared, added together and finally, the square root is taken. Since this is some kind of RMSE, these values are called RMSE of SAL. As a mean of SAL values treats all values equally, a weighted mean was also regarded as helpful. If there is only very little precipitation, the SAL values are not as important compared to time steps with very heavy precipitation. Therefore, the values are weighted with the domain mean precipitation of both model and observation.

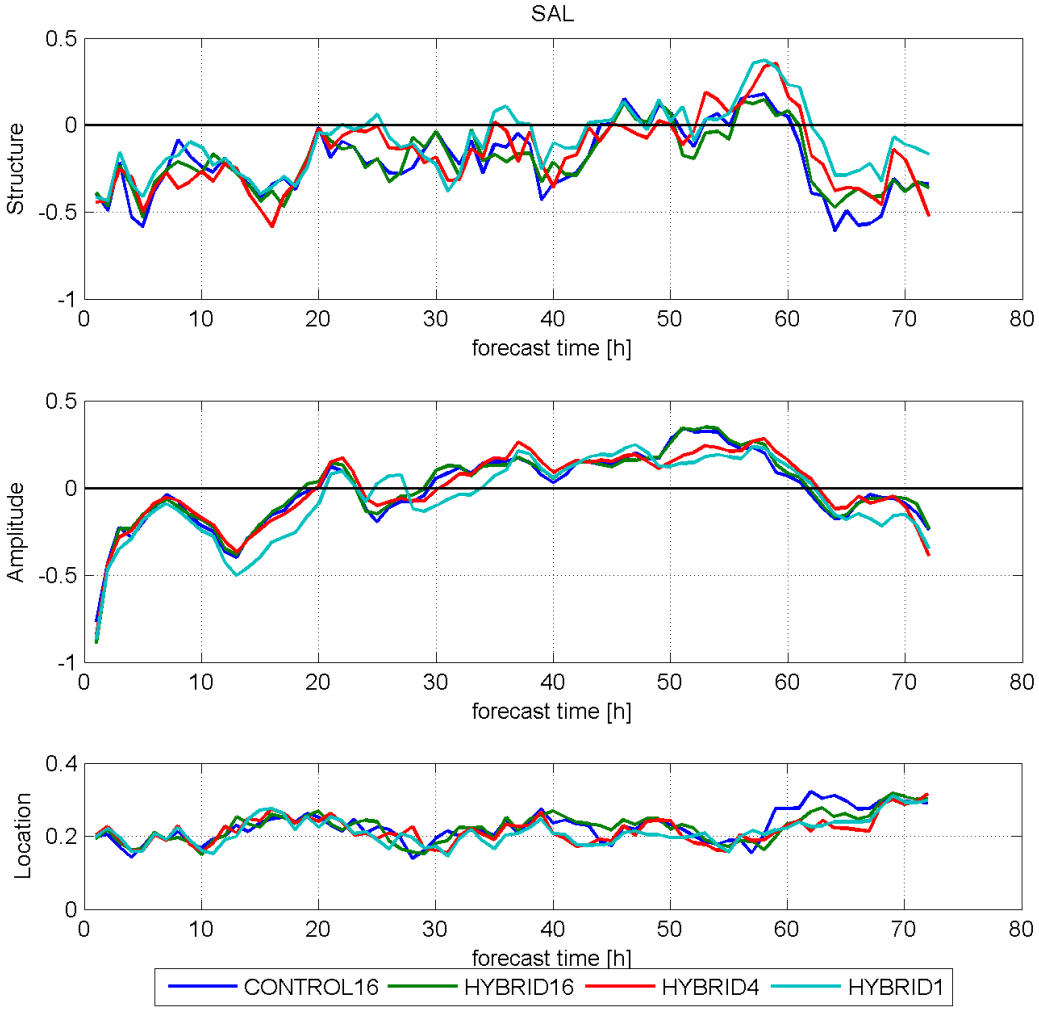

Figure 7.7: SAL against forecast time for 13 cases (year 2013 not included). Top: Structure component S. Center: Amplitude component A. Bottom: Location component L

7.2.1 Mean SAL Values without Weighting

Just to show that smoothing of radar data is absolutely necessary, Table 7.1 shows the RMSE of SAL for unsmoothed data. In this table one would assume that the structure components gets even worse with more realistic configurations. Table 7.2 shows the RMSE values for SAL with smoothed weather radar data. There is not much difference between the first two configurations. Only the amplitude component tends to have slightly improved. A large improvement is achieved by HYBRID4 for all three SAL components. The nested domain shows some additional improvement, especially for the structure component.

Table 7.1: RMSE of Structure, Amplitude and Location. Mean over all forecast hours and all cases of 2014 and 2015. No smoothing of radar data at all. For the definition of the four WRF configurations, see Table 5.4.

	CONTROL16	HYBRID16	HYBRID4	HYBRID1
S	0.846	0.847	0.861	0.865
A	0.600	0.592	0.553	0.535
L	0.206	0.207	0.199	0.202

Table 7.2: As in table 7.1, but with smoothing of radar data.

	CONTROL16	HYBRID16	HYBRID4	HYBRID1
S	0.868	0.867	0.855	0.821
A	0.600	0.592	0.553	0.535
L	0.206	0.207	0.199	0.200

7.2.2 Mean weighted SAL Values

As soon as the SAL values are weighted with the domain averaged precipitation, the results slightly change (see Table 7.3). There is more difference between the two different initializations. Furthermore, HYBRID1 with the nested domain achieves improvements in all 3 SAL components. In contrast to above, the location component shows significant differences between the four WRF configurations.

Table 7.3: As in table 7.2, but the values are weighted with the domain averaged precipitation before averaging.

	CONTROL16	HYBRID16	HYBRID4	HYBRID1
S	0.785	0.779	0.771	0.720
A	0.734	0.722	0.696	0.665
L	0.275	0.273	0.261	0.256

7.3 Verification with VERA

This section treats the verification of 2 m specific humidity, 2 m temperature and MSLP. To include ECMWF in the verifications of specific humidity, a conversion from the ECMWF dewpoint temperature in 2 m into the 2 m specific humidity had to be made. Following equations were used for this matter (Alduchov, 1996):

$$e = 6.1094 \exp\left(\frac{17.625\,Td}{243.04 + Td}\right) \tag{7.1}$$

where e is the vapor pressure in hPa and Td the dewpoint temperature in degree Celsius. The final conversion to the needed specific humidity in kg/kg is given by (Bauer et al., 2001):

$$q = \frac{0.622e}{p - 0.377e} \tag{7.2}$$

where e is the vapor pressure in hPa from above and p the air pressure in hPa.

Fig. 7.8 shows averaged RMSE and bias values for all cases, excluding the first two cases because VERA data was only available since March 2014. First of all, the RMSE grows with time - in general. This is true for all three displayed meteorological parameters. The global model of ECMWF performs always better concerning the RMSE values. The WRF runs feature larger errors. However, there are some significant differences between the four WRF configurations: The top left panel shows the RMSE of 2 m temperature. There is a distinct diurnal cycle. Daytime temperatures feature a greater error than nighttime temperatures. This is clearly visible in all WRF configurations as well as in ECMWF. Again, as in many other verifications, the difference between the two initializations is marginal. A great improvement is achieved by the 4 km topography (HYBRID4). There is hardly any further improvement with the nested domain (HYBRID1), but is has to be said that this is a domain average of the whole domain covering most parts of Europe. Overall, there is a negative temperature bias (top right) which means that the forecasts are too cold, in particular during daytime.

Concerning MSLP (center panels), there is again little difference between the two initializations. There is a big improvement with HYBRID4 and the error gets even smaller with the nested domain. As already indicated in Fig. 7.4 and Fig. 7.5, there is a negative MSLP bias, which grows with forecast time. However, the WRF runs with high resolution topographies (HYBRID4 and HYBRID1) are able to reduce the bias. It appears that the ECMWF model performs better in both RMSE and bias.

When it comes to the RMSE of 2 m specific humidity, there is a distinct diurnal cycle that repeats twice a day. Obviously, the errors are largest at early morning time and in the afternoons. WRF configurations with more realistic topographies are able to reduce the error during daytime, whereas the errors during the early morning hours stay more or less unchanged. Compared to the other meteorological parameters, there is no striking bias although it features a diurnal cycle. Here, the ECMWF is actually the only model that has a clear overall negative humidity bias.

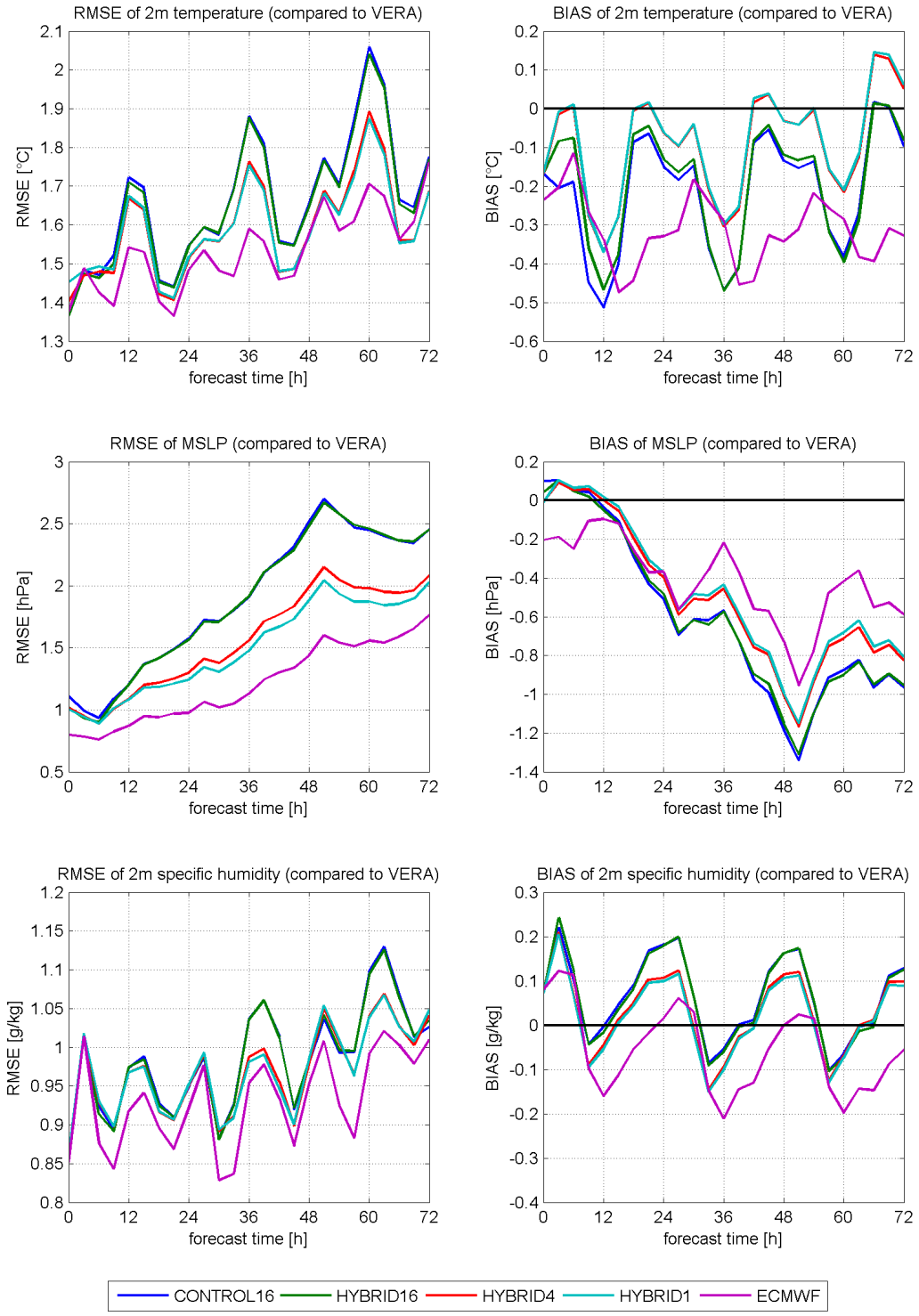

Figure 7.8: RMSE (left) and bias (right) verified with VERA against time. Averaged over 12 dates (first two not included) and all gridpoints within the domain. 6Upper illustrations represent the 2 m temperature, the illustrations in the middle the MSLP and the lower illustrations the 2 m specific humidity. The data is plotted every three hours.

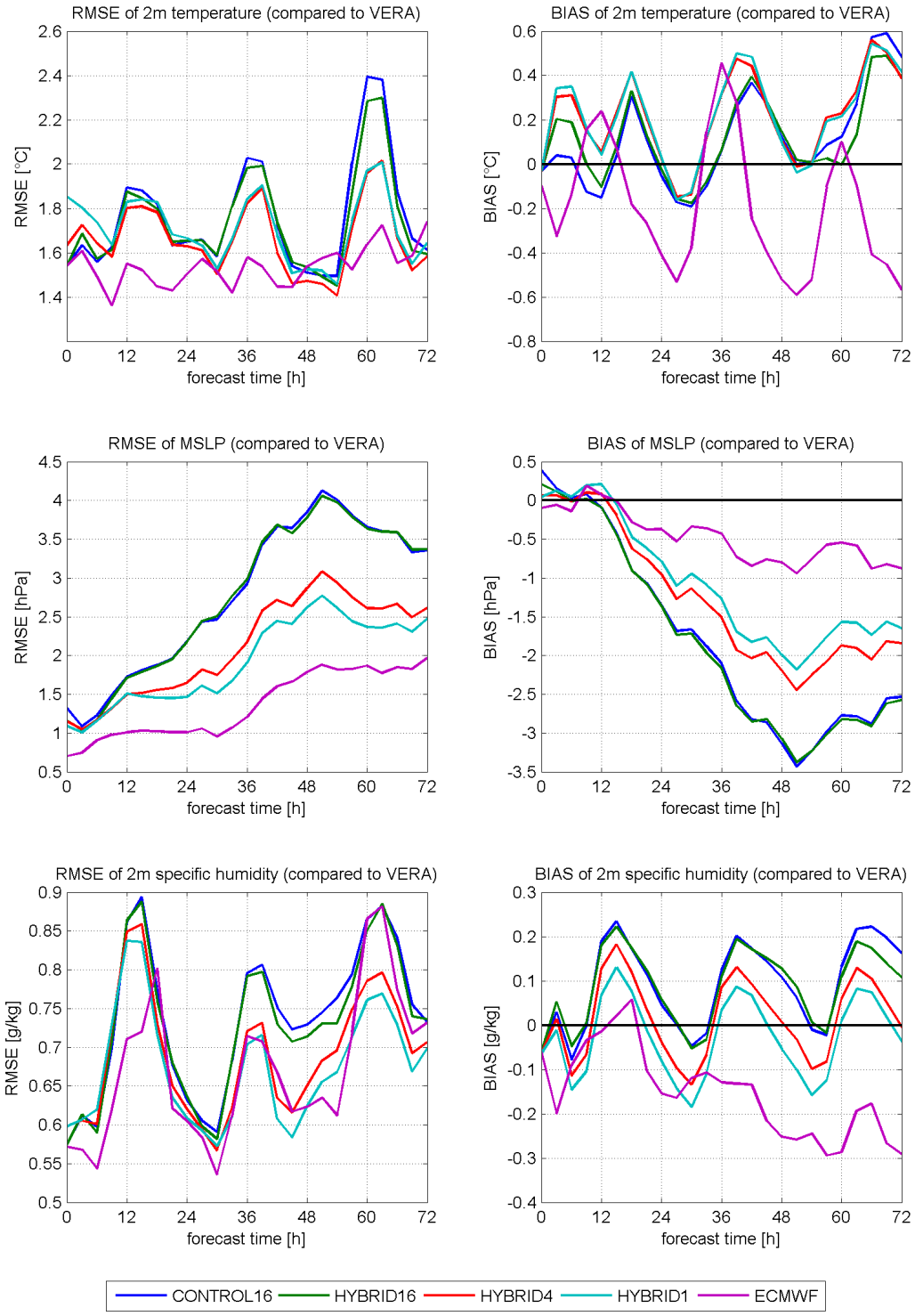

Figure 7.9: As in Fig. 7.8, but only for central Europe, as shown in the maps in Fig. 6.10

There are a few differences as soon as the verification is made in the area of particular interest, namely central Europe as shown in Fig. 7.9:

- The upper right panel shows a mostly positive 2 m temperature bias, whereas the bias over the whole domain is negative. This supports the idea that Foehn-like effects cause too high temperatures near the Alps (see also Fig. 7.1).
- The negative bias of MSLP (center right) is almost three times as large as over the whole domain. This indicates a far too low pressure in Central Europe during the presence of Mediterranean cyclones. Due to the limitation on Central Europe only, HYBRID1 with the nested domain in this region tends to achieve significant improvements compared to HYBRID4 (red vs. cyan line).
- In particular, HYBRID1 manages to achieve a smaller specific humidity RMSE error than the ECMWF model, especially during daytime on the 2^{nd} or 3^{rd} day of forecast (bottom). The bias of WRF is also much closer to zero than the ECMWF model which develops a negative specific humidity bias over forecast time.

8 Conclusion, Outlook and Problems

The aim of this work was to improve the WRF model forecast during the presence of Mediterranean cyclones because those forecasts often delivered unsatisfying results in the past. For this purpose, different configurations were run, where the topography, the horizontal model resolution and the initialization on the vertical levels of the global model was changed. The results are compared with the global model as well as observations, such as radio soundings or weather radar.
Overall, the 4 km topography (HYBRID4) features significant improvements whereas the nested domain (HYBRID1) is only recommendable when major computer resources are available, since it approximately triples the computation time. The initialization on hybrid levels instead of pressure levels brings almost no measurable improvement. In summary, the forecast is improved by high resolution topographies. However, ECMWF still performs as good as HYBRID1, in some error measures even better. This is actually a rather unsatisfactory result - knowing that a global model performs at least as good as a local area model. It is important to say that all these statements are only valid for cases with Mediterranean cyclones - and not in general.

One problem in the verification comes from the used radar data. The SAL seems to be more appropriate for accumulated precipitation values. There are problems with SAL when there is just little or even no precipitation at all which is sometimes the case when using hourly radar data. SAL works best with well shaped precipitation fields.

A few aspects stood out in this work where further investigation is needed:

Negative pressure bias: The global model ECMWF but in particular WRF have a negative bias (too low pressure) in cases with Mediterranean cyclones. This is striking in the center right panel in Fig. 7.8 or rather indirect in Fig. 7.4, where the geopotential height has a negative bias in lower levels. Although this aspect gets better with higher resolution, there is still a bias left. This may be connected to the positive wind speed bias in Fig. 7.6, as a negative pressure bias could cause higher pressure gradient and thus higher wind speeds. This bias gives hints that there are problems with friction or the roughness length so that the model allows for pressure systems to develop too strong.

Warm temperature bias: As shown in Fig. 7.1, there is a warm temperature bias with the higher resolution WRF runs, especially in the Alpine region. This may be due to stronger descending air on mountain lees or in other words, a too strong Foehn-like wind. This is confirmed if one looks at Fig. 6.4 (bottom right). There are valleys or small spots in Austria or northern Italy where no precipitation is modeled. Another planetary boundary layer (PBL) scheme of WRF may help to reduce this bias.

Positive precipitation bias: The amplitude component in Fig. 7.7 (center) indicates a positive bias in the time range where most of the precipitation happened. This is between 20 and 60 forecast hours. This means that all WRF configurations forecast too much precipitation in this area, which is mainly southern Germany, Austria and the Czech Republic.

Northward shifted pressure and precipitation fields: At least in the two case studies of Mediterranean cyclones, the isolines of pressure and the precipitation fields are shifted to the north (see Fig. 6.3, 6.4, 6.6 and 6.17). Although this does not have to be true for all cases, it may be an important input for further investigation.

Bibliography

Robert E. Alduchov, Oleg A .and Eskridge. Improved magnus form approximation of saturation vapor pressure. *Journal of Applied Meteorology*, 35(4):601–609, 1996.

P. Alpert, B.U. Neeman, and Y. Shay-El. Climatological analysis of mediterranean cyclones using ecmwf data. *Tellus A*, 42(1):65–77, 1990.

Erik Andersson. *User guide to ECMWF forecast products*, November 2015.

J. Siegfried Bauer, Rudolf Gutdeutsch, Michael Hantel, Heinz Reuter, Helmut O. Rucker, Gerold Siedler, Tilman Spohn, R Steinacker, and Walter Zenk. *Erde und Planeten, Band 7 der Reihe Bergmann-Schaefer: Lehrbuch der Experimentalphysik. Walther de Gruyter*, volume 2, chapter 3.2.4.1, page 184. 2001.

Peter Bauer, Anton Beljaars, Maike Ahlgrimm, Peter Bechtold, Jean-Raymond Bidlot, Massimo Bonavita, Alessio Bozzo, Richard Forbes, Elias Hólm, Martin Leutbecher, et al. *Model Cycle 38r2: Components and Performance*. 2013.

Katharina Brugger. Bestimmung von Flächenniederschlägen über Zentral-und Nordeuropa aus Wetterradardaten. Master's thesis, Universität Wien, 2004.

Joan Campins, Agustí Jansà, and Ana Genovés. Three-dimensional structure of western mediterranean cyclones. *International journal of climatology*, 26(3):323–343, 2006.

Joan Campins, A. Genovés, MA Picornell, and A. Jansà. Climatology of mediterranean cyclones using the era-40 dataset. *International Journal of Climatology*, 31(11):1596–1614, 2011.

Stephen Eckermann. Hybrid σ-p coordinate choices for a global model. *Monthly Weather Review*, 137(1):224–245, 2009.

ECMWF, 2013. URL `http://www.ecmwf.int/en/forecasts/documentation-and-support/137-model-levels`. [2015-10-28].

J. Egger and K.P. Hoinka. Fronts and orography. *Meteorology and Atmospheric Physics*, 48(1-4):3–36, 1992.

Michael Hofstätter and Barbara Chimani. Van bebber's cyclone tracks at 700 hpa in the eastern alps for 1961–2002 and their comparison to circulation type classifications. *Meteorologische Zeitschrift*, 21(5):459–473, 2012.

Ian T. Jolliffe and David B. Stephenson. *Forecast verification: a practitioner's guide in atmospheric science*. John Wiley & Sons, 2003.

René Laprise. The euler equations of motion with hydrostatic pressure as an independent variable. *Monthly weather review*, 120(1):197–207, 1992.

Daniel Leuenberger, Marcel Koller, Oliver Fuhrer, and Christoph Schär. A generalization of the sleve vertical coordinate. *Monthly Weather Review*, 138(9):3683–3689, 2010.

P. Maheras, H.A. Flocas, I. Patrikas, and Chr. Anagnostopoulou. A 40 year objective climatology of surface cyclones in the mediterranean region: spatial and temporal distribution. *International Journal of Climatology*, 21(1):109–130, 2001.

D. Mayer, A. Steiner, and R. Steinacker. Innovations and applications of the vera quality control. *Geoscientific Instrumentation, Methods and Data Systems*, 1(2):135–149, 2012.

J.A. McGinley and M. Zupanski. Numerical analysis of the influence of jets, fronts, and mountains on alpine lee cyclogenesis: More cases from the alpex sop. *Meteorology and Atmospheric Physics*, 43(1-4):7–20, 1990.

M. Messmer, J.J. Gómez-Navarro, and C.C. Raible. Climatology of vb cyclones, physical mechanisms and their impact on extreme precipitation over central europe. *Earth System Dynamics Discussion*, 6:907–941, 2015.

Manfred Mudelsee, Michael Börngen, Gerd Tetzlaff, and Uwe Grünewald. Extreme floods in central Europe over the past 500 years: Role of cyclone pathway Zugstrasse Vb. *Journal of Geophysical Research: Atmospheres*, 109(D23), 2004.

Roger A. Pielke Sr. *Mesoscale meteorological modeling*, volume 98. Academic press, 2013.

Johannes Rausch. Improvement of short term precipitation forecasts in the alpine region using wrf with 3dvar radar reflectivity and synop assimilation. Master's thesis, Universität Wien, 2012.

Harold Ritchie, Clive Temperton, Adrian Simmons, Mariano Hortal, Terry Davies, David Dent, and Mats Hamrud. Implementation of the semi-lagrangian method in a high-resolution version of the ecmwf forecast model. *Monthly Weather Review*, 123(2):489–514, 1995.

Christoph Schär, Daniel Leuenberger, Oliver Fuhrer, Daniel Lüthi, and Claude Girard. A new terrain-following vertical coordinate formulation for atmospheric prediction models. *Monthly Weather Review*, 130(10):2459–2480, 2002.

AJ Simmons and R Strüfing. *An energy and angular momentum conserving finite-difference scheme, hybrid coordinates and medium-range weather prediction*. European Centre for Medium Range Weather Forecasts, 1981.

William C. Skamarock, Joseph B. Klemp, Jimy Dudhia, Dale M. Barker, Michael G. Duda, Xiang-Yu Huang, Wei Wang, and Jordan G. Powers. A discription of the advanced research wrf version 3. Technical report, Mesoscale and Microscale Meteorology Division, National Center for Atmospheric Research, Boulder, Colorado, USA, 2008.

Henry R. Stanski, Laurence J. Wilson, and William R. Burrows. *Survey of common verification methods in meteorology*. World Meteorological Organization Geneva, 1989.

Reinhold Steinacker, Matthias Ratheiser, Benedikt Bica, Barbara Chimani, Manfred Dorninger, Wolfgang Gepp, Christoph Lotteraner, Stefan Schneider, and Simon Tschannett. A mesoscale data analysis and downscaling method over complex terrain. *Monthly Weather Review*, 134(10):2758–2771, 2006.

I.F. Trigo, T.D. Davies, and G.R. Bigg. Objective climatology of cyclones in the mediterranean region. *J. Climate*, 12:1685–1696, 1999.

I.F. Trigo, G.R. Bigg, and T.D. Davies. Climatology of cyclogenesis mechanisms in the mediterranean. *J. Climate*, 130:549–569, 2002.

M. Tsidulko and P. Alpert. Synergism of upper-level potential vorticity and mountains in genoa lee cyclogenesis–a numerical study. *Meteorology and Atmospheric Physics*, 78 (3-4):261–285, 2001.

Wilhelm Jakob Van Bebber. Typische witterungserscheinungen - archiv der deutschen seewarte. page 45 pp, 1882.

W.J. van Bebber. *Die Zugstrassen der barometrischen Minima nach den Bahnenkarten der deutschen Seewarte für den Zeitraum 1875-1890*. 1891.

W. Wang et al. *WRF-ARW Version 3 Modeling System User's Guide*. Mesoscale and Microscale Meteorology Division, National Center for Atmospheric Research, Boulder, Colorado, USA, July 2015.

Heini Wernli, Marcus Paulat, Martin Hagen, and Christoph Frei. Sal-a novel quality measure for the verification of quantitative precipitation forecasts. *Monthly Weather Review*, 136(11):4470–4487, 2008.

Fuqing Zhang, Chris Allen, Kramer; David, Robert Smith, and Aaron Stults. Vertical resolution and coordinates, 2002. URL `http://www.met.tamu.edu/class/metr452/models/2001/vertres.html`. [2015-10-28].

List of Figures

Acknowledgments

First of all, I want to thank my supervisor Prof. Leopold Haimberger for his help and advice during my work on my master's thesis, especially for his quick answers via e-mail. Furthermore, this work would not have been possible without the help of many employees at UBIMET, such as Johannes Rausch, Aron Drüszler and Dieter Mayer. Along with many others, they helped me out countless times when my programming skills were not sufficient. Additionally, they gave me a lot of valuable input with regards to the content.

My thanks also go out to my sister, who assisted me in the search for typing errors, grammatical mistakes or the general improvement of the linguistic quality. I would also like to thank my parents without whose (financial) support the last six years of university would not have been possible. Finally, I want to thank all my colleagues and friends for making these years a very pleasant time.

Appendix

Verification with Radio Soundings

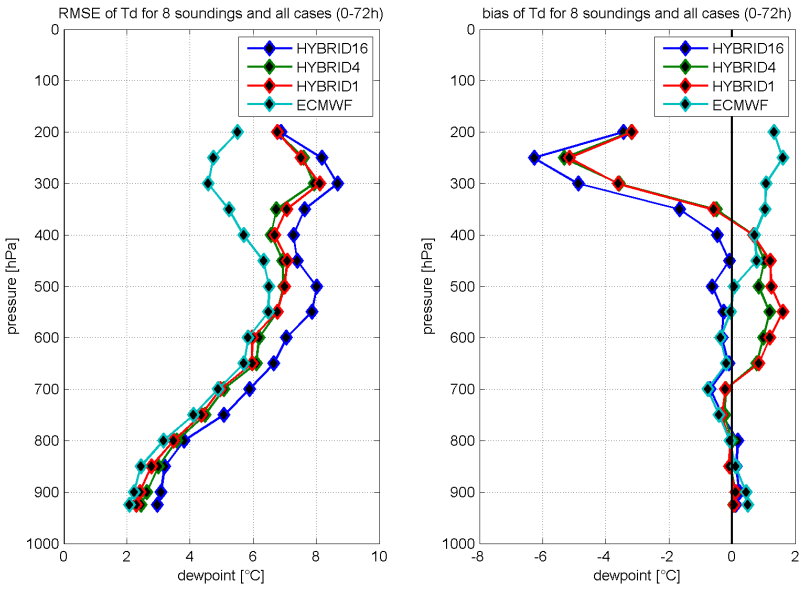

Verification of dewpoint with data from radio soundings for HYBRID16, HYBRID4, HYBRID1 and ECMWF. Only radio soundings from inside the nested domain are used. The values are averaged over the 8 soundings that lie within the nested domain (Bold locations in Table 5.2) and all 14 dates (Table 5.1) and all 72 forecast hours

1th Case: 2013-09-15 until 2013-09-18

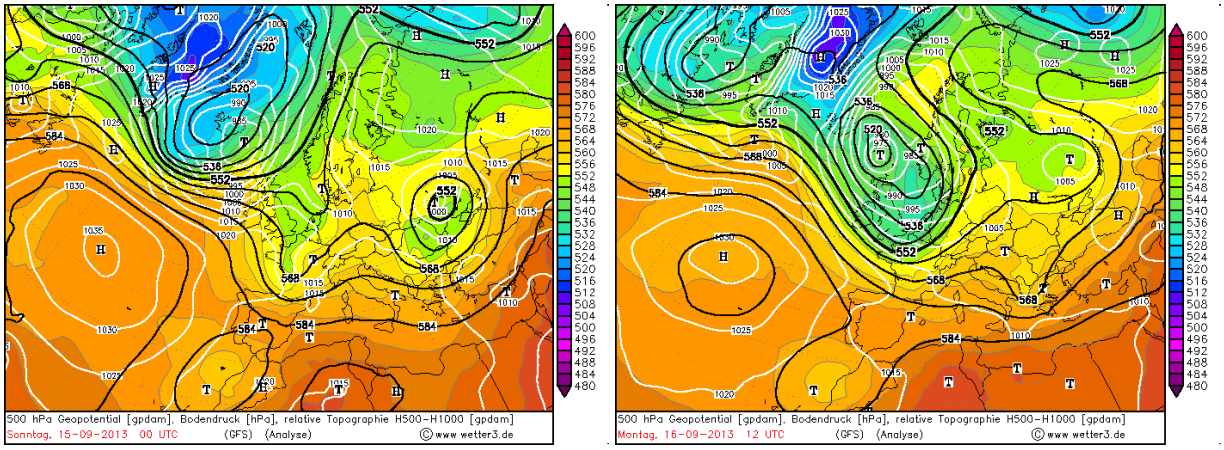

Synoptic weather conditions at inizialization (left) and 36 h after initialization (right). The white lines indicate the MSLP in hPa and the black lines indicate the relative topography which is the difference in gpdam of the 1000 hPa and 500 hPa level. The filled color fields show the 500 hPa geopotential height in gpdam. Source: `http://www1.wetter3.de/Archiv/`

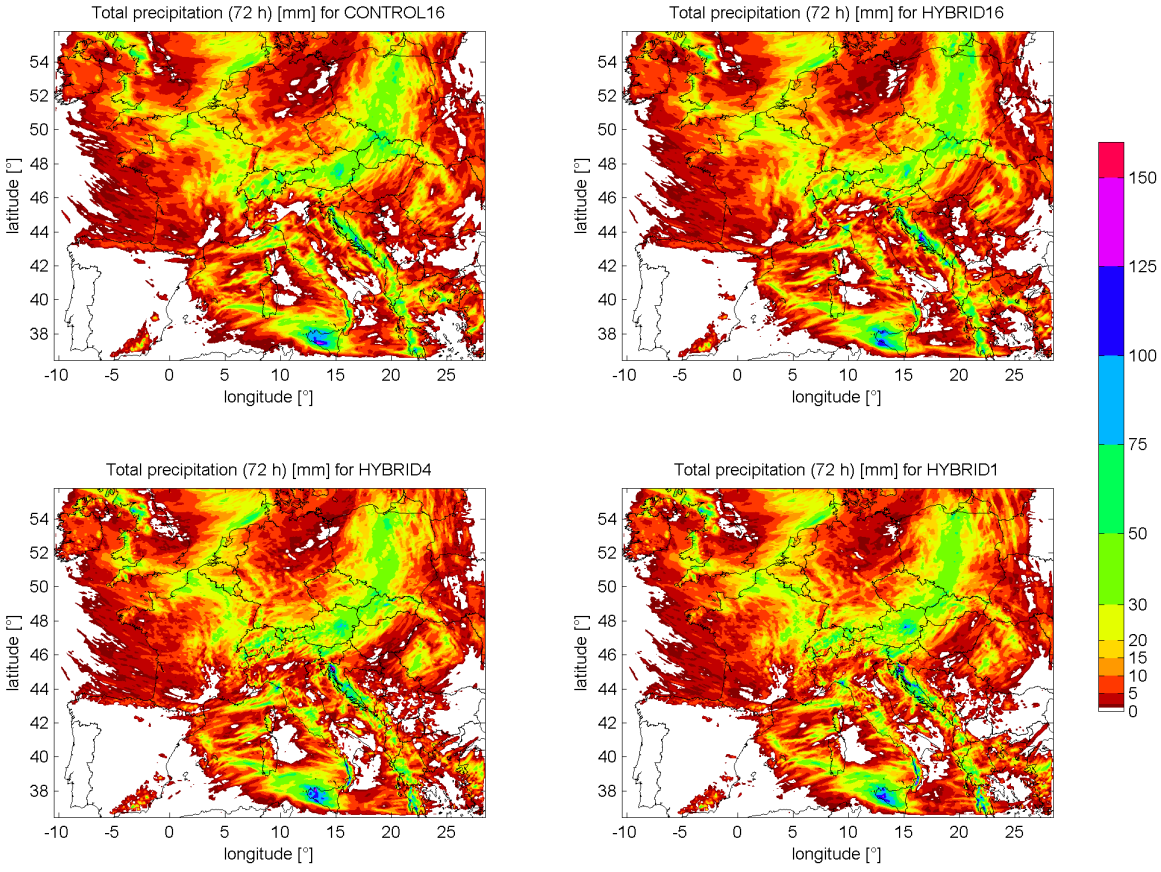

Total 72 h precipitation forecasts for all four WRF runs. Top left: CONTROL16. Top right: HYBRID16. Bottom left: HYBRID4. Bottom right: HYBRID1.

2th Case: 2014-01-19 until 2014-01-22

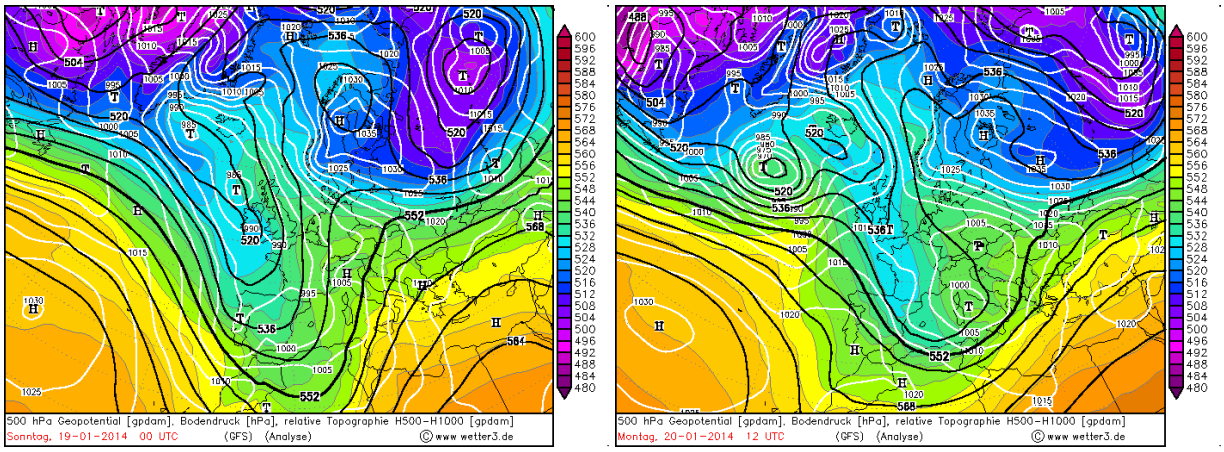

Synoptic weather conditions at inizialization (left) and 36 h after initialization (right). The white lines indicate the MSLP in hPa and the black lines indicate the relative topography which is the difference in gpdam of the 1000 hPa and 500 hPa level. The filled color fields show the 500 hPa geopotential height in gpdam. Source: `http://www1.wetter3.de/Archiv/`

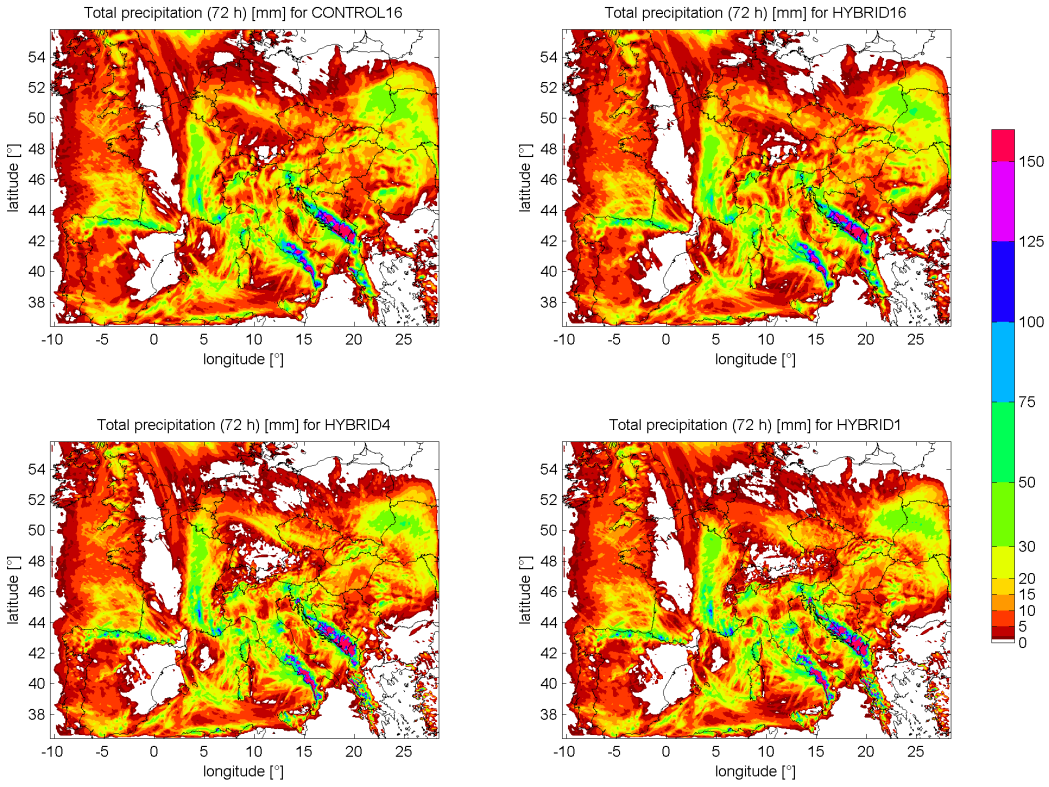

Total 72 h precipitation forecasts for all four WRF runs. Top left: CONTROL16. Top right: HYBRID16. Bottom left: HYBRID4. Bottom right: HYBRID1.

3th Case: 2014-03-22 until 2014-03-25

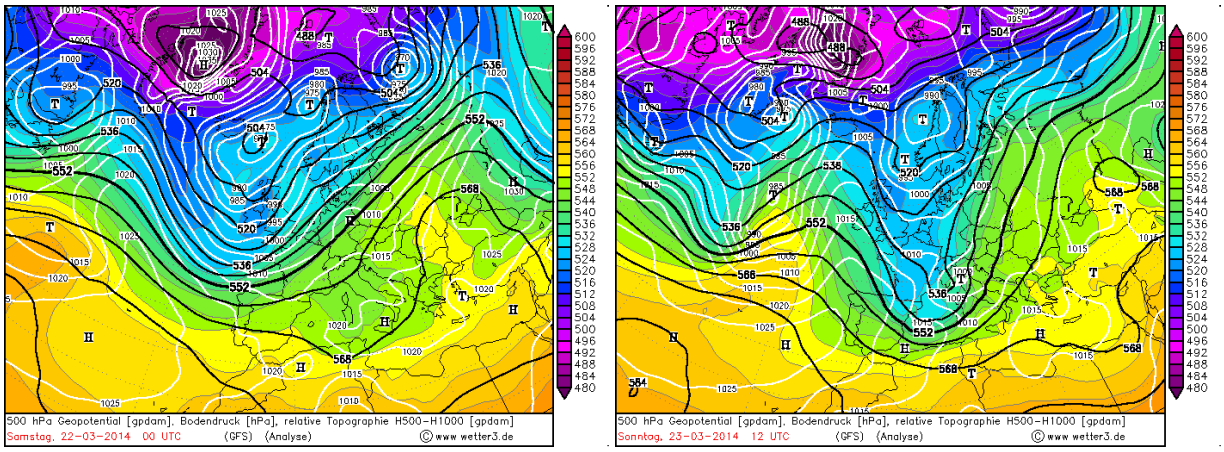

Synoptic weather conditions at inizialization (left) and 36 h after initialization (right). The white lines indicate the MSLP in hPa and the black lines indicate the relative topography which is the difference in gpdam of the 1000 hPa and 500 hPa level. The filled color fields show the 500 hPa geopotential height in gpdam. Source: `http://www1.wetter3.de/Archiv/`

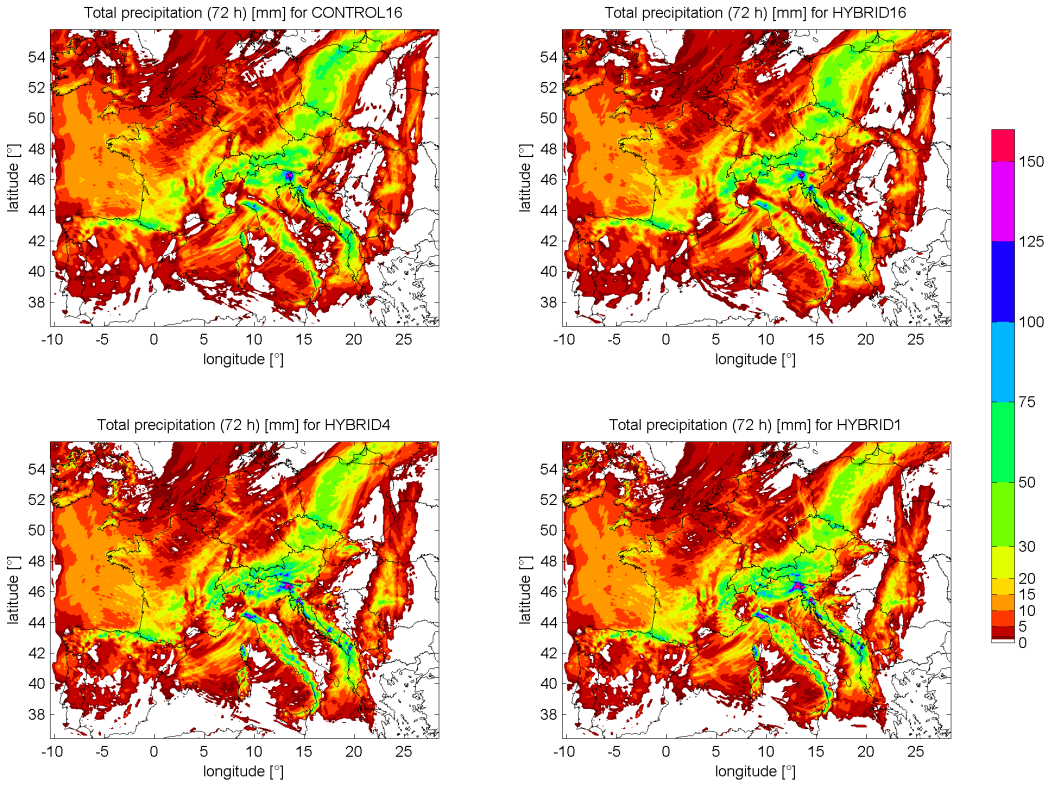

Total 72 h precipitation forecasts for all four WRF runs. Top left: CONTROL16. Top right: HYBRID16. Bottom left: HYBRID4. Bottom right: HYBRID1.

4th Case: 2014-05-14 until 2014-05-17

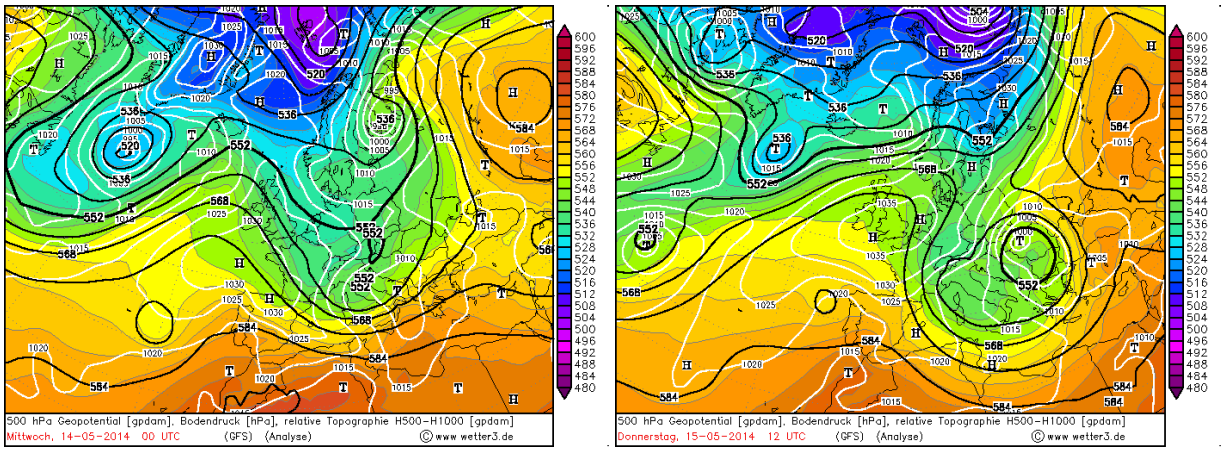

Synoptic weather conditions at inizialization (left) and 36 h after initialization (right). The white lines indicate the MSLP in hPa and the black lines indicate the relative topography which is the difference in gpdam of the 1000 hPa and 500 hPa level. The filled color fields show the 500 hPa geopotential height in gpdam. Source: `http://www1.wetter3.de/Archiv/`

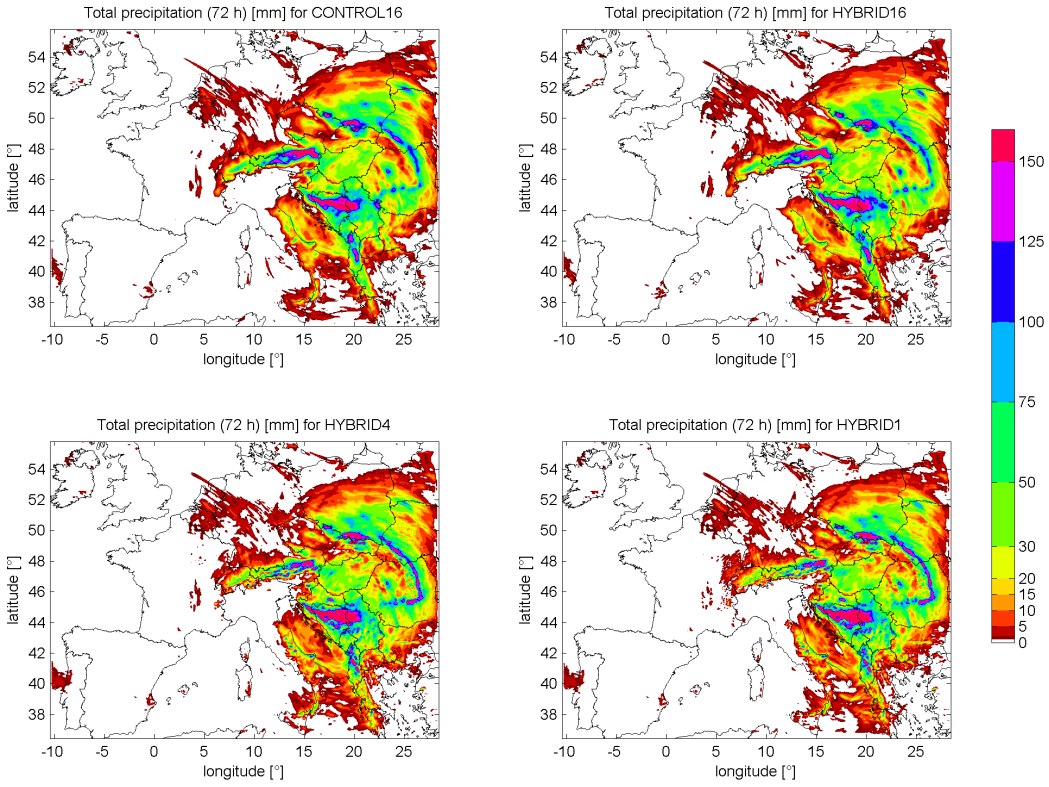

Total 72 h precipitation forecasts for all four WRF runs. Top left: CONTROL16. Top right: HYBRID16. Bottom left: HYBRID4. Bottom right: HYBRID1.

5th Case: 2014-07-20 until 2014-07-23

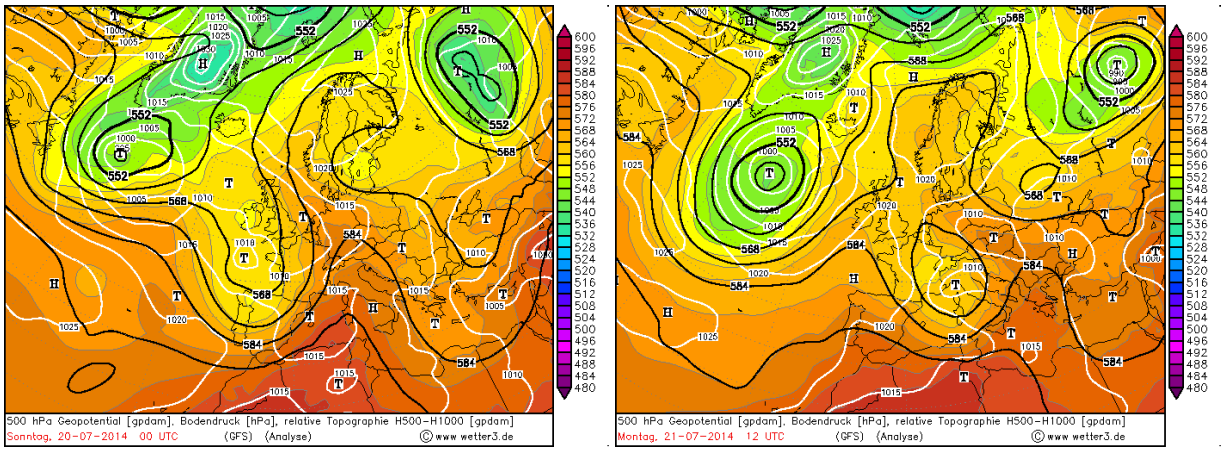

Synoptic weather conditions at inizialization (left) and 36 h after initialization (right). The white lines indicate the MSLP in hPa and the black lines indicate the relative topography which is the difference in gpdam of the 1000 hPa and 500 hPa level. The filled color fields show the 500 hPa geopotential height in gpdam. Source: `http://www1.wetter3.de/Archiv/`

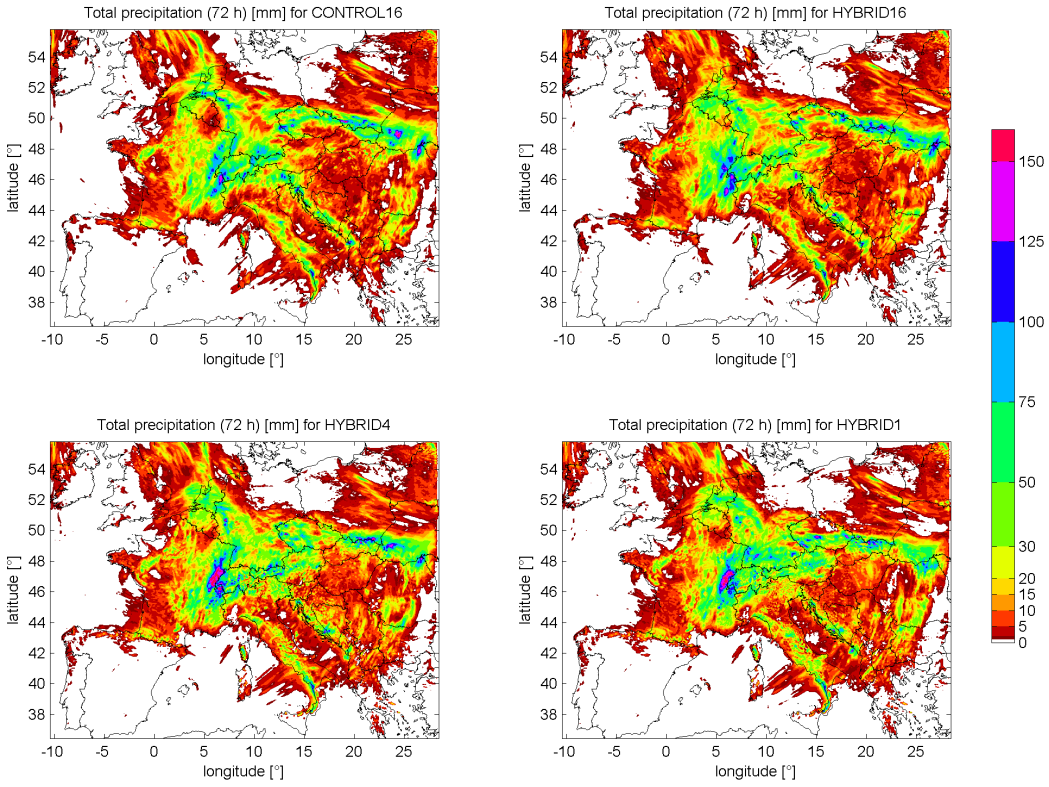

Total 72 h precipitation forecasts for all four WRF runs. Top left: CONTROL16. Top right: HYBRID16. Bottom left: HYBRID4. Bottom right: HYBRID1.

6th Case: 2014-07-28 until 2014-07-31

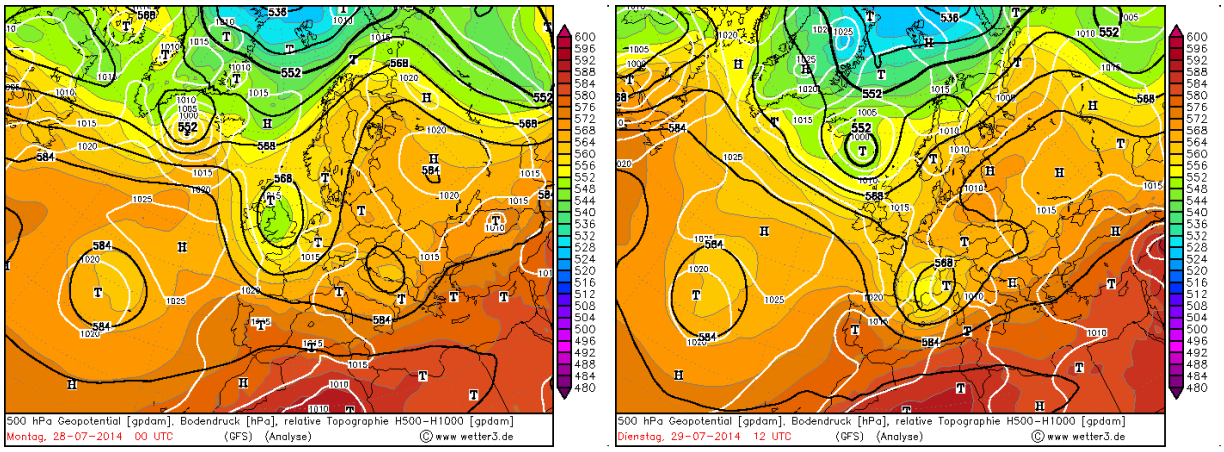

Synoptic weather conditions at inizialization (left) and 36 h after initialization (right). The white lines indicate the MSLP in hPa and the black lines indicate the relative topography which is the difference in gpdam of the 1000 hPa and 500 hPa level. The filled color fields show the 500 hPa geopotential height in gpdam. Source: `http://www1.wetter3.de/Archiv/`

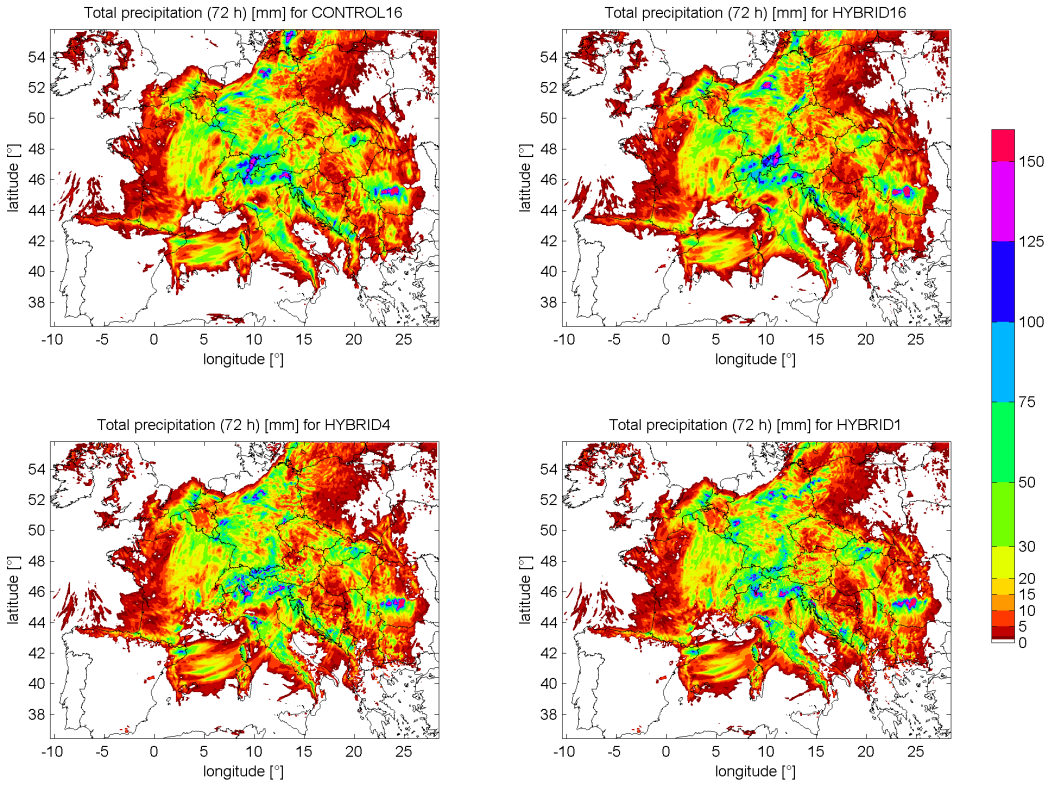

Total 72 h precipitation forecasts for all four WRF runs. Top left: CONTROL16. Top right: HYBRID16. Bottom left: HYBRID4. Bottom right: HYBRID1.

7th Case: 2014-08-31 until 2014-09-03

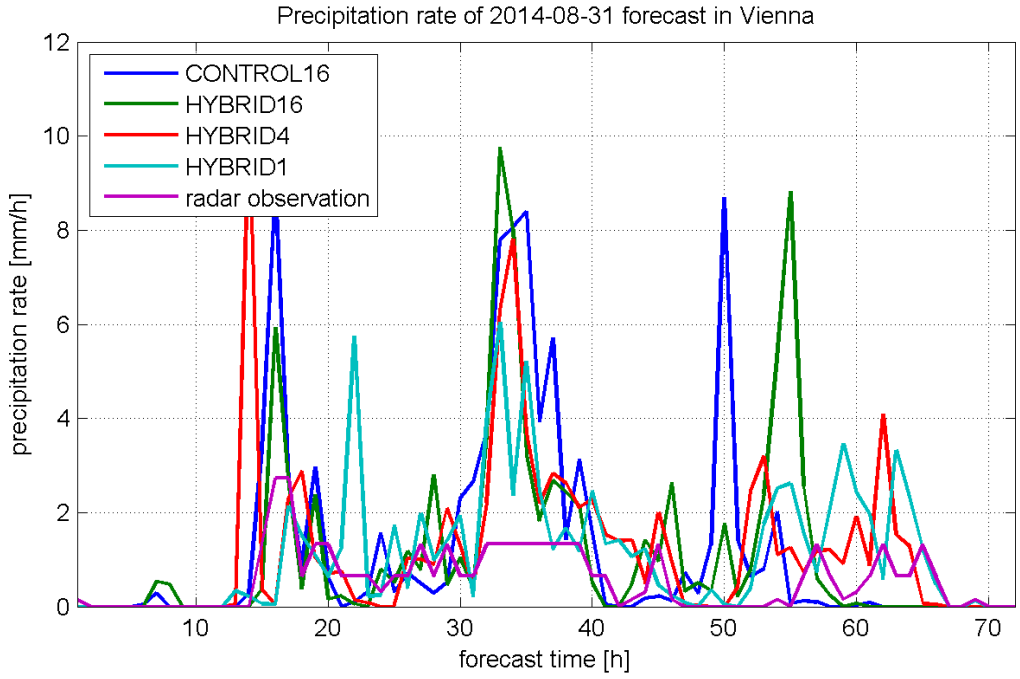

Precipitation rate in Vienna from 2014-08-31 0 UTC to 2014-09-03 0 UTC at every full hour. The radar reflectivity is the maximum radar reflectivity of CERAD for the entire atmosphere. The modeled reflectivity as well as the observed reflectivity is converted into the precipitation rate with Eq. 5.17. The purple line represents the observed radar observation.

8th Case: 2014-09-10 until 2014-09-13

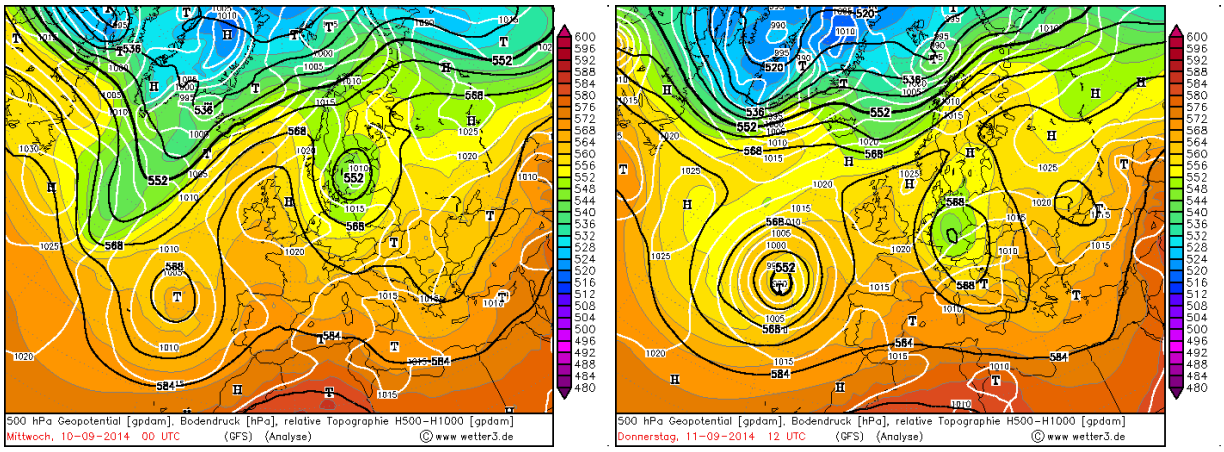

Synoptic weather conditions at inizialization (left) and 36 h after initialization (right). The white lines indicate the MSLP in hPa and the black lines indicate the relative topography which is the difference in gpdam of the 1000 hPa and 500 hPa level. The filled color fields show the 500 hPa geopotential height in gpdam. Source: `http://www1.wetter3.de/Archiv/`

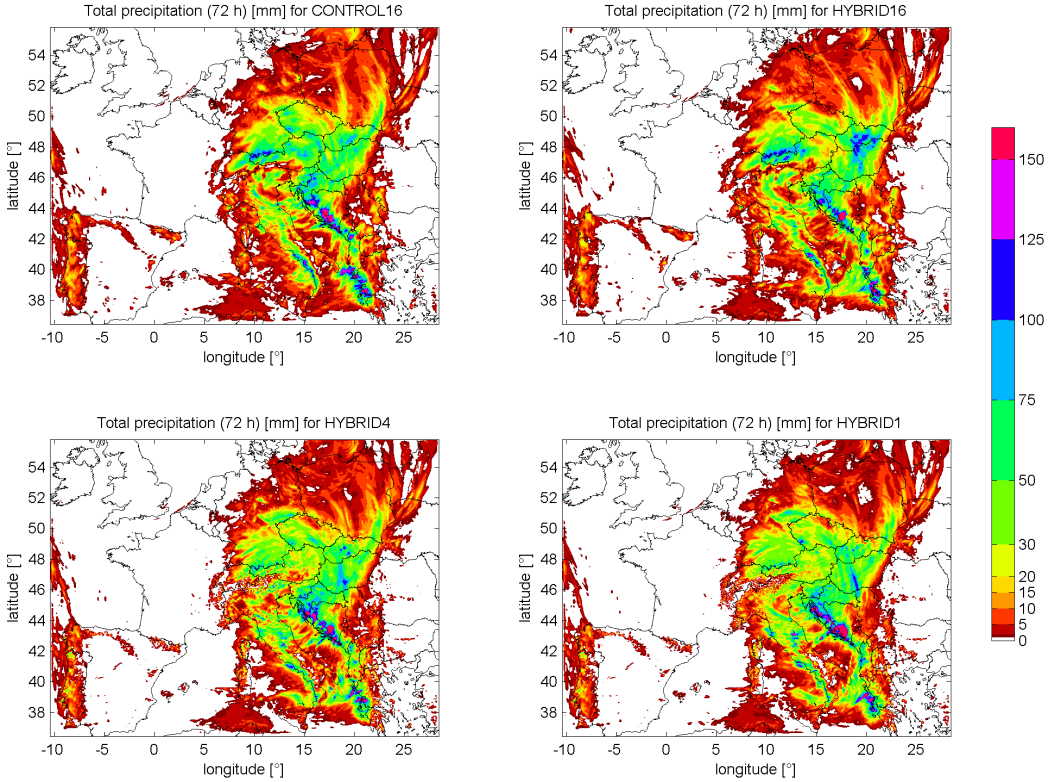

Total 72 h precipitation forecasts for all four WRF runs. Top left: CONTROL16. Top right: HYBRID16. Bottom left: HYBRID4. Bottom right: HYBRID1.

9th Case: 2014-09-12 until 2014-09-15

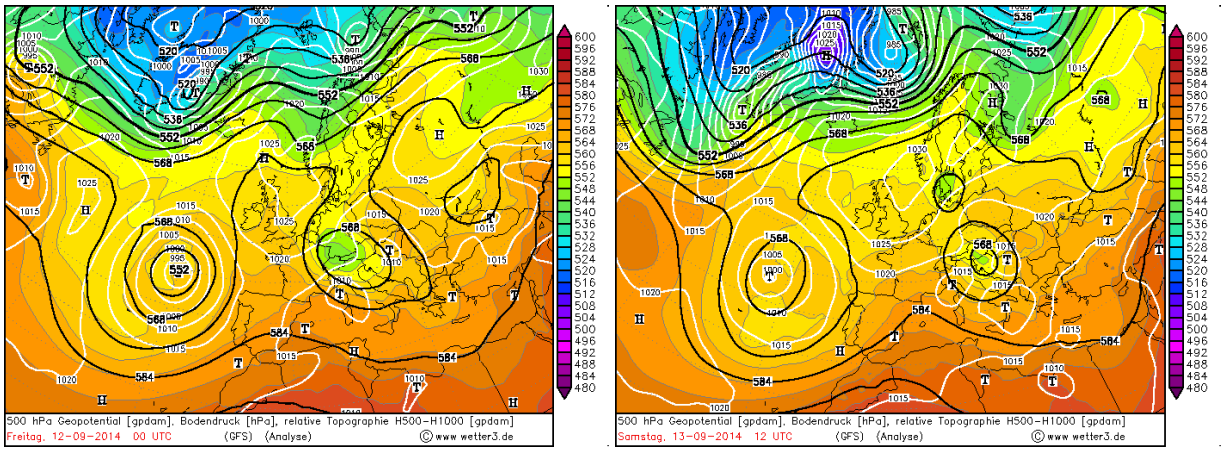

Synoptic weather conditions at inizialization (left) and 36 h after initialization (right). The white lines indicate the MSLP in hPa and the black lines indicate the relative topography which is the difference in gpdam of the 1000 hPa and 500 hPa level. The filled color fields show the 500 hPa geopotential height in gpdam. Source: `http://www1.wetter3.de/Archiv/`

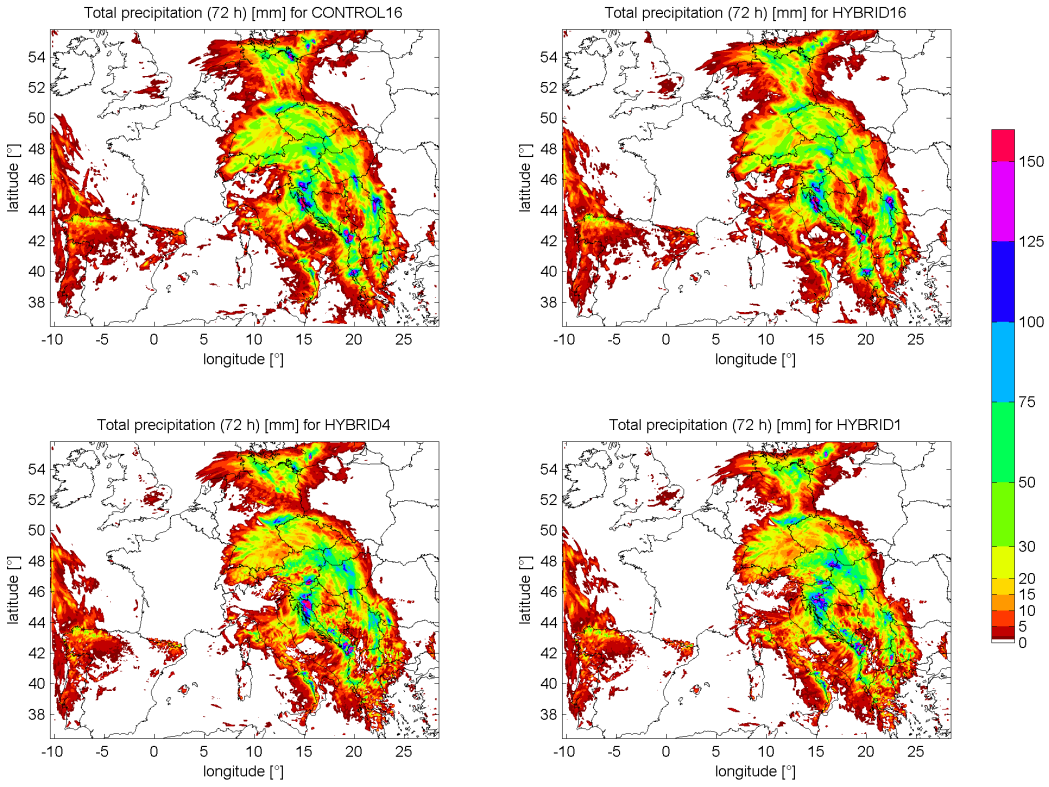

Total 72 h precipitation forecasts for all four WRF runs. Top left: CONTROL16. Top right: HYBRID16. Bottom left: HYBRID4. Bottom right: HYBRID1.

10th Case: 2014-11-04 until 2014-11-07

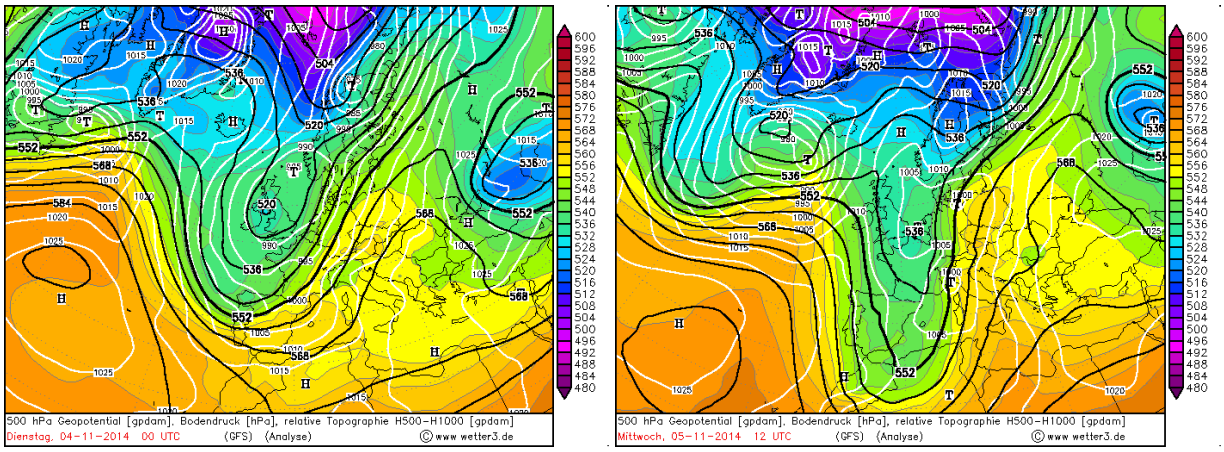

Synoptic weather conditions at inizialization (left) and 36 h after initialization (right). The white lines indicate the MSLP in hPa and the black lines indicate the relative topography which is the difference in gpdam of the 1000 hPa and 500 hPa level. The filled color fields show the 500 hPa geopotential height in gpdam. Source: `http://www1.wetter3.de/Archiv/`

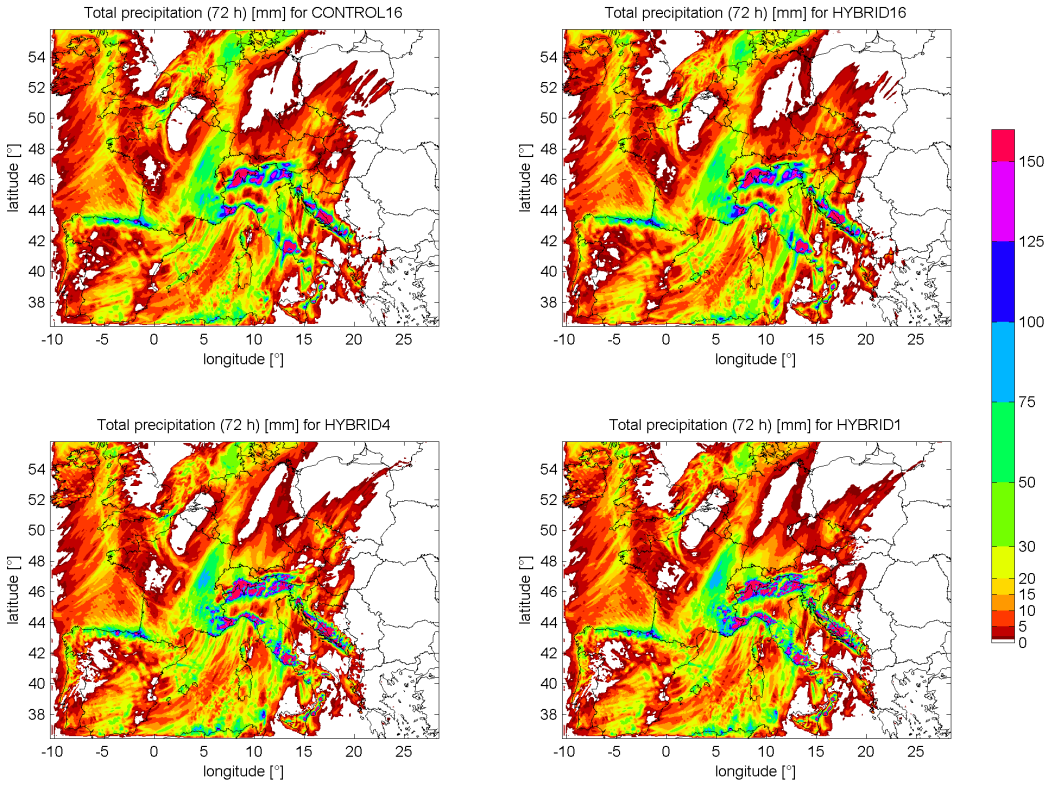

Total 72 h precipitation forecasts for all four WRF runs. Top left: CONTROL16. Top right: HYBRID16. Bottom left: HYBRID4. Bottom right: HYBRID1.

11th Case: 2015-01-23 until 2015-01-26

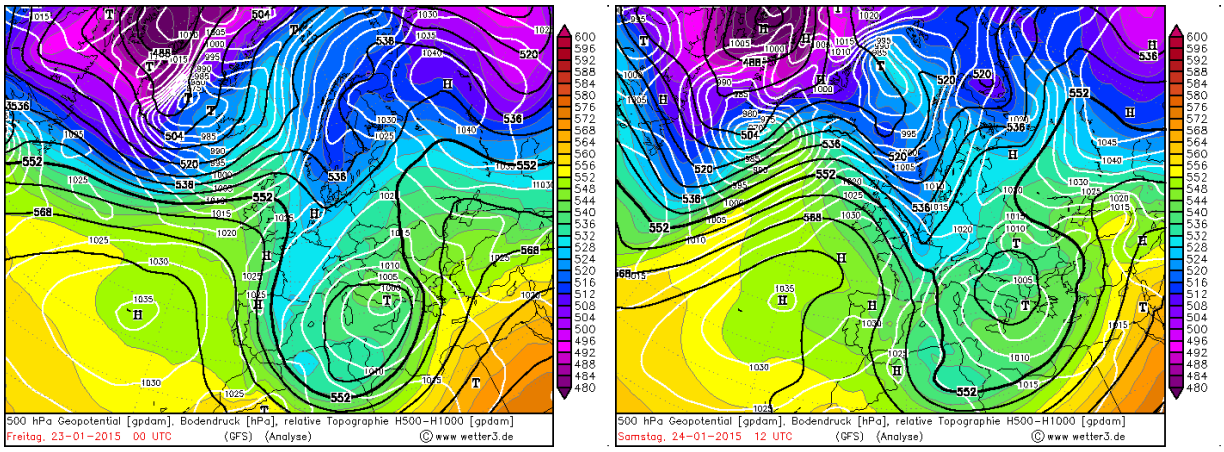

Synoptic weather conditions at inizialization (left) and 36 h after initialization (right). The white lines indicate the MSLP in hPa and the black lines indicate the relative topography which is the difference in gpdam of the 1000 hPa and 500 hPa level. The filled color fields show the 500 hPa geopotential height in gpdam. Source: `http://www1.wetter3.de/Archiv/`

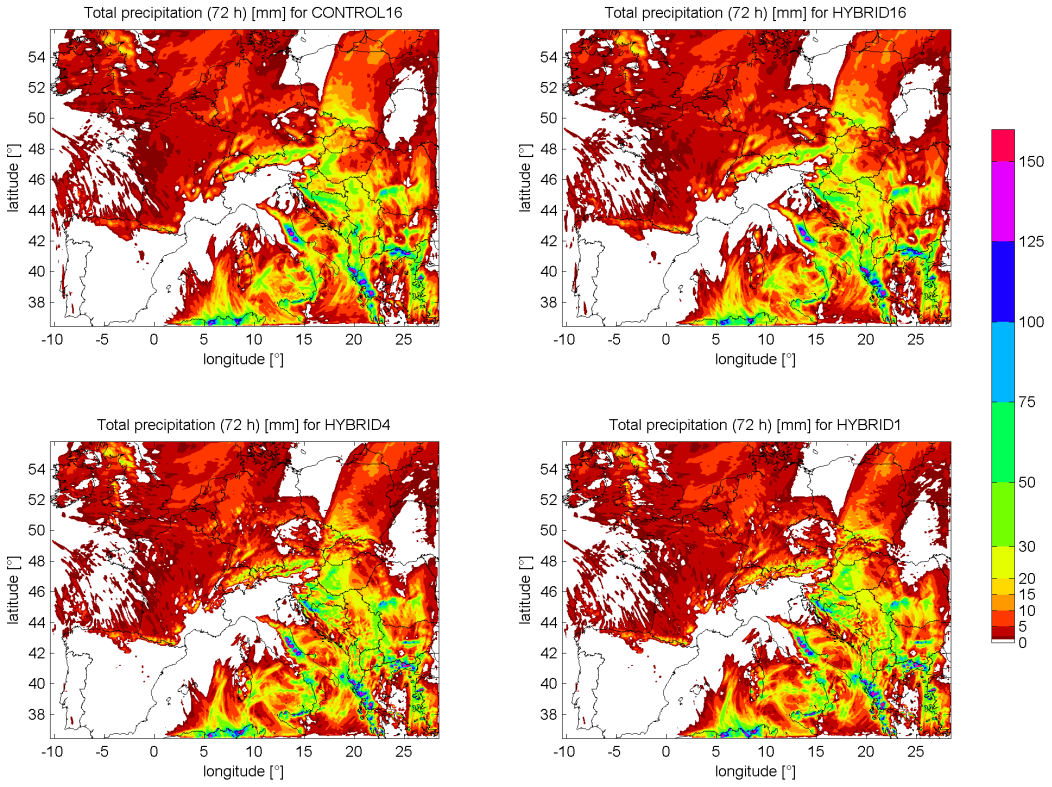

Total 72 h precipitation forecasts for all four WRF runs. Top left: CONTROL16. Top right: HYBRID16. Bottom left: HYBRID4. Bottom right: HYBRID1.

12th Case: 2015-01-29 until 2015-02-01

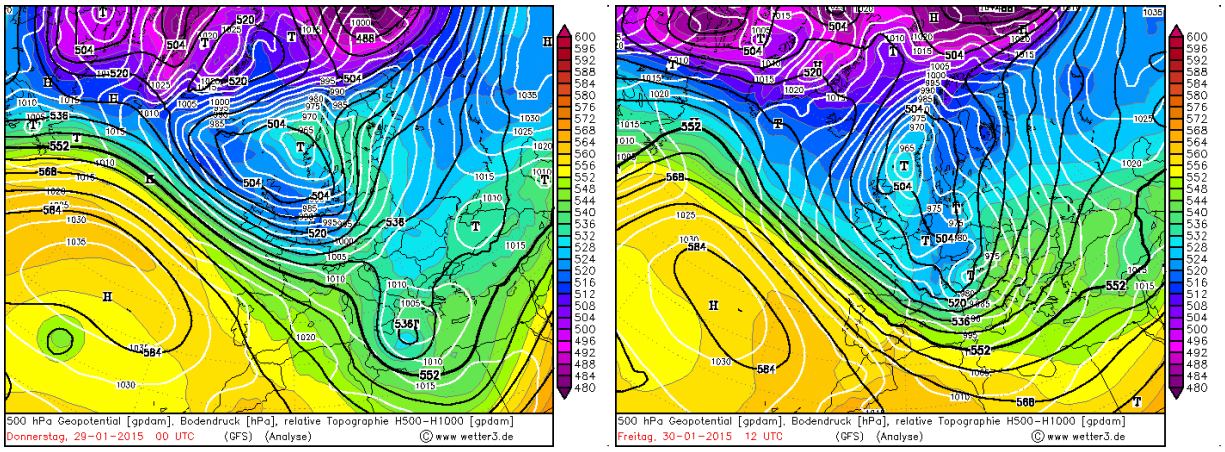

Synoptic weather conditions at inizialization (left) and 36 h after initialization (right). The white lines indicate the MSLP in hPa and the black lines indicate the relative topography which is the difference in gpdam of the 1000 hPa and 500 hPa level. The filled color fields show the 500 hPa geopotential height in gpdam. Source: `http://www1.wetter3.de/Archiv/`

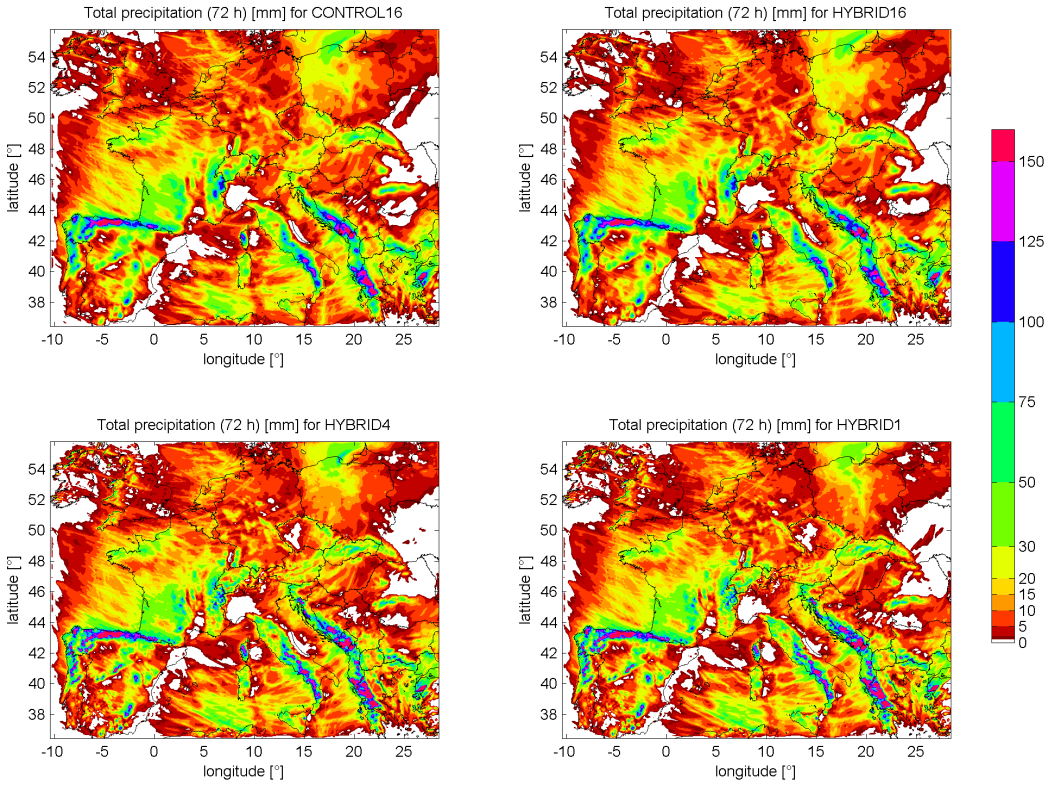

Total 72 h precipitation forecasts for all four WRF runs. Top left: CONTROL16. Top right: HYBRID16. Bottom left: HYBRID4. Bottom right: HYBRID1.

14th Case: 2015-02-23 until 2015-02-26

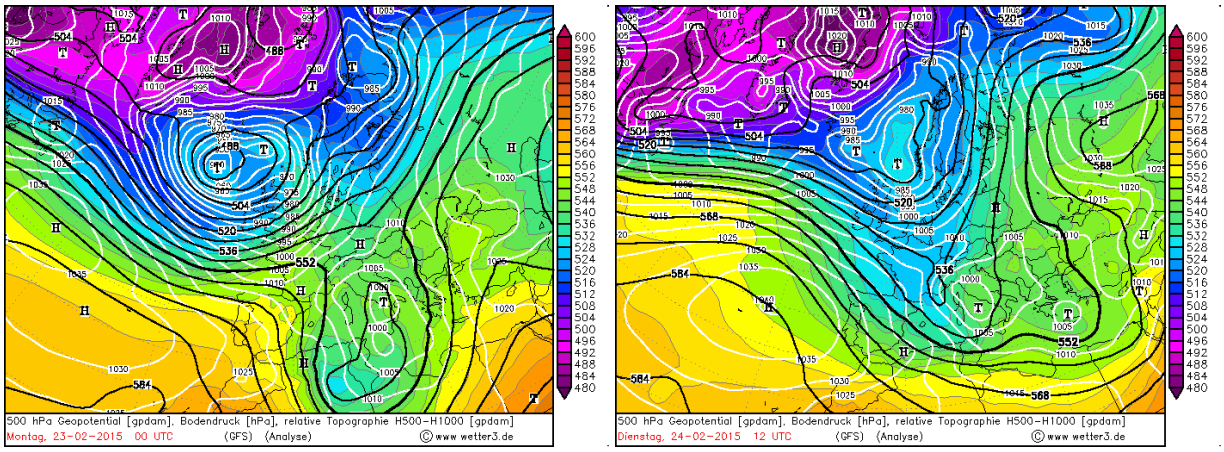

Synoptic weather conditions at inizialization (left) and 36 h after initialization (right). The white lines indicate the MSLP in hPa and the black lines indicate the relative topography which is the difference in gpdam of the 1000 hPa and 500 hPa level. The filled color fields show the 500 hPa geopotential height in gpdam. Source: `http://www1.wetter3.de/Archiv/`

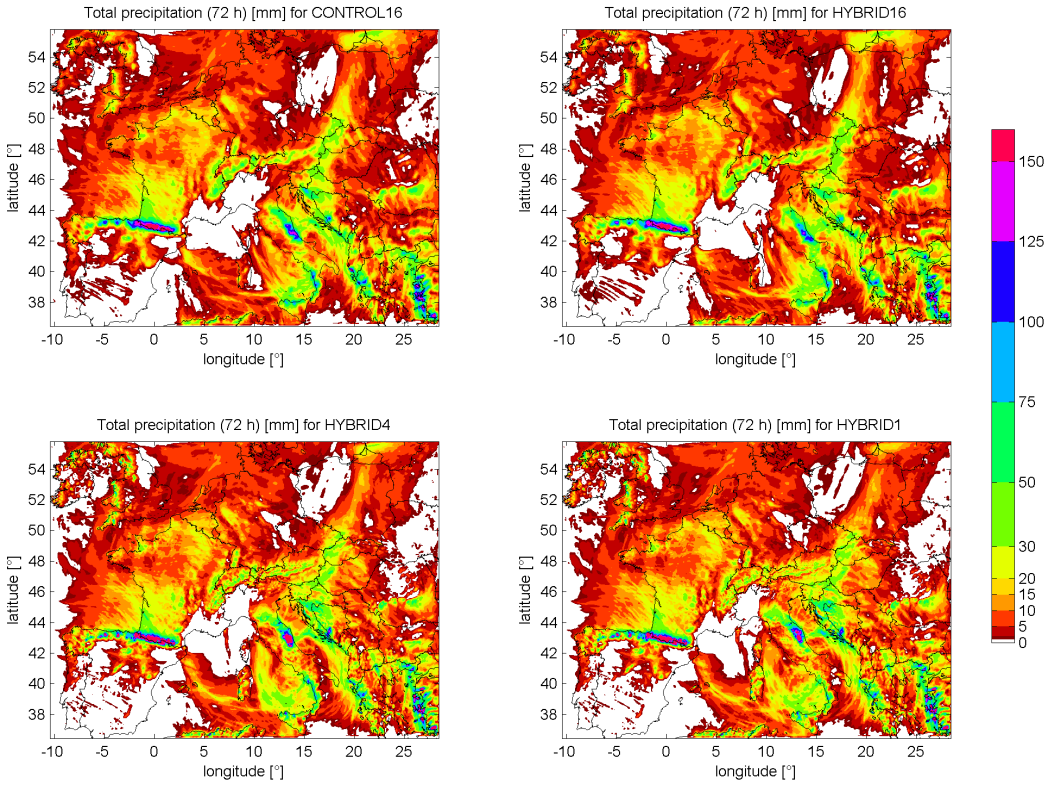

Total 72 h precipitation forecasts for all four WRF runs. Top left: CONTROL16. Top right: HYBRID16. Bottom left: HYBRID4. Bottom right: HYBRID1.